NTNU
Norwegian University of
Science and Technology

Behaviour of the S1 and S2 Components of the Semidiurnal Tide in the MLT

Kåre Backer-Owe

Master of Science
Submission date: June 2016
Supervisor: Patrick Joseph Espy, IFY

Norwegian University of Science and Technology
Department of Physics

Abstract

9 years (2000 – 2008) of wind data from a longitudinal chain of up to 10 Super Dual Auroral Radar Network (SuperDARN) radars spanning over $\sim 184^{\circ}$ in longitude and ranging in latitude from 51.4 – 65.7°N is used to fit the daily meridional semidiurnal amplitudes at different longitudes to extract the zonal wavenumber 1 (S1) and wavenumber 2 (S2) without spatial-temporal aliasing. This thesis focuses on the climatology of the different components, connections to sudden stratospheric warmings (SSW) and the possibility of the auroral electrojet being a generation mechanic for the S1 component.

The climatology shows that the S2 dominates from June to November maximising around fall equinox, followed by another enhancement in winter. The S1 shows an enhancement around the fall equinox. The rest of the year, the S1 and S2 amplitudes are comparable in magnitude.

The behaviour of the S1 and S2 components during SSWs are studied using a superposed epoch of 7 SSWs accompanied by an elevated stratopause event, and show that the response of the semidiurnal tide to SSW is mainly S2 driven. This means that most of the tidal enhancement during an SSW would be capable of propagating into the ionosphere and initiating the process by which the SSW signature is carried to the equator, as suggested by Chau et al. (2012).

The auroral electrojet is investigated as a possible generation mechanism of the S1 component through joule heating by correlating yearly S1 anomaly data with the AE index. During solar minimum this yields weak correlations (~ 0.2 – 0.3) significant above the 95% confidence level and shows a clear repeating 27 day cycle. This repeating pattern is thought to be linked to persisting high-speed solar wind streams associated with coronal holes, adding credibility that there is a weak solar link to the generation of the S1 component, and that it is particle rather than radiatively driven.

Sammendrag

9 år (2000 – 2008) med vind-data fra opptil 10 Super Dual Auroral Radar Network (SuperDARN)-radarer spredt over $\sim 184°$ i lengdegrad og fra 51.4 – 65.7°N i breddegrad, blitt brukt til å estimere komponentene med bølgetall 1 (S1) og 2 (S2) av den meridionale 12-timers tidebølgen i mesosfæren og nedre termosfæren uten rom-tid-aliasing. Denne hovedoppgaven fokuserer på å bestemme klimatologien til disse to bølgekomponentene, undersøke forbindelser til brå stratosfæriske oppvarminger (SSW) og muligheten for at nordlysovalen er tilknyttet dannelsen av S1-komponenten.

Klimatologien viser at S2-komponenten dominerer fra juni til november og når maksimum rundt høstjevndøgn, fulgt av en ny forsterkning i vintermånedene. S1 blir også kraftigere rundt vårjevndøgn. Om våren er som regel S1 og S2 tilnærmet like kraftige.

Ved å slå sammen resultater rundt 7 SSW-hendelser, som også er etterfulgt av en hevet stratopause, er oppførselen til S1 og S2 studert. Resultatene viser at disse hendelsene hovedsakelig er drevet av S2-komponenten. Dette betyr at mesteparten av forsterkningen av 12-timersbølgen i løpet av en SSW vil være i stand til å propagere inn i ionosfæren og starte prosessen som SSW-signaturen bringer til ekvator, som foreslått av Chau et al. (2012).

Nordlysovalen blir undersøkt som en mulig dannelsesmekaniske for S1-bølger gjennom oppvarming ved å sammenligne S1-anomalidata med *AE*-indeksen. Under solminimum gir dette en svak korrelasjon (~ 0.2 – 0.3) signifikant over 95% konfidensnivået, og viser en klar repeterende 27-dagers syklus. Dette mønsteret tenkes å være knyttet til vedvarende høy-hastighetssolvind assosiert med koronahull. Dette gir økt tiltro til at solvinden er en dannelsesmekanikk av S1 bølger, og at de er drevet av partikler heller enn stråling.

Preface

This thesis marks the end of my teacher education programme in the natural science at Norwegian University of Science and Technology (NTNU), Trondheim. The degree includes a minimum of 300 credits, where 30 of these credits are from this thesis.

I would like to thank my supervisor Patrick Joseph Espy for his superb guidance and for being the Lucky Luke of email answering. Your in depth explanations coupled with your motivation and enthusiasm for your work has really created an enjoyable environment for learning – in which I have learned a lot.

I would also like to thank my fellow student Magnus Langøien Waalekalv for good discussions and our computational collaboration in the first part of this analysis work.

Big thanks to Gunnar, Knut and Sindre for years of fun and games.

Thanks to my family for their continuous support and engagement.

Contents

Acronyms and Abbreviations

AE	Auroral Electrojet
AV	Absolute Vorticity
CME	Coronal Mass Ejections
ES	Elevated Stratopause
GW	Gravity Wave
MLT	Mesosphere and Lower Thermosphere
NH	Northern Hemisphere
PV	Planetary Vorticity
PW	Planetary Wave
RV	Relative Vorticity
S1	Semidiurnal westward propagating wavenumber 1 component
S2	Semidiurnal westward propagating wavenumber 2 component
SH	Southern Hemisphere
SKiYMET	All-Sky Interferometric Meteor Radar
SSW	Sudden Stratospheric Warming
SuperDARN	Super Dual Auroral Radar Network
TOM	Time Of Maximum
UT	Universal Time
WACCM	Whole Atmosphere Community Climate Model
WACCM-SD	Whole Atmosphere Community Climate Model Specific Dynamics

List of Figures

List of Tables

Chapter 1

Introduction

The atmosphere is a complex system of gas surrounding Earth, retained by Earth's gravity. Dynamical and radiative processes in the atmosphere yield different types of fluid waves, which can propagate, and allows the atmosphere to communicate over large distances, both horizontally and vertically. Even though most weather phenomena happen in the first 10 km of the atmosphere, more and more studies are showing important couplings to high altitude phenomena affecting the weather on Earth. Knowledge of such phenomena can be used to improve weather and climate models to improve weather predictions and our understanding of the atmosphere as a whole. This thesis is contributing to this by focusing on one particular type of waves, namely the *atmospheric tides*.

Atmospheric tides are planetary-scale wave motions mainly generated by solar heating of by ozone in the stratosphere (near 20 km altitude). The warm pool in the atmosphere under the sub-solar point is localised in both longitude and latitude resulting in a pressure bulge launching a driven global wave outward from that sub-solar point. Although the waves can propagate both westward and eastward, the westward propagating waves are much greater since they propagate with the apparent motion of the Sun. The atmospheric tidal waves are defined by Earth's rotation rate and have periods which are sub-harmonics of a solar day (i.e. 24 h, 12 h, 8 h etc.). As the waves propagate vertically, the pressure of the surrounding atmosphere decreases exponentially, leading the amplitude of the waves to grow exponentially due to conservation of energy, and can reach wind speeds of up to 100 m/s. Around the mesosphere and lower thermosphere (MLT, 60-100 km), the waves break and deposit their energy and momentum and become the dominant source of variability in the horizontal wind in this region (Oberheide et al., 2015).

The atmospheric tides has been studied for a long time, and in the 20th century, the tides were decomposed into temporal components. The 24 h tide was expected to be most significant since the heating from the Sun has a 24 hour period. However, they found that tidal oscillations of both 24 h and 12 h was generating large amplitudes, and

after that the 12 h tide has raised much interest (Taylor, 1929). To measure the amplitudes of the 12 h tide, one only needs to measure it at the wanted location and time, and by now its behaviour across the globe is well-known (e.g. Schminder et al. (1989); Manson et al. (1989); Lysenko et al. (1994); Jacobi et al. (1999)). Both the amplitude and phases at a single latitude and longitude has been shown to vary a lot with time. This is due to a super-positioning of different wavenumber components. Murphy et al. (2003), Baumgaertner et al. (2006) and Hibbins et al. (2010) have recently studies the 12 h zonal wavenumber 1 and 2 (waves with one and two wavelengths around the world respectively) above the Antarctic region, obtained by two or more measuring stations at different longitudes.

The goal of this thesis is to estimate the wind amplitudes and phases of the zonal wavenumber 1 and 2 components of the 12 h tide in the northern hemisphere MLT, and investigate how they are affected by different atmospheric phenomena. To manage this, northern hemisphere wind data at ~ 95 km of the 12 h tide from a longitudinal chain of stations around 60°N are used, and a non-linear least-squares curve fitting routine is developed assuming that only these two wavenumber components are present. For validation a second method, developed by Baumgaertner et al. (2006), using two stations separated by approximately 180° in longitude is used. 9 consecutive years (2000-2008) of data allows the examination of how inter-annual phenomena affect the semidiurnal tide. In this thesis the response to major breakdowns of the polar vortex, known as sudden stratospheric warmings (SSW) is studied, along with the possible generational mechanics of the wavenumber 1 by asymmetrical heating through solar particle flux, by investigating how it correlates to the auroral electrojet index (AE index).

This thesis is divided into 7 main chapters, including this introduction. In chapter 2 the theory of relevance to the topics discussed in this thesis will be presented. Chapter 3 presents the specific method from which the results will be obtained. These results will then be presented and analysed in chapter 4. The subsequent chapter presents a brief validation based on the obtained results. In chapter 6 the obtained results will be discussed using the presented theory and other relevant studies. Finally, chapter 7 will summarise the thesis and highlight the most important findings and ending with suggestions for future work.

Chapter 2

Theory

The goal of this chapter is to create a framework in which the results of this thesis can be discussed. Firstly, an overview of important topics regarding the atmospheric structure is presented, followed by a presentation of different atmospheric dynamics, mainly in the form of different types of atmospheric waves. Lastly these things are put together to explain some atmospheric coupling phenomena that will be studied further in this thesis.

2.1 Atmospheric structure

Despite the atmosphere being a complex non-linear system, useful insight can be gained when looking at the climatology (weather-average over a period of time) of the atmosphere. This is the basis for the definition of the atmospheric layers.

2.1.1 Atmospheric layers

Figure 2.1 shows (a) the zonal mean (i.e. longitudinal mean) temperature and the mean vertical temperature profile of the atmosphere during a December solstice, and (b) shows the annual mean temperature structure of the atmosphere using the Whole Atmosphere Community Climate Model (WACCM) (Stray, 2015). The turning points of the temperature profile gives rise to convenient borders for defining atmospheric layers. In the troposphere, approximately from 0 to 15 km, the temperature falls of linearly with height due to increasing distance from surface heating. The troposphere is where most of the direct weather phenomena happen and is often referred to as the lower atmosphere.

The stratosphere is defined as the layer above the troposphere and up to about 60 km. This layer contains the main bulk of ozone molecules (O_3) in the atmosphere (Boeker and van Grondelle, 2001). The absorption of ultra-violet radiation from the Sun creates a cycle between atomic oxygen (O), molecular oxygen (O_2) and ozone that results in a thermal energy increase, increasing the temperature in the stratosphere

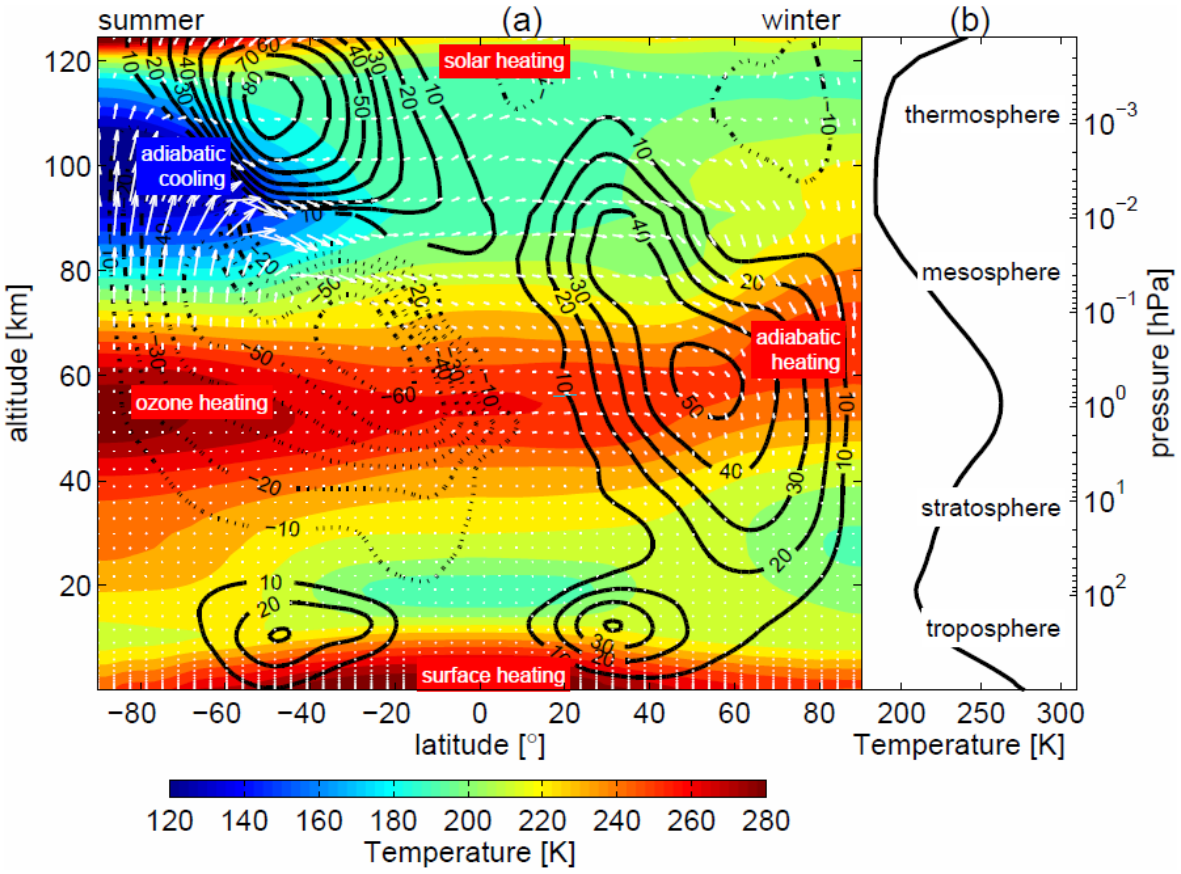

Figure 2.1: Atmospheric structure derived from WACCM. (a) Solstitial atmospheric conditions of zonal-mean temperature (colour plot), zonal-mean zonal wind (black contour lines) and zonal-mean vertical and meridional wind (white arrows). The vertical speed has been enlarged for better visibility. (b) Annual-mean temperature structure. From Stray (2015).

with altitude (Andrews, 2010). The temperature has a local maxima at about 60 km, the stratopause, before it drops off again due to a decrease in radiative heating and an increase in radiative cooling to space by CO_2 in the mesosphere. The stratosphere and mesosphere are often referred to as the middle atmosphere.

As seen from the pressure axis in figure 2.1, the pressure falls off exponentially with altitude. From this, one can estimate that about 90% of the total mass of the atmosphere is located in the troposphere, a little less than 10% in the stratosphere, and only about 0.1% in the mesosphere, thermosphere and above. In the thermosphere, the temperature again increases due to the absorption of very short wavelength solar radiation that results in the dissociation and ionization of molecules. Because the thermospheric density is low, the atmospheric departs from being well mixed and begins to diffusively separate, with lighter species decreasing less rapidly with altitude than heavier ones.

2.1.2 Polar vortex

During winter, there is no solar heating near the winter pole causing lower temperatures and pressures than around the equator. This causes a wind motion towards the winter pole. Since the Earth (and the atmosphere) is rotating eastward, and rotating slower closer to the poles, the air from the equator will be moving eastwards faster than the surrounding air when displaced towards the poles (the Coriolis force). This results in an eastward thermal wind. This strong eastward circumpolar flow around the winter pole is called the *polar vortex* (Andrews, 2010), and maximises around 50 ° latitude at around 60 km altitude, illustrated in figure 2.1 during winter in the northern hemisphere.

There is a similar situation during summer, when stratospheric heating of the ozone near the poles cause a temperature difference between high latitudes and the equator. This yields a temperature gradient between the summer pole towards the equator which, following the same argument as above, results in a westward circumpolar flow in the summer hemisphere. This temperature gradient however is not as strong as in the winter when the pole goes into darkness. This causes the vortex during summer to be much weaker than during winter. In the following, the term polar vortex will only be used to describe the strong eastward winter polar vortex.

The polar vortex in the northern hemisphere (NH) and southern hemisphere (SH) is often referred to as the Arctic and Antarctic polar vortex respectively. The Arctic polar vortex is less stable than the Antarctic polar vortex since zonal distributed land-sea boundaries in the NH are an indirect source for planetary waves (PW) which can propagate up into the stratosphere. In the stratosphere, the PWs, which can only propagate westward in an eastward background wind (section 2.2.3), can interact with the polar vortex, causing a drag and slowing the eastward stratospheric winds during winter. An extreme example of this is a phenomenon called sudden stratospheric warming (SSW), and is detailed in section 2.3.1.

2.2 Atmospheric dynamics

When only looking at the climatology of the atmosphere, the daily dynamics are lost. As an example, in figure 2.1 in the mesosphere and lower thermosphere (MLT) at around 60°N, the mean zonal wind is estimated to be ± 10 m/s, and the meridional wind is small. However, when looking at hourly atmospheric activity the story is quite

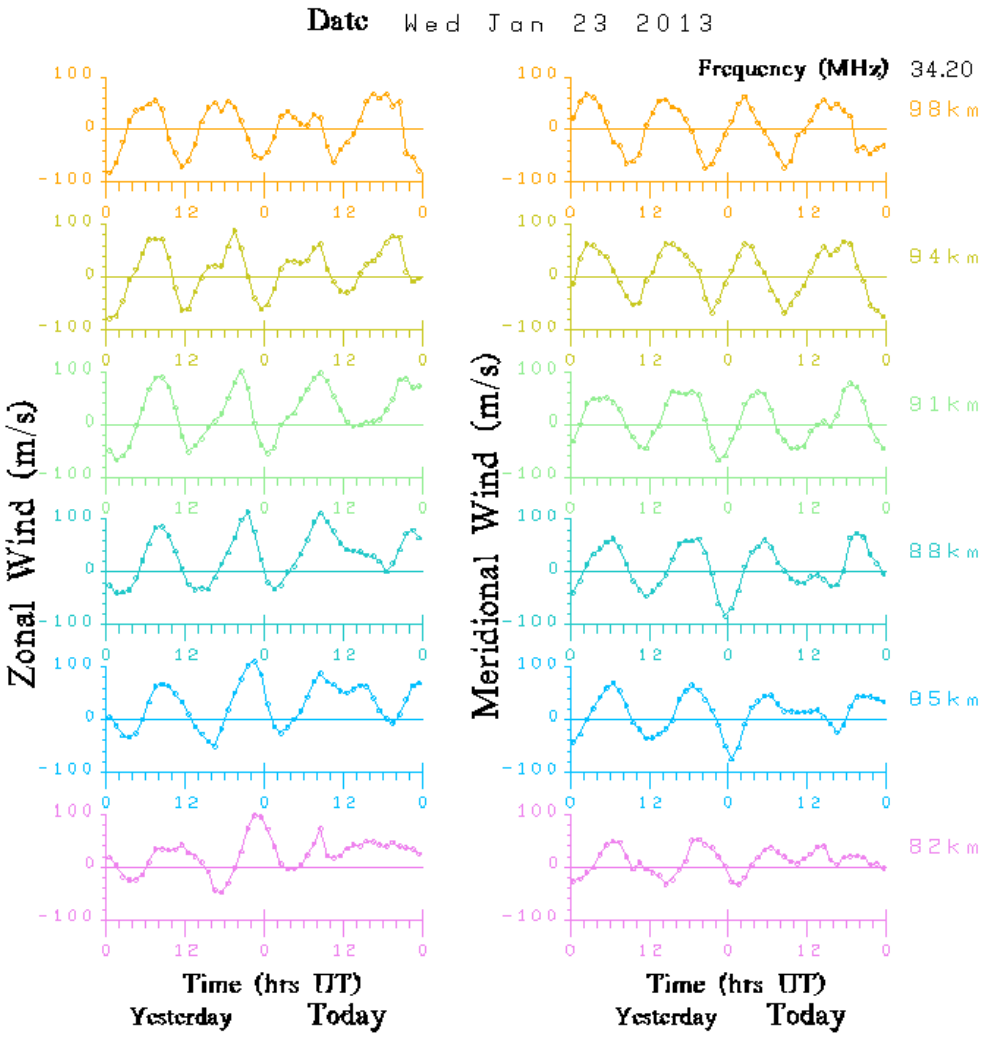

Figure 2.2: Figure from SKiYMET on Dragvoll. Zonal/meridional wind velocity in m/s as a function of time (left/right). Altitude ranges from 82 km to 98 km from top to bottom. Data is from January 22 and January 23 2013.

different. Figure 2.2 shows wind speeds in the MLT (altitudes ranging from 82 km to 98 km) measured by an All-Sky Interferometric Meteor Radar (SKiYMET) placed on Dragvoll at 63°N. This plot shows that in the course of 12 hours the zonal and meridional wind speeds can change between roughly ±90 m/s. In this section we will look into fundamental mechanics that makes the large semidiurnal changes at altitudes around 100 km possible.

2.2.1 Atmospheric tides

As mentioned in section 2.1 ozone in the stratosphere absorbs radiation from the Sun and soon after liberates the energy in the form of heat. Solar absorption by water vapour in the troposphere, as well as photo-dissociation of O_2 and N_2 in the thermosphere (120-180 km) also contribute to the heating of the atmosphere (Forbes, 1995).

The heating in section 2.1 shows the time-averaged heating over the globe. When looking at the diurnal variation of that heating it shows large density and temperature perturbations that moves westward with the apparent motion of the Sun. This creates a large planetary scale wave that propagates outward and upward away from the point of heating. Due to conservation of energy and the exponential decrease in atmospheric density with altitude, the amplitude grows as the disturbance propagates upwards. The maximum heating is located around the sub-solar point, which will move westward with time with the apparent motion of the Sun observed from Earth. This differential heating launches very large planetary-scale oscillations with periods defined by Earth's rotation rate (Forbes, 1995) and they are observed in wind speed, temperature, pressure, density and geopotential height (Oberheide et al., 2015). An example of the wind oscillation induced is shown in figure 2.2, where wind variations as large as $\pm 90\,\mathrm{m/s}$ are observed at subsolar harmonics of the Earth's rotation period.

A derivation of the properties of the atmospheric tides can be described by introducing a heating distribution function $J(t)$ (Forbes, 2009). The heating distribution $J(t)$ can be assumed non-zero during the day and zero at night. This periodicity in time means that it can be expressed using Fourier series as a function of t in hours giving

$$J(t) = \sum_{n=0}^{N} A_n(\theta, z, \lambda) \cos(n\Omega t - \phi_n(\theta, z)). \tag{2.1}$$

Here $\Omega = 2\pi/24\,\mathrm{h}$ and describes the *apparent* motion of the Sun from an observer on Earth, A_n describes the amplitude of each Fourier component in terms of altitude (z), latitude (θ) and longitude (λ) east of Greenwich. ϕ_n describes the phases of each component. $n \geq 0$ describes which fraction of the 24 hours periodicity the wave component has. Thus, $n = 1$ refers to the diurnal wave ($24\,\mathrm{h}$), $n = 2$ the semi-diurnal ($12\,\mathrm{h}$), $n = 3$ the terdiurnal ($8\,\mathrm{h}$) etc.. These wave components are assumed linear, meaning that the atmospheric response for each separate wave component can be calculated separately and added afterwards to describe the total atmospheric response.

Since the sub-solar point on Earth moves approximately along a constant longitude, it can also be assumed periodic in longitude. Including this in the Fourier series results in a heating distribution that is also dependent on the zonal wavenumber S on the form

$$J(t) = \sum_{S=-\infty}^{\infty} \sum_{n=0}^{N} A_{n,S}(\theta, z) \cos(n\Omega t + \lambda S - \phi_{n,S}(\theta, z)). \tag{2.2}$$

Now, the amplitude and phase are only dependent on the altitude and the latitude since the longitudinal effects are described by the zonal wavenumber S. S can be understood as the number of crests around the Earth for a particular wave component. By convention the λS term is introduced in such a way so that a positive and negative S describes westward and eastward propagating waves respectively.

The particular definition of the phase $\phi_{n,S}(\theta, z)$ does not change the physics of the problem. Here it is defined as the universal time (UT), as a fraction of 24 hours, at which the first maximum of the respective wave component, observed at a longitude λ, will pass over Greenwich (zero longitude). This makes the phase $\phi_{n,S}$ dependent upon how fast the maximum of the particular wave travels, also referred to as the phase speed C_{ph} of the wave.

The phase speed of each wave component can be obtained by first setting the argument in the cosine of equation (2.2) equal to a constant, rearranging with respect to λ leaving $\lambda = (-n\Omega t + \phi_{n,S})/S$, and differentiating this expression with respect to t. The phase speed can then be expressed as

$$C_{ph} \equiv \frac{d\lambda}{dt} = -\frac{n\Omega}{S}. \tag{2.3}$$

Several studies have shown that the strongest tidal components are the 8 h, 12 h and 24 h waves (e.g. Hibbins et al. (2006)), and that at mid to high latitudes, the 12 h, or semidiurnal, is the strongest tidal component. A 12 h ($n = 2$) wave with $S = 1$ characterises a semidiurnal westward propagating wave with wavenumber 1 which means that it has a phase speed of $C_{ph} = -2\Omega = -2 \cdot 360^\circ/24\text{h} = -30^\circ/\text{h}$. Hereafter this is referred to as a semidiurnal (or 12 h) S1 component, and it can be seen to be travelling with twice the apparent speed of the Sun. On the other hand a wave with $n = 2$ and $S = 2$ is also a 12 hour westward propagating wave, but it has wavenumber 2 and therefore a phase speed of $-\Omega = -15\,^\circ/\text{h}$. This particular wave will be referred to as a semidiurnal (12 h) S2 wave component. Waves with $C_{ph} = -\Omega$ travel with the apparent motion of the Sun with respect to a ground base observer, and are said to be *migrating* waves. From equation (2.3) it is clear that only waves with $S = n$, like the semidiurnal $S = 2$ component, are migrating. Waves with $S \neq n$, like the semidiurnal S1 component, are said to be *non-migrating* waves. Hence, every temporal wave component has its own migrating spatial component.

2.2.2 Gravity waves

Despite the importance of gravity waves (GW) for atmospheric circulation, detailed below, this thesis will deal primarily with the larger scale tidal and planetary waves. However, a brief discussion of gravity waves is given to explain some of the dynamically controlled features in the mesosphere shown in figure 2.1 and will give further insight into SSWs discussed in section 2.3.1.

Gravity waves are buoyancy waves generated when air is displaced from equilibrium (Hines, 1960). Like the tides, they grow in amplitude as they propagate upward into lower density regions of the atmosphere in order to conserve energy. However, gravity waves have much shorter time and spatial scales. Their periods ranges from minutes to one day with vertical wavelengths in the mesosphere of $2 - 30$ km. Horizontal wavelengths are on the order of tens to thousands of kilometres. Like most waves, they cannot propagate into regions where the background wind is equal or greater than the phase speed of the wave (Fritts, 1984). Thus, GWs are filtered by the mean stratospheric flow when propagating upwards. In winter, the eastward stratospheric wind allows the westward propagating GW to dominate in the mesosphere. In summer, the westward stratospheric wind leads to dominant eastward propagating GW in the mesosphere. Due to their smaller scale sizes, these waves can grow to amplitudes that create local temperature perturbations on the background temperature profile exceeding the adiabatic lapse rate. When this occurs, any air parcels that are displaced upwards by random thermal motion will only expand and cool adiabatically, but be warmer than the surrounding air. Similarly, any parcels that move downward will heat adiabatically but be cooler than the surrounding air. When this occurs, the wave becomes unstable and overturns (or breaks), depositing its momentum and dissipation its energy in the background flow (Lindzen, 1981). This extra momentum, in the direction opposite to the mean wind, acts as a drag force and creates a residual meridional circulation upwards and outwards from the summer pole to the winter pole where the air converges and sinks. The resulting adiabatic heating and cooling creates the warm winter and cold summer mesopause regions shown in figure 2.1.

2.2.3 Planetary waves

A planetary wave (PW) is a large-scale wave with horizontal scales of thousands of kilometres and with periods on the order of days. They are sometimes also referred to as Rossby waves (Andrews, 2010) and play an important role in many large-scale atmospheric phenomena. To understand the way they are created one needs an under-

standing about the conservation of absolute vorticity.

Vorticity refers to the local rotation or spin of some flow, mathematically presented as the curl of the velocity vector of the flow. This is not to be confused with global rotation. In the atmosphere, planetary vorticity (PV) is the vorticity directly caused by Earth's rotation around its axis. At the poles, the vorticity is counter-clockwise and the value of the vorticity here is the maximum on Earth. It gradually decreases towards the equator where it is zero. Vorticity relative to the planetary rotation is here called relative vorticity (RV). Summed together the PV and RV result in the absolute vorticity (Andrews, 2010). Assuming that the horizontal flow is non-divergent at all times (no vertical stretching of the atmosphere in the areas of interest) absolute vorticity is conserved (Paldor, 2008). Thus, changes in either RV or PV, will be compensated for by the other, conserving absolute vorticity. The assumption of non-divergent horizontal flow is not realistic since there are no such restrictions on the vertical displacement of fluids in the atmosphere, but is good enough to get an idea of the dynamics at play when air is displaced in latitude on Earth.

Looking at the northern hemisphere and for simplicity assuming that the initial relative vorticity is zero. A displacement of air toward the North Pole increases the PV counter-clockwise, resulting in a clockwise RV to conserve absolute vorticity. I.e. with respect to the surrounding atmosphere, the displace air is rotating clockwise. This will create a northward air motion to the west of the displaced air and a southward air motion to the east of the displaced air. Due to the viscosity of the air, the rotation of the displaced air will force parcels to its west towards the north, and these will increase their RV clockwise. Similarly, those to the east of the initial displacement will be forced towards the south and will acquire a counter-clockwise RV. Therefore the initial displacement of air is creating a westward propagating wave motion (Stray, 2015). This westward propagating wave is what is characterised as a PW. The phase speed of PWs is always westward relative to the air, so they will not propagate into winds that move westward faster than the phase velocity of the wave.

2.3 Atmospheric coupling

Waves generated in the lower atmosphere can propagate upwards though the atmosphere. The exponential decrease in pressure and the conservation of wave energy causes the waves to increase in amplitude with altitude. When the waves break, they dissipate energy and momentum in the atmosphere. This is the main cause of vertical

coupling of energy and momentum in the atmosphere and this section will focus on some effects of coupling between different parts of the atmosphere.

2.3.1 Sudden stratospheric warmings

A sudden stratospheric warming (SSW) is known as one of the most extreme phenomena happening in the atmosphere. Interaction between the upwards propagating PWs and the zonal-mean zonal flow of the stratosphere (polar vortex) can, due the PWs being westward travelling waves and the polar vortex eastward, weaken the zonal flow and can in extreme cases lead to an abrupt reversal of the zonal-mean winds in the middle atmosphere as well as a sudden warming in the stratosphere and a sudden cooling in the mesosphere (Matsuno, 1971; Limpasuvan et al., 2004). These extreme cases occur in the polar wintertime dominating the variability of the NH wintertime stratospheric circulation (e.g. Andrews et al. (1987)). Large vertical and horizontal velocity and temperature gradients during SSW caused by the altered transmission of PWs and GWs, results in generation of new waves.

Figure 2.3 shows a simulation of the behaviour of the polar cap zonal-mean wind (a) and temperature (b) during a polar cap wind reversal event. In the days prior to the wind reversal, the conditions reflect general winter time conditions (as seen in figure 2.1) with eastward zonal wind in the stratosphere, westward in the mesosphere and with a temperature minimum at the tropopause ($\sim 20\,\mathrm{km}$) and in the mesopause ($\sim$100 km), and a maximum at around 60 km. After the onset (day 0, green vertical line), the zonal wind in the stratosphere reverses abruptly and becomes a westward wind, reflecting summer time conditions. This alters the filtering of eastward waves, and allows for more eastward PWs and GWs to reach the mesosphere. As a result, there is a change in the mesospheric momentum deposition resulting in a change from westward to eastward mesospheric winds. The meridional flow in the mesosphere also changes direction (not shown).

Some of these SSWs are also followed by a nearly isothermal stratosphere, and after the polar vortex starts to recover the stratopause can reform at higher altitudes near 75-80 km and descends over a period of weeks (Manney et al., 2008, 2009). This is known as an elevated stratopause event (ES) and it has been shown that when an SSW is accompanied by an ES event large PWs appear in the MLT (Stray et al., 2015, and references therein).

In the NH, SSWs happen frequently during the winter months. They vary in strength,

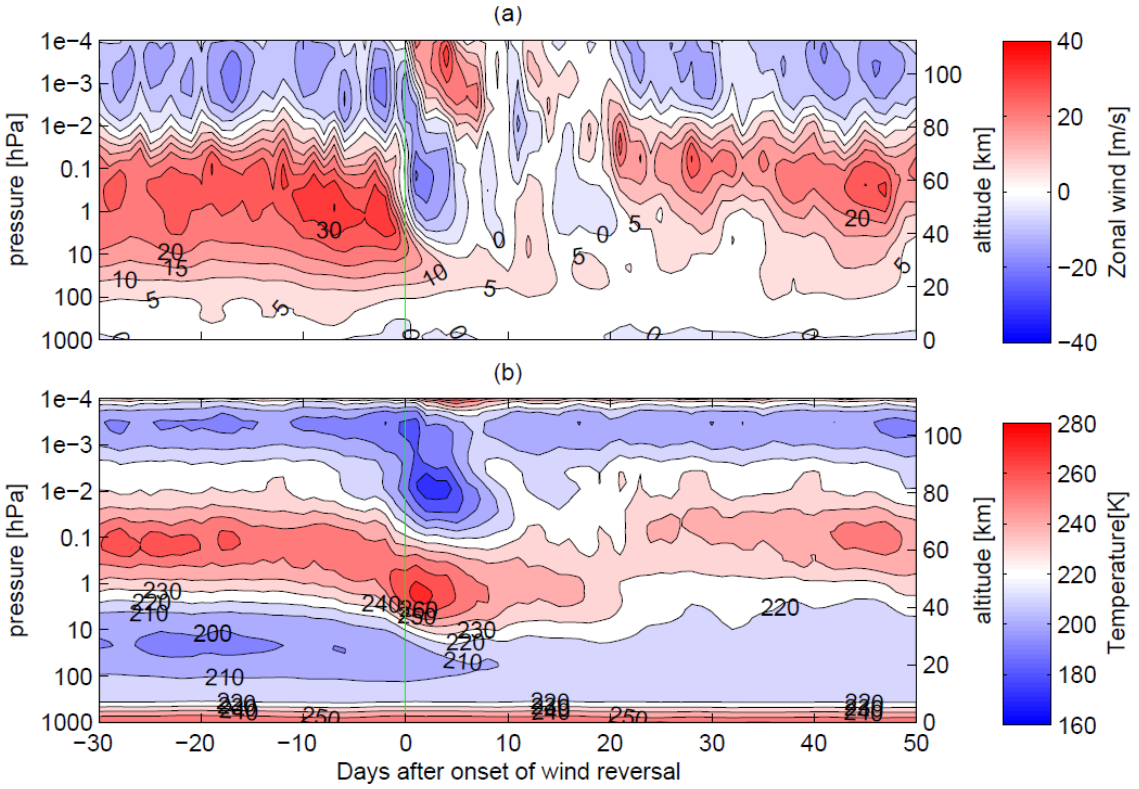

Figure 2.3: Typical polar cap (70-90°N) zonal mean wind (a) and zonal temperature composite (b) from WACCM-SD.

time and duration from year to year, and there are several definitions for SSWs used. The World Meteorological Organization define major SSWs as one that leads to a positive poleward temperature gradient from 60° latitude to the pole at or below 10 hPa ($\gtrsim$ 30 km), and a reversal of the zonal mean wind at 60°N latitude and 10 hPa. If the zonal mean wind does not reverse at that level, it is considered a minor SSW event (Chandran et al., 2013). In recent studies SSW events has been defined using the polar cap temperatures or winds, and the onset of the SSW is defined as the point in time when the zonal-mean zonal polar cap (70-90°N) wind at 0.7 hPa ($\sim$ 50 km) reverse from eastward to westward and persists for at least four days (e.g. (Tweedy et al., 2013; Stray et al., 2015)).

In addition to this, the SSWs are characterized by how the polar vortex breaks. One type is called a *vortex displacement* and is characterized by a clear shift of the polar vortex off the pole. The other is called *vortex split* and refers to a splitting of the polar vortex into two comparable pieces (Charlton and Polvani, 2007). These two types are often associated with a wavenumber 1 for the displacement and a wavenumber 2 for the splitting.

As air flows from the sea over land, the change in topography can displace air in latitude and cause PWs. Thus, the generation of PWs is much larger in the NH than in the SH due to there being more land-sea transitions in the north. Hence, SSWs are much more frequent in the NH compared to the SH.

2.3.2 Solar activity

This section will give a brief overview of how phenomena happening on the Sun can affect and be measured in Earth's atmosphere.

The activity on the Sun is found to have a nearly periodic 11-year cycle (Kutner, 2003). This activity includes e.g. numbers of sunspots, levels of solar radiation, coronal mass ejections (CMEs) and solar flares. Tracking sunspots also reveal a mean rotation period of 27 days for a fixed feature on the Sun to appear at the same apparent position viewed from Earth, called Carrington rotation (Newton and Nunn, 1951).

The Sun is constantly pumping out plasma outward into interplanetary space, and this flow of plasma is known as the solar wind. A coronal hole is a variable solar feature that can last for weeks to months. They are large cells with low densities and unipolar magnetic fields on the Sun's surface with their field lines extending far out into the solar system. This allows an outflow of high-speed plasma from and through the solar corona. During the descending part of the solar cycle, these coronal holes are the dominant phenomenon affecting geomagnetic activity on Earth (e.g. (Tsurutani et al., 2006)). If the coronal holes lasts for more than 27 days, the strong solar winds from the coronal holes will reappear each solar rotation.

The ionosphere is the region of Earth's space environment with the highest plasma density ($\sim 60 - 1000\,\mathrm{km}$) and forms the lowest part of what is known as Earth's magnetosphere. It is produced by the ionization of the neutral atmosphere by x-rays and UV radiation from the Sun. The solar wind interacting with Earth determines the dynamical state of the magnetosphere and ionosphere.

When studying Solar-terrestrial connections an estimate of the dissipation of energy within the magnetosphere at any given time yields information about effects of geomagnetic storms. Geomagnetic activity can be estimated by interpreting magnetometer measurements. To simplify this process and making the data more accessible, several geomagnetic indices has been introduced to give a semi-quantitative measurement of magnetospheric activity. The data used in computation of the indices are obtained

using three component magnetometers either in the local magnetic coordinate system (H, D, Z) or the geographic coordinate system (X, Y, Z). The Z component is the vertical component and is used in both systems, H and X are the horizontal components with H lying in the local magnetic longitudinal plane, and X in the geographic longitudinal plane. D and Y completes the respective right-handed orthogonal systems (Rostoker, 1972).

There are several indices used today, with different purposes. If one wants to study the auroral-zone activity one wants to maximize the contribution from the auroral electrojet in these measurements. This is done with a geomagnetic index called the Auroral Electrojet Index (AE index) first proposed by Davis and Sugiura (1966). The AE index is a function of universal time and is constructed only using the H component measured by subauroral-zone stations providing equally space coverage around the auroral zone. The H component at each observatory is usually measured (in nanotesla, nT) at intervals on the orders of minutes and scaled with regards to a reference level measured on quiet days occurring before and after the period under study (Davis and Sugiura, 1966). The deviations from the reference level, denoted ΔH, is calculated at each station and all values are superimposed onto one another. The upper and lower envelopes represent estimates of the maximum positive and negative deviations occurring along the auroral zone denoted AU and AL respectively. AU and AL are intended to express the strongest current intensity of the eastward and westward auroral electrojets respectively. The separation between AU and AL depends solely upon the maximum eastward and westward auroral electrojet currents and is independent of zonal currents that may exist in the ionosphere, or of the axially symmetric component of magnetic field from any distant sources. Thus

$$AE = AU - AL \tag{2.4}$$

gives a direct measure of the total maximum amplitude of east and west electrojet currents.

There are some problems connected to the AE index that can affect its reliability. Information can be lost during geomagnetic storms when currents are localized in longitude. Hence one cannot rule out sub storm activity only based on low AE index. Also information can be lost if large portions of the electrojet is located at too high latitudes from the AE observatories, or if the auroral oval expands southward away from the stations which it is the case during intense storms (Rostoker, 1972).

Chapter 3

Method

This project is based upon the wind data from 10 radars, called SuperDARN radars, that form a longitudinal chain stretching from 150°W and eastward to 25°E. The hourly mean meridional winds at each station are fitted in 4-day segments to derive a mean wind as well as different tidal components of the wind,. The 4-day windows is shifted in one-day intervals, so that the daily mean winds and tidal amplitudes represent a smoothing over four days. A daily mean meridional wind is calculated and fitted to extract the semidiurnal tide at each station. The longitudinal spread of the stations is used to estimate the spatial part of the semidiurnal tide assumed to consist of two wave components, without spatial-temporal aliasing.

The data gathering, and the first steps of deriving the tidal amplitudes and phases at each station, was done in Stray (2015). Stray was looking at PWs derived from the mean wind, and as a result, the atmospheric tides (i.e. 8 h, 12 h, 24 h sine waves) were extracted from her data, and the 12 h tidal component is used in this study. The next section will be an overview of this initial work and will be followed by the method developed in this thesis. More information on the initial work is found in Stray (2015) as well as in Kleinknecht et al. (2014) and Hibbins and Jarvis (2008).

3.1 Data gathering

3.1.1 SuperDARN Network

The Super Dual Auroral Radar Network (SuperDARN) is an extensive array of high frequency auroral radars located in both the NH and SH, and the stations are widely spread in longitude (Greenwald et al., 1985, 1995). All the operating radars in the NH as of January 2009 and their respective fields of view is shown in figure 3.1. Note that the coordinates in this figure refer to their geomagnetic coordinates. In table 3.1 the coordinates are given in geographic coordinates and are the ones that will be referred to throughout this thesis. The SuperDARN network was developed to study large-scale dynamical processes in the magnetosphere-ionosphere system (Greenwald et al., 1995).

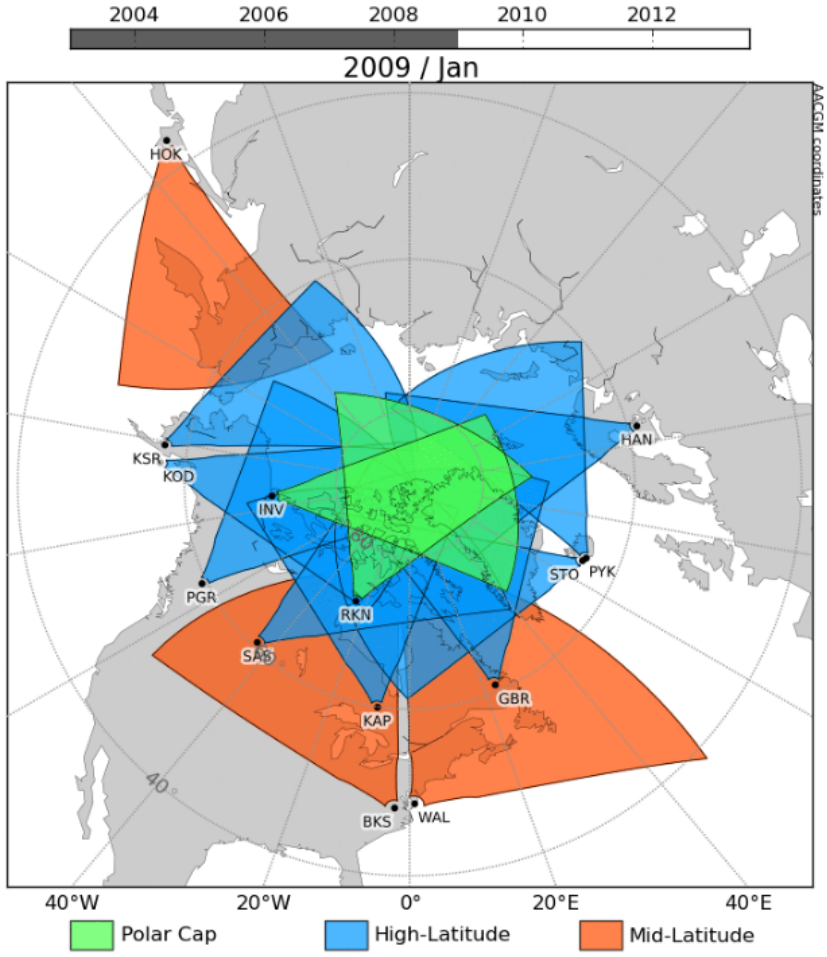

Figure 3.1: Map of all SuperDARN radars in the NH as of January 2009. The radar field of view is shown for all stations. The outermost circle marks 40°N, the second 60°N, and the innermost 80°N in *geomagnetic* latitudes. *Credit*: Virginia Tech SuperDARN website. (Copied with permission from Dr. J. Michael Ruohoniemi)

It was later shown that the echoes received by the radars in the lower range gates are linked to scatter from ionization trails from meteors burning up in the lower and upper mesosphere (Hall et al., 1997). These ionization trails drift with the neutral wind for about a second before they dissipate (Hocking et al., 2001). Tracking the trail therefore yields a line of sight velocity for the mean wind. Line of sight velocities in each of the 16 to 24 beams that cover each radar's field of view are collected for one hour, and a net vector wind with zonal and meridional components is fitted. Because the radars have at least one of their beams directed to the north, but cover only a limited range of longitudes with their field of view, the meridional wind has been shown to be the most accurate (Hibbins and Jarvis, 2008).

While standard SuperDARN radars have no altitude discrimination within the lowest range gates used for meteor-trail detection, the mean altitude of the meteor wind has been estimated to be 94 ± 3 km by comparing the derived wind with the wind

observed by a co-located MF radar (Hall et al., 1997). This has been verified by comparing winds from an imaging Doppler interferometer radar at Halley (74°S, 25°W) and a co-located SuperDARN radar (Hibbins and Jarvis, 2008). The winds from this radar network provide an hourly snapshot of the wind as a function of longitude, and this gives a great amount of insight into the dynamics of the MLT.

Since the radars detect the short-lived ionization trails against the background ionosphere, the extra ionization cause by auroral ionization at $\sim 90\,\mathrm{km}$ (the E region) can reduce the contrast between the trail and the background. Thus, the meteor count rate can drop during auroral precipitation, and if too few meteors are observed to fit a wind, it will result in data gaps.

3.1.2 SuperDARN stations used

The data analysis is done using the 10 radars listed in table 3.1. Figure 3.1 shows all the operating stations in the NH as of January 2009. To be able to calculate the zonally propagating tides in the NH, stations that are spread out in longitude is needed. The SuperDARN stations listed above form a band of radars ranging in longitude from King Salmon at 158.5°W to Hankasalmi at 25.2°E, and in latitude from Kaupasking 51.4°N to Pykkvibaer at 65.7°N. This means that King Salmon and Hankasalmi are 1.7° away from being on the exact opposite side of the Earth and that the maximum latitudinal spread of the stations is 14.3°. The longitudinal difference between Hankasalmi and Kodiak is 176.3°, 3.7° from 180° separation. All stations have coverage during 2000-2008, except King Salmon and Rankin Inlet which started operating in 2001 and 2007 respectively.

Table 3.1: SuperDARN Radars used in the Data Analysis. Abbreviations in table is from (Chisham et al., 2007) and the official website of `vt.superdarn.org`.

Radar names	Abbrev.	Lat. [°]	Long. [°]	Start Year
Hankasalmi	han	64.4	25.2	1995
Pykkvibaer	pyk	65.7	-18.0	1995
Stokkseyri	sto	64.7	-26.9	1994
Goose Bay	gbr	55.5	-60.3	1983
Kaupasking	kap	51.4	-83.3	1993
Rankin Inlet	rkn	65.0	-92.9	2007
Saskatoon	sas	54.2	-105.2	1993
Prince George	pgr	56.1	-123.2	2000
Kodiak	kod	59.5	-150.1	2000
King Salmon	ksr	60.6	-158.5	2001

3.2 Data analysis

To obtain the S1 and S2 components of the semidiurnal tide, the wind data from the SuperDARN radars are processed through several steps. The process of quality checking and least-squares fitting the data to provide the mean wind, 8 h, 12 h and 24 h tidal components along with the 48 h wave is explained in detail in Kleinknecht et al. (2014), but for completeness the main points are repeated in section 3.2.1. The resulting wave amplitudes and phases for the meridional component of the 12 h daily mean wind at the locations of the SuperDARN radars are then used to fit the S1 and S2 components as explained in section 3.2.2.

3.2.1 Extracting the tidal components from the hourly wind for each station

Hourly averaged neutral meteor winds are obtained from SuperDARN's data access site at the British Antarctic Survey. The SuperDARN radars have between 16 and 32 adjacent 1 degree wide beams arranged in a fan shaped array (see figure 3.1). Since most of the radars point towards the North Pole, they cover only a limited range of angles in the zonal direction. Thus, the meridional component of the wind solved from all the line-of-sight Doppler velocities has higher accuracy (Hibbins et al., 2010). Hence, only the meridional component of the wind is used. Hourly mean winds above 100 m/s, winds with standard deviation of zero or a mean location different from the geometric centroid of the beams are excluded. These values are either unrealistic or suggest non-standard operation mode of the radar.

To extract the tidal amplitudes of the hourly mean wind a 4-day window is used with the fitting function

$$V(t) = A_0 + \left[\sum_{j=1}^{3} A_j \sin\left(\frac{2\pi j}{24\text{h}}t + \phi_j\right)\right] + A_4 \sin\left(\frac{2\pi}{48\text{h}}t + \phi_4\right) \tag{3.1}$$

to extract the amplitude of the mean wind A_0, the amplitude A_i and phase ϕ_i of the 24 hour ($i = 1$), 12 hour ($i = 2$), 8 hour ($i = 3$) and 48 hour ($i = 4$) component of the hourly mean wind V as a function of time t in hours. The 48 h is the quasi-two day PW, while the 8 h, 12 h and 24 h are the tidal components. Of these tidal components e.g. Manson et al. (1989) and Hibbins et al. (2006) have shown that the 12 h semidiurnal tide is the strongest component at high latitudes.

The segment window is then moved one day at a time and the above components

are again fitted if there is enough data covering each hour of the day, as done in Hibbins and Jarvis (2008). These results in a 4-day average of the daily mean meridional wind as well as the tidal amplitudes and phases for each day when the associated 4-day window contains enough hourly mean data. The resulting amplitudes typically have uncertainties of approximately $\pm 2.5\,\mathrm{m/s}$.

Tidal amplitudes will vary as a function of latitude (Murphy et al., 2006). In tidal theory these variations are defined by Hough functions (Forbes, 1995). However, over the latitude range covered by the SuperDARN radars used, 14.3°, the latitudinal variation of the tide may be seen to be on the same order as the measured uncertainties. Following Hibbins et al. (2010) and Baumgaertner et al. (2006), the theoretical variation of amplitude with latitude in the analysis is neglected.

Standard SuperDARN radars cannot determine the altitudes of meteor trails measured in the lowest range gates (Kleinknecht et al., 2014). However comparison with the other range-finding meteor radars as done in Hibbins and Jarvis (2008) indicate that the observations are most representative of the winds at $\sim 95\,\mathrm{km}$.

3.2.2 Deriving S1 and S2

As discussed in section 2.2.1 a 12 h wave can be represented as a sum of an infinite number of 12 h wave components, given by the zonal wavenumber S. Earlier studies has shown that the S1 and S2 are the largest components, and this leads to the assumption that the total semidiurnal tidal field can be represented by the vector sum of only a S1 and S2 component (Hibbins et al., 2010).

Using all available SuperDARN stations given above, one can fit data from several longitudes to derive the amplitudes A_{S1} and A_{S2} along with the phase difference Φ_{diff} of the meridional component of the semidiurnal tide for each day with enough stations available. This method is detailed in section 3.2.2.1. Mainly for validation another method is also used developed by Baumgaertner et al. (2006) using two stations located approximately 180° from each other in longitudes. This method will be detailed in section 3.2.2.2.

3.2.2.1 Multiple station fitting method

When assuming that the 12 h tide consists of only a wavenumber 1 (non-migrating) wave propagating westward with twice the apparent speed of the Sun, and a wavenum-

ber 2 (migrating) wave, this is equivalent to equation (2.2) with $n = 2$ and only choosing $S = 1$ and $S = 2$. The basic equations of the semidiurnal S1 and S2 can then be written as

$$f(t,\lambda) = A_{S1}\cos\left(\frac{2\pi}{12}t + \frac{2\pi}{360}\lambda - \phi_{S1}\right) + A_{S2}\cos\left(\frac{2\pi}{12}t + \frac{4\pi}{360}\lambda - \phi_{S2}\right). \tag{3.2}$$

Here A_{S1} and A_{S2} are the amplitudes, and ϕ_{S1} and ϕ_{S2} are phases for the S1 and S2 respectively. λ is the longitude east of Greenwich (0°E). The phase is given in radians. Typically the phase is given in UT, as it will be in this thesis. In the equations it will be given in radians for simplicity. The conversion from radians to UT for a semidiurnal tide is given by $\phi_i^{UT} = (12\text{h} \cdot \phi_i^{rad})/2\pi$. The phase is the time of maximum (TOM) in UT of the first maximum after midnight passing over Greenwich. If the maximum of the S1 wave is at longitude $\lambda = 90°$ at midnight, keeping in mind that the S1 travels with a speed of 30°/h westward, it would take 3 hours before the maximum pass over Greenwich. Hence its phase is 3 UT ($= \pi/2$). Note that even though the S1 travels with twice the speed of S2, the temporal argument is the same. This is due to S2 having two maxima. For the S2 the TOM at each longitude λ is the same as the TOM at 0°E since it is a migrating component.

At a fixed longitude, λ_i, equation (3.2) can be written as

$$f(t) = A_{S1}\cos\left(\frac{2\pi}{12}t + \Phi_{S1}\right) + A_{S2}\cos\left(\frac{2\pi}{12}t + \Phi_{S2}\right), \tag{3.3}$$

where

$$\Phi_{S1} = \frac{2\pi}{360}\lambda_i - \phi_{S1}, \tag{3.4}$$

$$\Phi_{S2} = \frac{4\pi}{360}\lambda_i - \phi_{S2}. \tag{3.5}$$

Using $\cos(a+b) = \cos a\cos b - \sin a\sin b$, equation (3.3) can be written as

$$f(t) = A_{S1}\left[\cos\left(\frac{2\pi}{12}t\right)\cos(\Phi_{S1}) - \sin\left(\frac{2\pi}{12}t\right)\sin(\Phi_{S1})\right] \tag{3.6}$$

$$+ A_{S2}\left[\cos\left(\frac{2\pi}{12}t\right)\cos(\Phi_{S2}) - \sin\left(\frac{2\pi}{12}t\right)\sin(\Phi_{S2})\right]. \tag{3.7}$$

Recognizing the shared time dependent factors and factorizing yields

$$f(t) = A(\lambda)\cos\left(\frac{2\pi}{12}t\right) + B(\lambda)\sin\left(\frac{2\pi}{12}t\right), \tag{3.8}$$

where

$$A(\lambda) = A_{S1}\cos(\Phi_{S1}) + A_{S2}\cos(\Phi_{S2}) \tag{3.9}$$

and

$$B(\lambda) = -A_{S1}\sin(\Phi_{S1}) - A_{S2}\sin(\Phi_{S2}). \tag{3.10}$$

The amplitude of $f(t)$ is now given by

$$A_{12}(\lambda) = \sqrt{A(\lambda)^2 + B(\lambda)^2}, \tag{3.11}$$

and the phase is given by

$$\Phi_{12} = \arctan\left(\frac{B(\lambda)}{A(\lambda)}\right). \tag{3.12}$$

There is no time dependence in neither amplitude nor phase, but they vary at each longitude λ_i. Inserting equation (3.4) and (3.5) into equation (3.9) and (3.10) and simplifying the result yields

$$A(\lambda) = A_{S1}\cos\left(\frac{2\pi}{360}\lambda_i - \phi_{S1}\right) + A_{S2}\cos\left(\frac{4\pi}{360}\lambda_i - \phi_{S2}\right), \tag{3.13}$$

and

$$B(\lambda) = -A_{S1}\sin\left(\frac{2\pi}{360}\lambda_i - \phi_{S1}\right) - A_{S2}\sin\left(\frac{4\pi}{360}\lambda_i - \phi_{S2}\right). \tag{3.14}$$

Inserting these into equation (3.11) yields the amplitude of the semidiurnal tide

$$A_{12}(\lambda) = \sqrt{A_{S1}^2 + A_{S2}^2 + 2A_{S1}A_{S2}\cos\left(\frac{\pi}{180}\lambda_i + (\phi_{s1} - \phi_{s2})\right)}. \tag{3.15}$$

Here $\sin^2 a + \cos^2 a = 1$, $\cos a\cos b + \sin a\sin b = \cos(a-b)$ and $\cos(-a) = \cos(a)$ has been used. Inserting equation (3.13) and (3.14) into (3.12) and simplifying yields the phase of the semidiurnal tide as

$$\Phi_{12}(\lambda) = \arctan\left(\frac{-A_{S1}\sin\left(\frac{\pi}{180}\lambda_i - \phi_{S1}\right) - A_{S2}\sin\left(\frac{\pi}{90}\lambda_i - \phi_{S2}\right)}{A_{S1}\cos\left(\frac{\pi}{180}\lambda_i - \phi_{S1}\right) + A_{S2}\cos\left(\frac{\pi}{90}\lambda_i - \phi_{S2}\right)}\right). \tag{3.16}$$

For a data set consisting of amplitude and phase of the semi-diurnal tide at several longitudes, one can use a non-linear least-squares fit to perform a curve fit of the function A_{12} in equation (3.15) with A_{S1}, A_{S2} and $\Phi_{\text{diff}} = \phi_{S1} - \phi_{S2}$ as free parameters. Since mathematical solutions to this fitting function also includes negative amplitudes and phase difference outside the interval $\pm 2\pi$, a limitation to the output parameters to be within 0 and 100 m/s for the amplitudes and $\pm 2\pi$ for the phases is set. The limit of 100 m/s is only set to give the fitting amplitude an upper limit. Amplitude readings stronger than this value are not realistic.

Equation (3.16) can also be used to obtain the S1 and S2 parameters. It would however yield a more complicated fitting routine due to the larger number of unknowns and the discrepancy in both the Φ_{12} and the individual phases of the wavenumber components. Hence equation (3.15) is used.

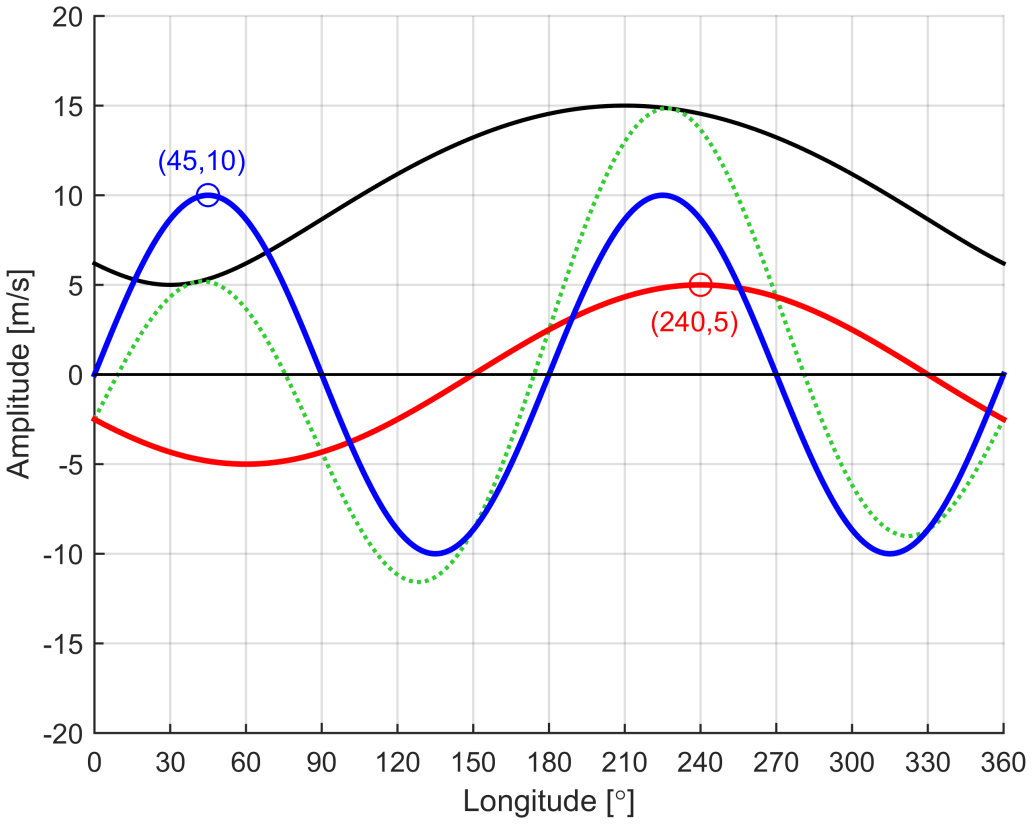

Figure 3.2: Connection between semidiurnal tide (dotted green line) when assuming that it is only the sum of the S1 (red) and S2 (blue) components. The black line shows the amplitude A_{12} in obtain from equation (3.15). The amplitude of the S1 and S2 is set to 5 m/s and 10 m/s,

Figure 3.2 shows an example of how this amplitude function (black curve) may look for a given S1 wave (red curve) and S2 wave (blue curve). The sum of the two components is given by the green curve and is equal to the semidiurnal tide when only assuming S1 and S2 components. In this example $A_{S1} = 5\,\mathrm{m/s}$, $A_{S2} = 10\,\mathrm{m/s}$. As mentioned earlier the phase is given as the UT time when the first maximum is at 0° longitude. This examples shows the maximum of the S1 at 240 ° longitude, and the first maximum of the S2 at 45 ° longitude. Assuming this example is a snapshot at $t = 0$ (midnight), the S1, moving at -2Ω, will pass over 0° longitude at 8 UT, and the S2, moving at $-\Omega$ will pass over 0° longitude at 3 UT. Hence $\phi_{S1} = 8\,\mathrm{UT}$ and $\phi_{S2} = 3\,\mathrm{UT}$ yielding

$\Phi_{diff} = \phi_{S1} - \phi_{S2} = 5\,\mathrm{UT}$ for this example.

There are some problems connected to this fitting function, which should be addressed. One is that the fitting function is symmetric with respect to A_{S1} and A_{S2}. I.e. the fitting function can compute different values for the amplitudes, but it has no way of knowing which value that corresponds to which component. To be able to separate the components, starting values for the free parameters are needed. The process described in section 3.2.2.2 yields estimates for both amplitude and phase for the individual S1 and S2, and these are used as starting points for the curve fitting routine. This means that the two methods are not completely independent of one another. The method presented in section 3.2.2.2 is used as a validation of the method presented here. There is also a problem connected to the confidence intervals produced by the fitting routine when $A_{S1} \approx A_{S2}$. This will be addressed in section 3.3.

3.2.2.2 Validation method

In order to validate the aforementioned fitting method, a method published in Baumgaertner et al. (2006) is used for comparison. The main idea presented in that publication is repeated here for completeness. The technique uses the amplitude and phase of the 12 h tide at two stations separated by approximately 180° in longitude. The S1 component has wavenumber 1, meaning that it has a wave crest and a wave trough separated by 180° longitude. For the S2, the wavenumber 2 component with two wavelengths around the Earth, the two crests are separated by 180°.

One can represent amplitude and phase with vectors in a phasor diagram. The length of the vectors represent the amplitude, and the angle represents the phase in TOM at a given longitude λ. Here the positive vertical axis is defined as 0 UT, and the phase increases clock-wise around the origin.

For the 12 h S1 and S2 at a longitude λ_A we define $\vec{S_1}$ and $\vec{S_2}$ respectively describing both the amplitude and phase of the respective wavecomponents. These vectors are shown in figure 3.3 (left) where the phase of the S1 is set to zero at longitude λ_A for simplicity, and the phase of the S2 is arbitrarily set. Assuming that S1 and S2 are the only components present, one can express the total semidiurnal tide at λ_A as

$$\vec{A} = \vec{S_1} + \vec{S_2}. \tag{3.17}$$

The S1 phasor repeats every 360° while the S2 phasor repeats every 180°. At a longitude $\lambda_B = \lambda_A + 180°$, the S1 will have its TOM 6 hours later, hence its phasor representation

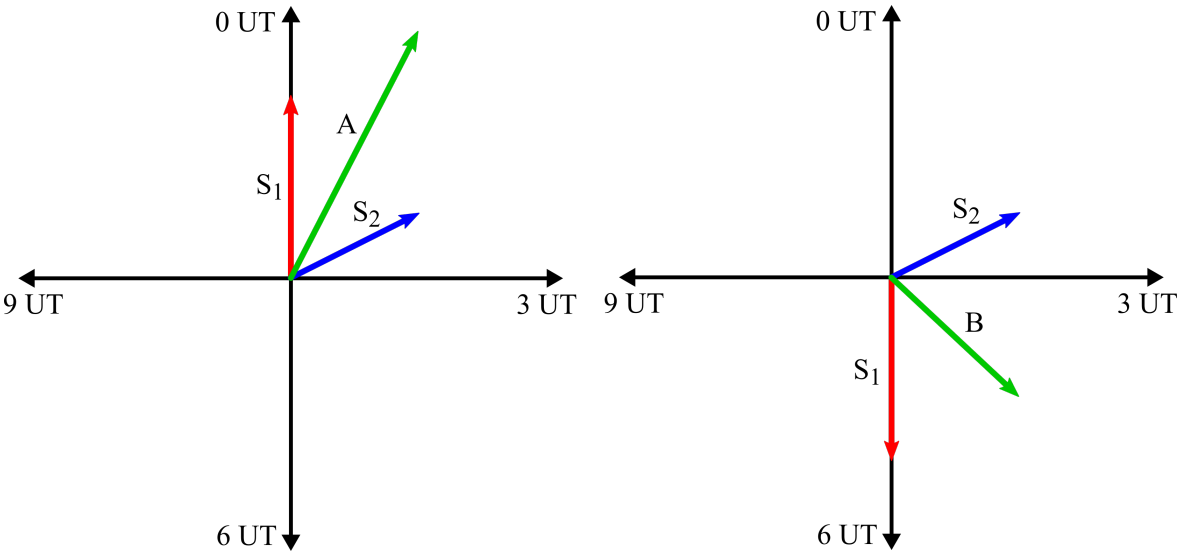

Figure 3.3: Phasor diagram illustrating semidiurnal tide at longitude λ_A (left), and at $\lambda_B = \lambda_A + 180\,^\circ$ (right) showing the wavenumber 1 (S1) and 2 (S2) amplitudes (length of vector), and phase (angle clockwise away from 0 UT). Each quarterly phase is illustrated with black arrows and their respective values. The vector sum of $\vec{S_1}$ and $\vec{S_2}$ is shown as $\vec{A}$ and $\vec{B}$ for the two different locations. After Baumgaertner et al. (2006).

will be $-\vec{S_1}$. The S2 will have a maximum at λ_B at the same time as at λ_A, so the phasor of the S2 will be the same as at λ_A. This is shown in figure 3.3 (right). The total 12 h tide at λ_B can then be expressed as

$$\vec{B} = -\vec{S_1} + \vec{S_2}. \tag{3.18}$$

$\vec{A}$ and $\vec{B}$ can be determined from radar measurements. Using equation (3.17) and equation (3.18) the vector representations of S1 and S2 can be expressed as

$$\vec{S_1} = \tfrac{1}{2}(\vec{A} - \vec{B}), \tag{3.19}$$

$$\vec{S_2} = \tfrac{1}{2}(\vec{A} + \vec{B}). \tag{3.20}$$

There is a small correction for stations whose separation is not 180°. Defining a vector $\vec{C}$ which describes the 12 h wave at $\lambda_C = \lambda_B + \gamma$, where γ is the deviation from 180° longitudinal separation from λ_A. This yields the phase of S1 and S2 at λ_C as $\theta_1 + \gamma + \pi$ and $\theta_2 + 2\gamma$ as shown in figure 3.4, where θ_1 and θ_2 is the phase of the S1 and S2 at λ_A.

Note that Baumgaertner et al. (2006) has made an error concerning the phases at λ_C, saying that the phases should be $\theta_1 + \pi + \gamma$ and $\theta_2 + \gamma/2$ for S1 and S2 respectively. Baumgaertner (personal communication, 2015) has confirmed this error. Luckily the deviation γ used in Baumgaertner et al. (2006) is fairly small (13.1°) meaning that this does not change his results too much.

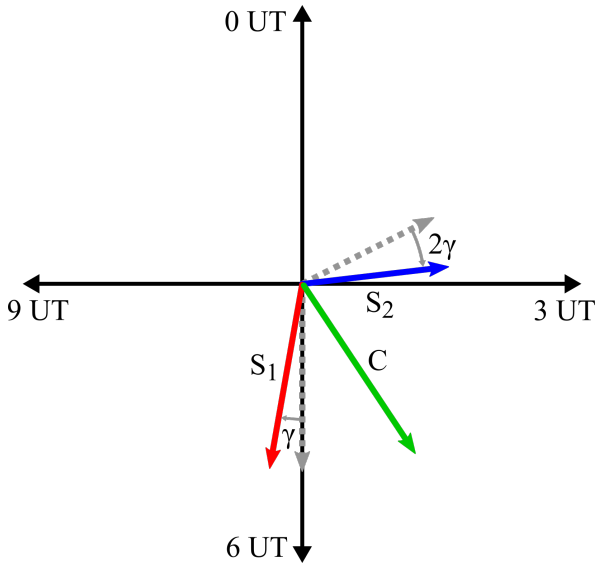

Figure 3.4: Same as figure 3.3 only at longitude $\lambda_C = \lambda_B + \gamma$. C is the amplitude of the vector sum of the $\vec{S_1}$ and $\vec{S_2}$. After Baumgaertner et al. (2006).

$\vec{C}$ can be expressed using polar coordinates in terms of $\vec{S_1}$ and $\vec{S_2}$, and the equations can be inverted to give the S1 and S2 amplitudes in terms of the observed amplitudes, phases, λ_A and λ_C.

This method is based upon the approximation that the S1 and S2 components of the semidiurnal tide are dominant. Since all phasors for waves with odd wavenumbers will be exactly the opposite when shifted 180° and all phasors for waves with even wavenumbers will be equal when shifted 180°, odd and even wavenumber components will effectively add themselves to the S1 and S2 respectively. This however is only accurate when $\gamma = 0$. Hence, the error in this assumption increases with γ. Nevertheless, enough prior studies has shown that the S1 and S2 components of the semidiurnal tide are dominating the wavenumber spectrum in the MLT.

3.3 Error analysis

This section is not crucial to understand the results of this thesis, but is included to explain why error bars are not included in the results and validate that the high confidence intervals are practical problem with the fitting routine and does not represent the uncertainties in the data presented in chapter 4.

Firstly in section 3.3.1 the particular problem connected to the confidence interval is presented. These problems leaves the confidence intervals from the fitting routine unreliable and practically difficult to use as error bars. In section 3.3.2 the values

of the fitting routine is however shown to produce satisfactory results using synthetic data. The results are shown to be better than the two-station method for about 95% of the cases. Hence, it is argued that the uncertainty in the fitting routine should not be larger than the uncertainty in the two-station method. A heuristic error analysis technique is presented in section 3.3.3, and it is used to estimate the uncertainty in the two-station method. These values are then extrapolated to be estimates of the uncertainty in the fitting routine. The estimated uncertainties of the actual data is presented in section 4.3.

3.3.1 Confidence interval from fitting routine

The least-squares fit, in addition to produce values for the free parameters, produces confidence intervals for each parameter. The 95% confidence interval represents values for the particular parameter for which the difference between the parameter and the observed estimate is not statistically significant at the 5% level (Cox and Hinkley, 1979). The standard deviation σ is approximately a quarter of the width of 95% confidence interval when Gaussian distributed errors are assumed.

The synthetic data is created by choosing values for $(A_{S1}^{in}, A_{S1}^{in}, \phi_{S1}^{in}, \phi_{S2}^{in})$ and using equation (3.15) to calculate A_{12} and (3.16) to calculate Φ_{12} for 8 of the longitudes corresponding to the SuperDARN radars in table 3.1 (rkn and ksr excluded). A_{12} is then added to a Gaussian distributed white noise with variance 4 to simulate real values. These synthetic data points for the semidiurnal tide are used to fit $(A_{S1}^{out}, A_{S2}^{out}, \Phi_{diff}^{out})$ using the fitting routine explained in 3.2.2.1. The input and output data can be found in table 3.2 and the belonging figure 3.5 for two different examples. The fitting routine produces for the most part satisfactory values where the input values are included in the standard deviation, with relative deviations less than 1, when A_{S1} is not approximately equal to A_{S2}. When the $A_{S1}^{out} \approx A_{S2}^{out}$, as seen in table 3.2, the standard deviations are many orders of magnitude larger than the particular center value. This only happens when the output amplitudes are similar. The frequency of large σ when $A_{S1}^{out} \approx A_{S2}^{out}$ is reduced when the number of stations are increased, but still at over 100 equally spread stations, $\sigma \geq 1000$ is still produced when the output amplitudes are very similar. Nonetheless, the amplitude values seems to correspond well with the input data, even though the confidence intervals are very big. This makes the standard deviations from the fitting routine unusable. Disregarding the uncertainties in the data is not something that should be done lightly, as data is of no significance without error estimates. Therefore, a validation of the fitting method is needed, to make sure that the data can be trusted even without the error estimates from the fitting routine. This

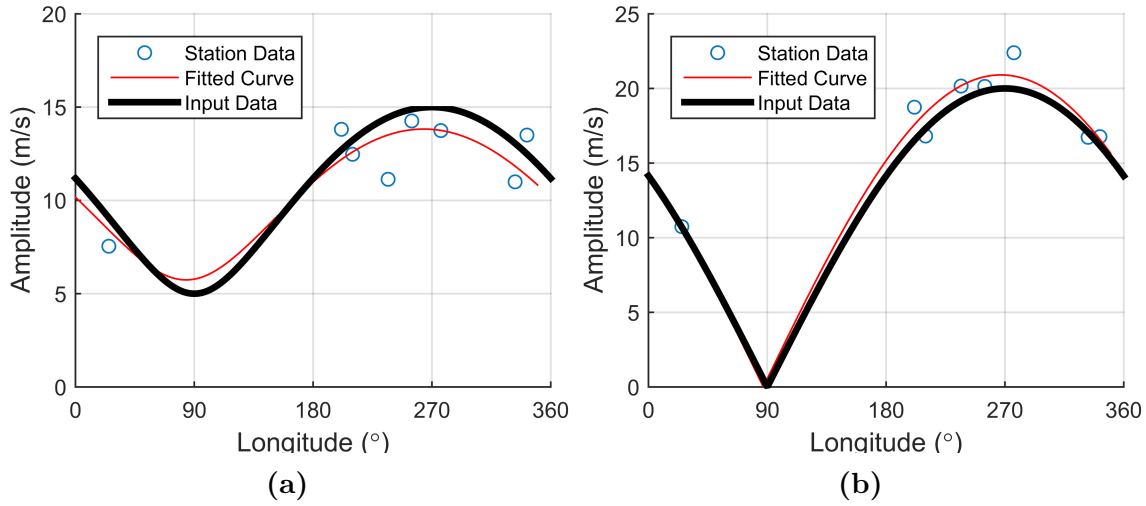

Figure 3.5: Examples of fitting results using synthetic data (black line), added Gaussian white noise at eight longitudes (blue circles) corresponding to longitudes of eight of the SuperDARN radars used. The red line is the result from the non-linear curve fitting routine explained in section 3.2.2.1.

is done in section 3.3.2.

Table 3.2: Shows examples of the output (value ± standard deviation, superscript *out*) when fitting synthetic data from eight longitudes created by the input data (superscript *in*) added Gaussian noise.

Figure	$(A_{S1}^{in}$	A_{S1}^{in}	$\Phi_{diff}^{in})$	$(A_{S1}^{out} \pm \sigma_1$	$A_{S2}^{out} \pm \sigma_2$	$\Phi_{diff}^{out} \pm \sigma_\Phi)$
3.5a	(10	5	1.57)	$(9.78 \pm 2.50$	4.04 ± 3.12	$1.68 \pm 0.39)$
3.5b	(10	10	1.57)	$(10.14 \pm 1.24$E4	10.14 ± 1.24E4	$1.36 \pm 0.30)$

3.3.2 Validating the method

It is hard to validate a method, because it demands an insight into what you are trying to determine in the first place. Hence there is not always a good way of knowing if the obtained results are close to the real values. A way around this is to start by creating results that are within the ballpark of the expected results, and work backwards creating the input data. Then, adding an appropriate distribution of noise to the input data and sending it through the routine yields a way of comparing how close the obtained results are to the created results. This can be obtained using the method of generating synthetic data that is explained in section 3.3.1, but instead of choosing the input data, drawing it from an appropriate distribution.

Here A_{S1}^{in} and A_{S2}^{in} is drawn from a uniform distribution between 0 and 25. ϕ_{S1}^{in} and ϕ_{S2}^{in} is drawn from a uniform distribution between 0 and 2π. Figure 3.6 shows the deviation

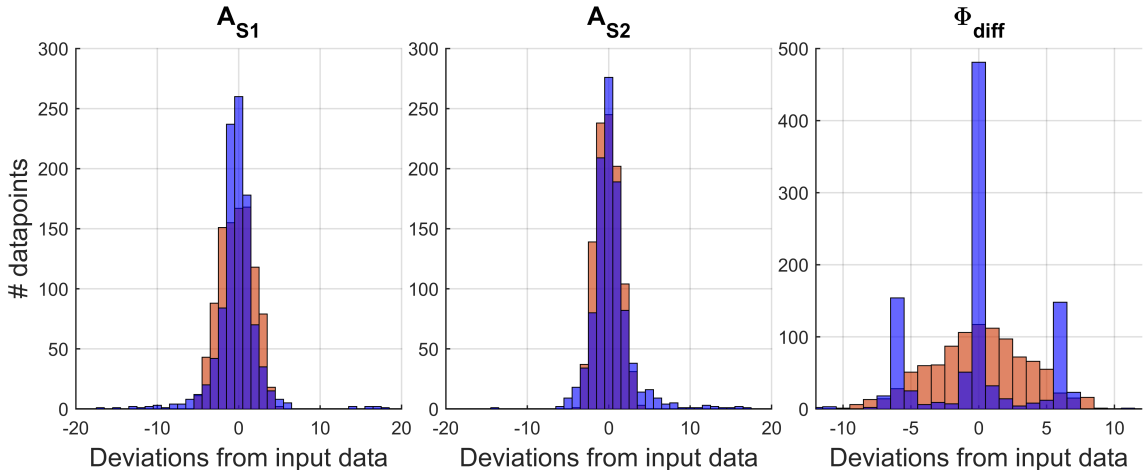

Figure 3.6: Comparison between the fitting routine (blue) and the two-station method (orange) using synthetic data of the S1 (left) and S2 (middle) amplitudes, and the phase difference (right). Units of amplitudes in m /s and the phase difference is given in radians.

from the input data, i.e. $(A_{S1}^{in} - A_{S1}^{out},\ A_{S2}^{in} - A_{S2}^{out},\ \Phi_{diff}^{in} - \Phi_{diff}^{out})$, for the two-station method (orange) and the fitting routine (blue) obtained by repeating the process 1000 times.

All parameters for both methods are fairly symmetric around zero. There are a few cases, for both A_{S1} and A_{S2}, where the fit gives large deviations. However for A_{S1} the fit produces better data than the two-station method for about 95% of the cases. For A_{S2}, the results from the two methods are quite similar apart from the larger deviations in the fit for about 5% of the data points. The fit produces results with roughly equal quality for both wave components, but the two-station method has larger deviations in A_{S1} compared to A_{S2}. From this $\pm\sigma$ (interval centred on 0 containing $\sim$ 68% of the data points) is estimated to be roughly ± 2.5 m/s for both amplitudes when the input data is added a Gaussian noise with standard deviation 2 m/s. Hence, this test suggests that the uncertainty in the output amplitude data (from the fit and the two-station method) should not increase dramatically with respect to the uncertainty in the semidiurnal data from the SuperDARN stations.

Φ_{diff} from the two-station method is centred around zero, but the values are quite spread out. Φ_{diff} from the fit is within ± 0.5 rad ($\approx \pm 1$ UT) of the input data for almost 50% of the data and has symmetric large peaks at $\pm 2\pi$. It is not as easy to quantify the change in uncertainty for the phase, since the scaled Gaussian distribution is only added to the amplitude data. The 2π discrepancy in the phase is likely caused by the 2π discrepancy of the phase in the fitting function.

This suggests that the fitting routine produces better amplitude results for roughly 95% of the cases. Combined with the much better phase resolution, the fitting routine values seems to yield satisfactory results. This is as expected since the fitting routine uses more stations than the two-station method.

Reducing the number of stations (i.e. data points in fit) for A_{12} and Φ_{12} to four (with longitudes corresponding to han, pyk, kap and kod). The fit preforms roughly the same for the amplitudes as the two-station method, but the phase performance is still much better for the fit. Hence the uncertainty in the two-station method would work as estimates of the uncertainty in the fitting routine. In the next section, a heuristic error analysis method is presented, which estimates the standard deviation in the two-station method.

3.3.3 Heuristic error analysis

To estimate the error in the two-station method heuristic error analysis can be used. It refers to a method of analysing the uncertainty in a function by drawing a given numbers of data points from a Gaussian distribution, using the actual input data point as a mean μ_{in}, and the standard deviation σ_{in} of the data as the standard deviation of the Gaussian distribution, and send every combination of the drawn numbers through the function. Calculating σ_{out} for the output parameters gives an idea of how the uncertainty changes as a function of the uncertainty in the input data.

This is used on the two-station routine explained in section 3.2.2.2. For one given day 10 numbers are drawn from a Gaussian distribution setting each of the 4 free variables (A, C, θ_A, θ_C) for that day as the means of each distribution and their respective σ's as the σ_{in} in the distribution and sending every possible combination of those numbers through the routine. This results in 10^4 different outputs. Calculating the average and standard deviation of the outputs yields an an estimate of the uncertainty in the output data. This can be repeated for each day.

The standard deviation will change based on which input numbers are drawn. Relative standard deviations ρ, defined as

$$\rho_{S1} = \frac{\sigma_{S1}}{\langle A_{S1} \rangle}, \quad \rho_{S2} = \frac{\sigma_{S2}}{\langle A_{S2} \rangle}, \tag{3.21}$$

will make it possible to compare the estimated errors for each day. Here $\langle ... \rangle$ refers to the mean of the amplitude. $\rho \geq 1$ suggest that the data points are just noise. Since $\sigma_{\Phi_{diff}}$ is not expected to scale with Φ_{diff} the relative standard deviations of the phase

difference will not be meaningful. $\sigma_{\Phi_{Diff}}$ will give better insight into the uncertainty.

As mentioned earlier, since the fitting routine is expected to preform similarly as the two-station method, it is also expected to have similar uncertainties. Hence, the relative standard deviations will be an estimate of the uncertainty in the fitting function.

Chapter 4

Results and analysis

To perform the following calculations *Matlab R2014b* was used. Presented and discussed first is the amplitude and phase of the semidiurnal tide followed by the data coverage for each station. The multiple station fitting routine explain in section 3.2.2.1 is then used on the semidiurnal tide data to produce the daily amplitude and phase values for the S1 and S2 wavecomponent presented in section 4.4.1. The 9 years (2000 – 2008) of data is used to form a climatology of each of the wavecomponents which is used to obtain yearly anomaly amplitude data (de-seasonalized data). All of this is then used to look at how the S1 and S2 behaves during SSWs (section 4.5.1), and the AE is investigate as a possible generation mechanism of the S1 component by correlating the S1 amplitudes and anomaly amplitudes with the *AE* index (section 4.5.2). The results obtained with the two-station method is also included in the S1 and S2 amplitude and phase plots for validation, and the results of the heuristic error analysis is presented in section 4.3.

4.1 Amplitude and phase of the semidiurnal tide

As part of her dissertation work, Stray (2015) used the procedure explained in section 3.2.1 on the raw wind data gathered by each of the SuperDARN radars to produce a mean wind, and the 8 h, 12 h, 24 h and 48 h components of the wind. An example of the results obtained from this is shown in figure 4.1 where the raw wind data recorded with the SuperDARN radar Hankasalmi (64.4°N, 25.2°E) is used to calculate the monthly average fitting results for the meridional components of the wind.

Figure 4.1 shows that the mean meridional wind from Hankasalmi is equatorward during summer and poleward during winter. The amplitude of the 2-day wave is strongest around the summer solstice, and minimum around both equinoxes. The 24 h wave amplitude is quite constant at around 5 m/s throughout the year. The 8 h amplitude is almost zero during spring and summer, with an incoherent phase during that time. The resulting monthly mean of the meridional amplitude for the 12 h tide shows the strongest amplitudes of all the tidal components, and has a maximum around the fall

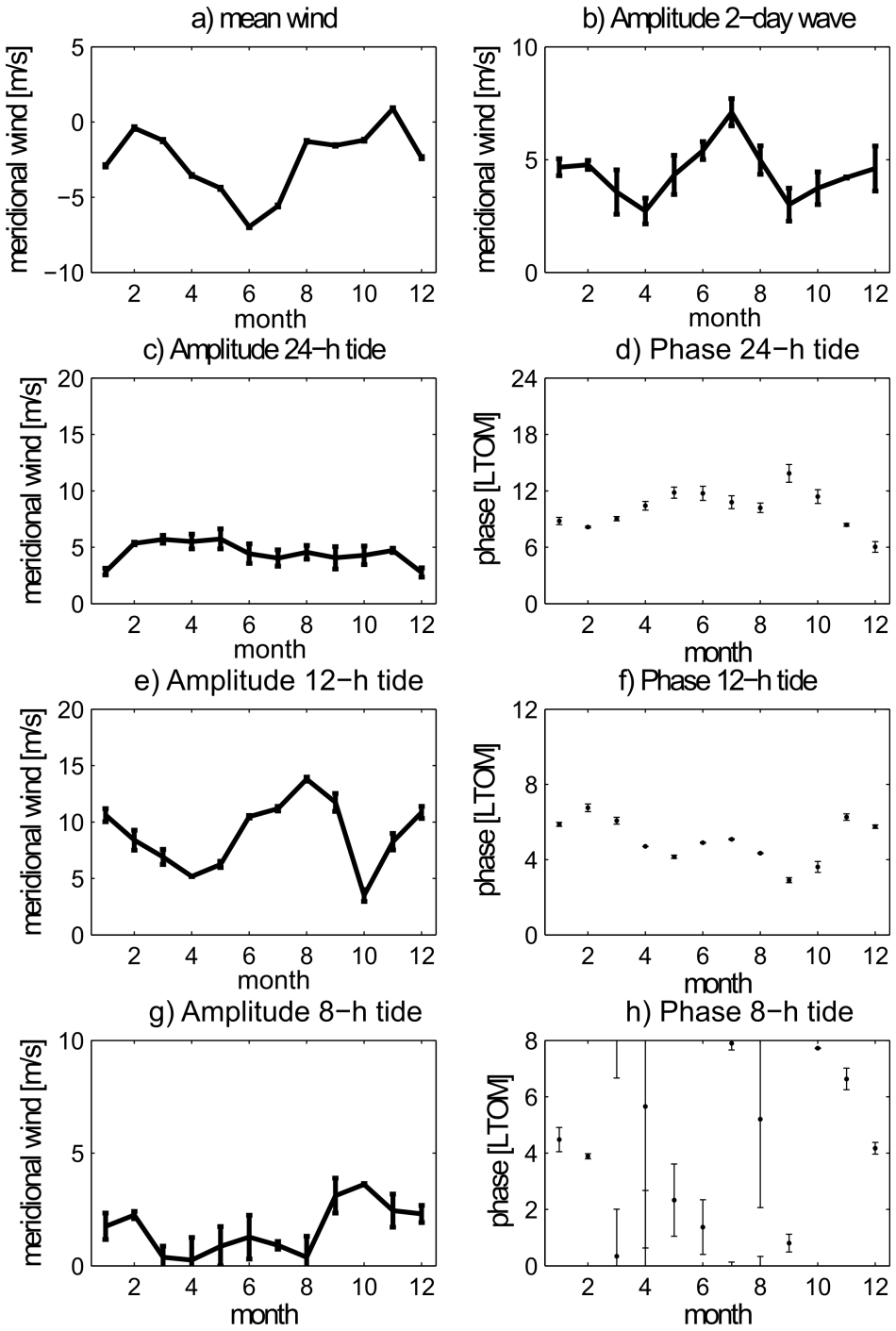

Figure 4.1: Monthly weighted average recorded with the Hankasalmi SuperDarn radar showing the a) meridional mean wind, b) meridional 2-day wave wind, c) amplitude- and d) phase of the 24 h tide, e) amplitude and f) phase of the 12 h tide, and g) amplitude- and h) phase of the 8 h tide. The phases are given in local time of maximum. The error bars shows the standard error of the weighted means. From Stray (2015).

equinox and winter and summer solstice, and minima around spring equinox and early winter. The corresponding local time of maximum occurs earlier at the amplitude minima.

There were some days where the relative error at the stations were above 100%. This means that the data is basically just noise. This did not affect many days, and hence it should not be a big problem, however these days are not excluded from the data presented later.

4.2 Data coverage of the semidiurnal tide

The daily coverage for each of the 10 SuperDARN stations given in table 3.1 from 2000 – 2008 is shown in figure 4.2. The horizontal lines shows the dates coverage for the station indicated along the vertical axis. The abbreviations are explained in table 3.1. The coverage of han and kod is blue to easily mark the two stations used to perform the two-station method.

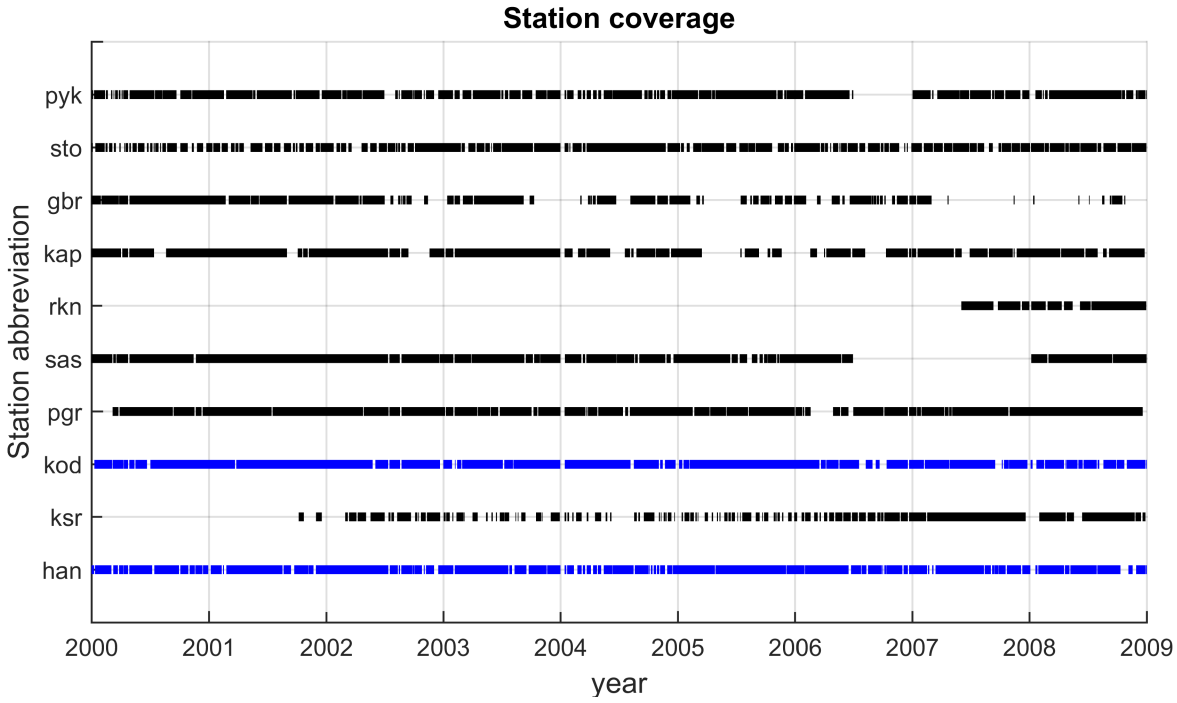

Figure 4.2: Data coverage of semdiurnal tide for each individual station used from 2000-2008. Each horizontal line indicates the data coverage for the station whos abbreviation is placed along the vertical axis. The ticks along the horizontal axis indicates the start of the year indicated.

Even though some stations have large consecutive periods of downtime (e.g. Saskatoon has a gap of 558 days between June 26th 2006 and January 7th 2008), the total

number of stations for each day is generally good. Table 4.1 shows the distribution of the available number of stations during the 9 years. About 75% of the total number of days are covered by more than 6 stations.

Of the total 3288 days in the period from the beginning of 2000 to the end of 2008, han and kod covers a total number of 2940 and 3000 days respectively. 2726 of these days are covered by both of the two stations. All of the 2726 are also covered by at least two additional stations. Hence, both of the two methods can be calculated for the same days.

Table 4.1: Distribution of number of stations in total data coverage.

Number of stations	0	1	2	3	4	5	6	7	8	9	10
Frequency	20	13	7	15	58	194	516	950	1097	387	31

4.3 Error analysis of S1 and S2 data

Due to the nature of the uncertainties in the data of the S1 and S2 of the semidiurnal tide, the estimated uncertainties are presented and discussed first. As expected from the synthetic data testing in section 3.3 when the S1 and S2 amplitudes are similar, the fitting routine produces 95% confidence intervals many orders of magnitude larger than the resulting data points. Figure 4.3 shows a histogram of $\log_{10}(\sigma)$ from A_{S1}, A_{S2} and Φ_{diff}. E.g. for the A_{S1} there are 1455 data points with σ between 1 m/s and 10 m/s, and 420 datapoints with σ between 10^4 m/s and 10^5 m/s. The histogram for the A_{S1} and A_{S2} is identical for $\sigma > 10^2$. These are the points where the A_{S1} and A_{S2} are too close for the fitting function to separate them. This is be discussed further in chapter 5, after the amplitudes are presented.

The resulting relative error estimates ρ, calculated using method in section 3.3.3, for A_{S1} and A_{S2} is calculated and the minimum, maximum and median of ρ for each year is presented in table 4.2. Combining all years yields a median of the relative error estimate of 0.2 for both the S1 and the S2 component, which for a wave amplitude of roughly 10 m/s would represent an error of roughly ± 2 m/s.

Based on the results presented in this section and the results from the synthetic data test. The standard deviations of the S1 and S2 amplitude can be estimated to be in the

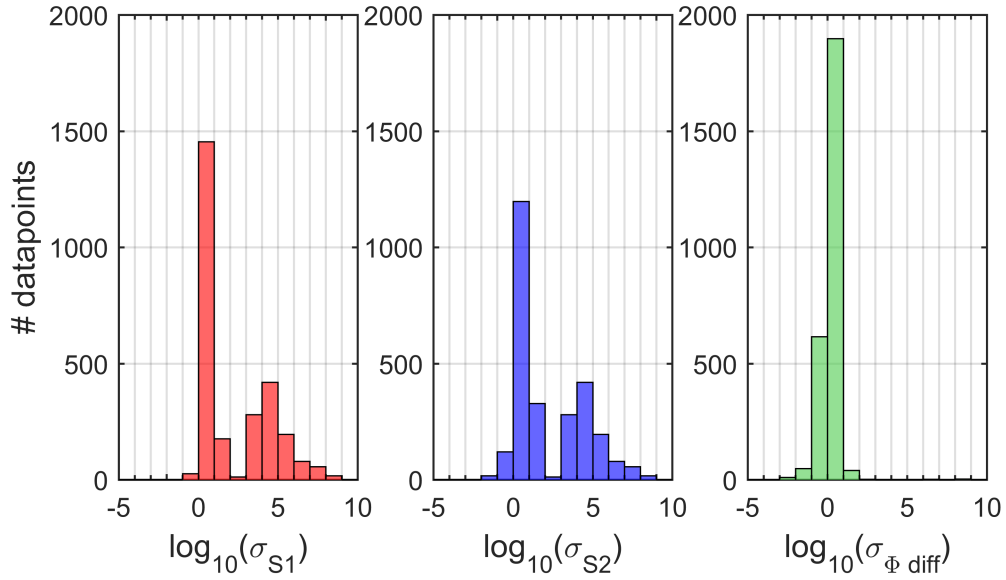

Figure 4.3: Histogram of the standard deviation σ of A_{S1} (red), A_{S2} (blue) and Φ_{diff} (green) from fitting routine using $\log_{10}(\sigma)$. The units for σ for A_{S1} and A_{S2} are m/s and radians for the Φ_{diff}.

Table 4.2: Results from heuristic error analysis outlined in section 3.3.3 showing the minimum, maximum and median of the estimated relative error ρ for A_{S1} and A_{S2}, and for the estimated error in the phase difference $\sigma_{\Phi_{diff}}$ for each year. $\sigma_{\Phi_{diff}}$ is given i hours. Numbers are rounded to nearest tenth.

Year	ρ_{S1}			ρ_{S1}			$\sigma_{\Phi_{diff}}$		
	min	max	median	min	max	median	min	max	median
2000	0.1	0.7	0.2	0.1	0.8	0.1	0.1	9.7	1.2
2001	0.1	0.8	0.2	0.0	0.6	0.2	0.1	9.2	1.1
2002	0.1	0.8	0.2	0.1	0.8	0.2	0.1	8.4	1.2
2003	0.1	0.7	0.2	0.0	0.6	0.2	0.0	9.9	0.9
2004	0.1	0.8	0.2	0.0	0.7	0.1	0.1	8.6	0.9
2005	0.1	0.8	0.2	0.0	0.7	0.1	0.0	9.9	0.6
2006	0.0	0.7	0.2	0.0	0.6	0.2	0.0	8.8	0.6
2007	0.1	0.7	0.2	0.0	0.7	0.2	0.1	7.4	0.9
2008	0.0	0.8	0.2	0.0	0.7	0.2	0.1	11.2	1.2

$\pm 2 - 3$ m/s range, hence one the same order as the uncertainty in the meteor radars. The uncertainty in the phase seems to be roughly ± 1 h.

4.4 Amplitudes and phases of the S1 and S2

This section shows the results obtain by using the fitting routine explained in section 3.2.2.1. The results of the validation method, explained in section 3.2.2.2 will also be included in this section. The method explained in the latter is dependent upon two stations separated by close to 180° in longitude. Of the 10 SuperDARN radars

which covers the period from 2000 – 2008 on roughly the same latitude, Hankasalmi and King Salmon are closest to this (1.7° deviation), but as figure 4.2 shows, the King Salmon radar was not operational until the end of 2001. Therefore Hankasalmi and Kodiak (separated by 4.7° longitude) are used. The separation between Hankasalmi and Kodiak is relatively small compared to other studies. E.g. both Baumgaertner et al. (2006) and Hibbins et al. (2010) used the Scott Base (a MF spaced antenna radar at 77.8°S, 166.7°E) and Halley (a SuperDARN radar at 75.8°S, 26.4°W) yielding a longitudinal separation from 180° of 13.1° which, together with the two-station method, gave good results.

4.4.1 S1 and S2 meridional wind amplitude

The daily meridional wind amplitudes of the S1 and S2 wavecomponents from 2000 to 2008 are shown in appendix A. Only data from a couple years are shown in this section to save space but still give a good view on the different results obtained with the two methods and show the inter-annual variability.

Due to the effects explained in section 3.3 errorbars are not included in the plots. In chapter 5 the results will be quantitatively compared to those calculated using the two-station method. Results from both methods will be presented in this section, but only data from the fitting routine will be used in section 4.4.4 and 4.5.

Figure 4.4 and 4.5 shows the resulting meridional amplitudes for the semidiurnal S1 and S2 respectively for the year 2000 and 2008. The red and blue lines represents the S1 and S2 respectively using the multiple station method, and the gold and green lines represents the S1 and S2 data respectively using the two-station method. Lines are only drawn when subsequent days has enough data to produce a fit. Hence, data gaps will be shown as gaps in the plots.

S1 amplitudes for 2000 in figure 4.4a shows a small maximum localized around the fall and in mid-December, and has a minimum around mid-summer and early spring. The correlation between the two methods seems good around the fall equinoxes and when the amplitudes are high, and diverge more in March, April and May.

In figure 4.4b the results are quite similar as for 2000. The maxima around the fall is still present and around 15 m/s, but the maximum in December seen in 2000 is not present in 2008. Generally, the maximum of the S1 seems to be located around the fall equinox peaking at around 15 m/s. The oscillation of the amplitude is also noteworthy.

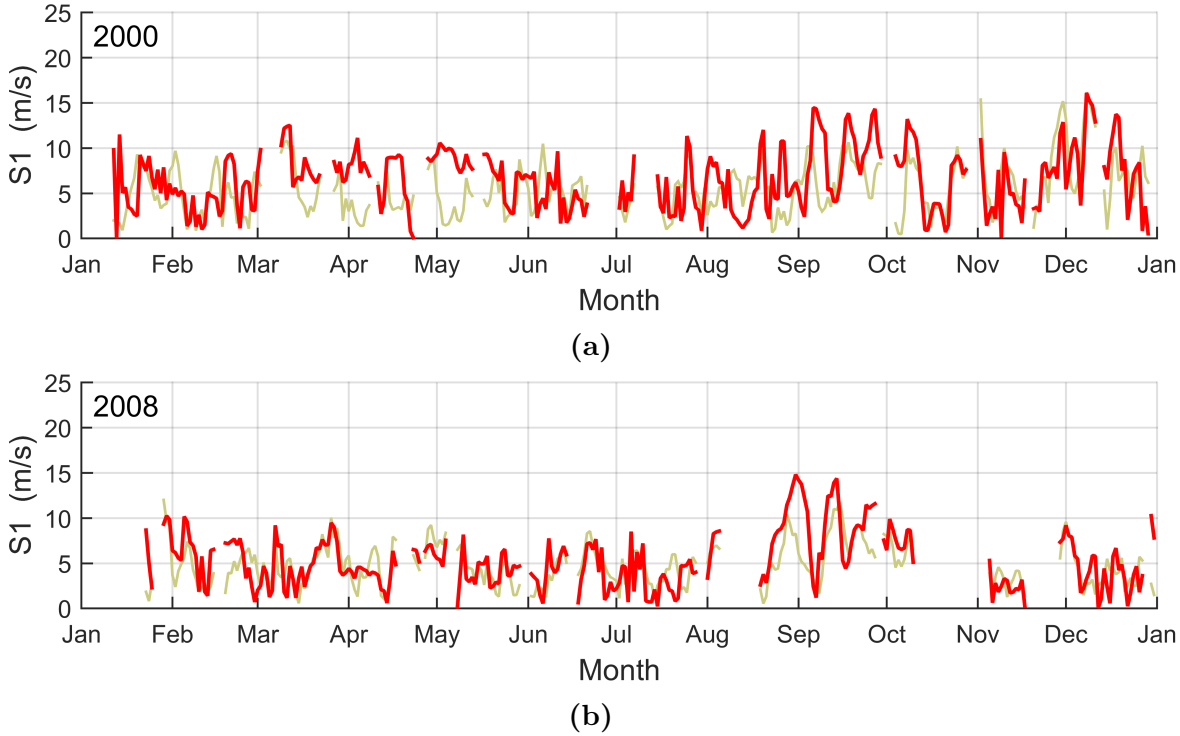

Figure 4.4: Plot of the semidiurnal S1 amplitude from 2000 **(a)** and 2008 **(b)**. The red line shows the amplitude from the fit and the gold line is from the two-station method.

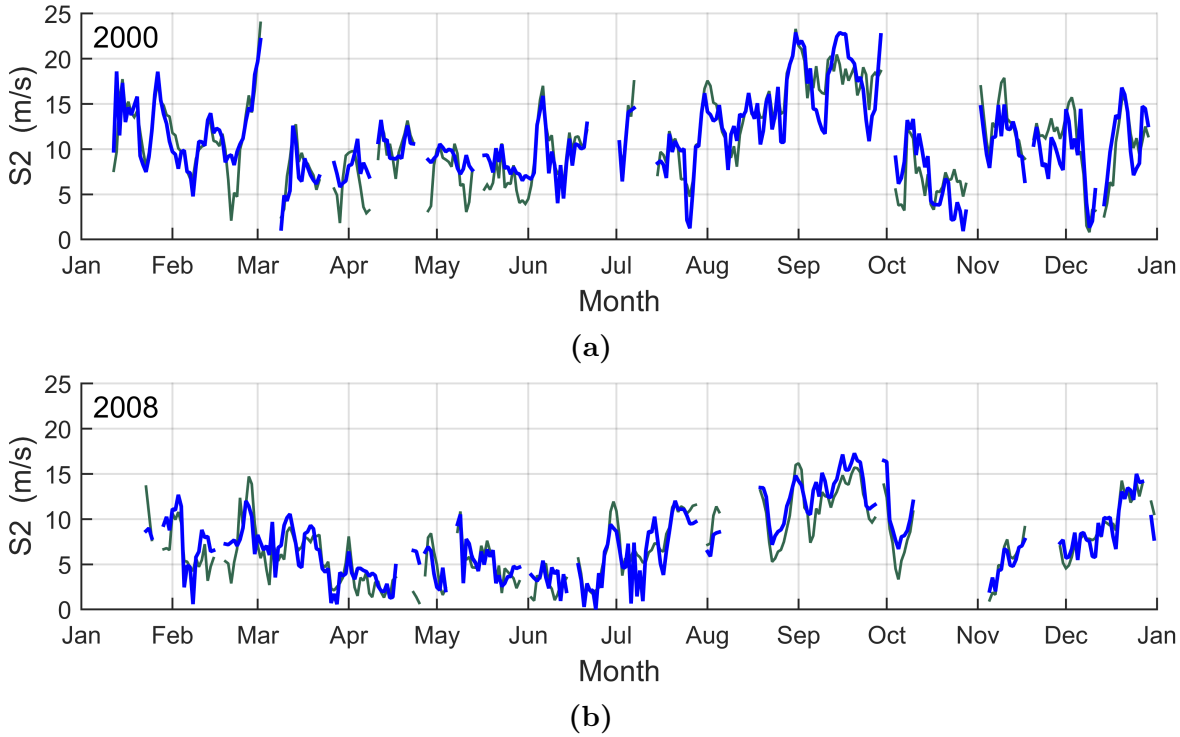

Figure 4.5: Same as in figure 4.4 only for the S2. Blue line shows the amplitudes from the fitting routine, and the green is from the two-station method.

There is seldom a period of time longer than around 10 days before the amplitude sharply drops of by around 50% This is more frequent on the last half of the year. The peak around fall equinox is not as strong as for the two-station method.

The S2 amplitudes reaches higher maximum amplitudes than the S1 as shown in figure 4.5, and they are larger and more persistent. In figure 4.5a the maxima of the amplitude is located around the beginning of March and in the middle of September with amplitudes close to 25 m/s showing for both methods. The maximum in March has a rapid increase and drop off spanning over roughly 20 days. Whereas the amplitude around September has an amplitude increase from the end of June and a drop off in amplitude into the start of November.

In figure 4.5b the largest peak remains around the fall equinox but the maximum is smaller than in 2000 as it maximises at just above 15 m/s. The maximum in March in figure 4.5a is not apparent in 2008 and neither in any of the other years of data. The frequency of low amplitudes is highest in spring and early summer, and again in early winter. The amplitude seems to generally increase in the course of the winter and reach local maxima around the beginning of the new year. When comparing the two methods for the S2 component, the difference between the resulting amplitudes seldom surpasses 5 m/s, and like the S1 it looks to be better at larger amplitudes. As can be seen from these two years, the amplitude of the S2 varies quite a lot from year to year. Large oscillations is also noted in the S2, similar to the S1.

4.4.2 S1 and S2 phases

The numerical values of the individual phases is defined as the time in UT after midnight at which the first maximum of the respective wave component will pass over Greenwich. The fitting routine outputs $\Phi_{diff} = \phi_{S1} - \phi_{S2}$. The two-station method produces the individual phases (ϕ_{S1} and ϕ_{S2}). The phases of the individual wavecomponents for 2000 and 2005 is given in figure 4.6 where the phases are repeated over three cycles to more easily show coherence. 2005 is here included because it contains a high number of data points that will make the comparison easier.

Even though the data points for each day is calculated independently, the calculated phase is relatively stable from day to day showing a degree of continuity. The ϕ_{S1} (red cirlces) in 2000 and 2005 seems to vary around 0 UT with largest variation during spring and fall equinoxes. Compared to 2005 ϕ_{S1} in 2000 varies more rapidly in the first half of the year, but both years have rapid variation from April to June. Shared

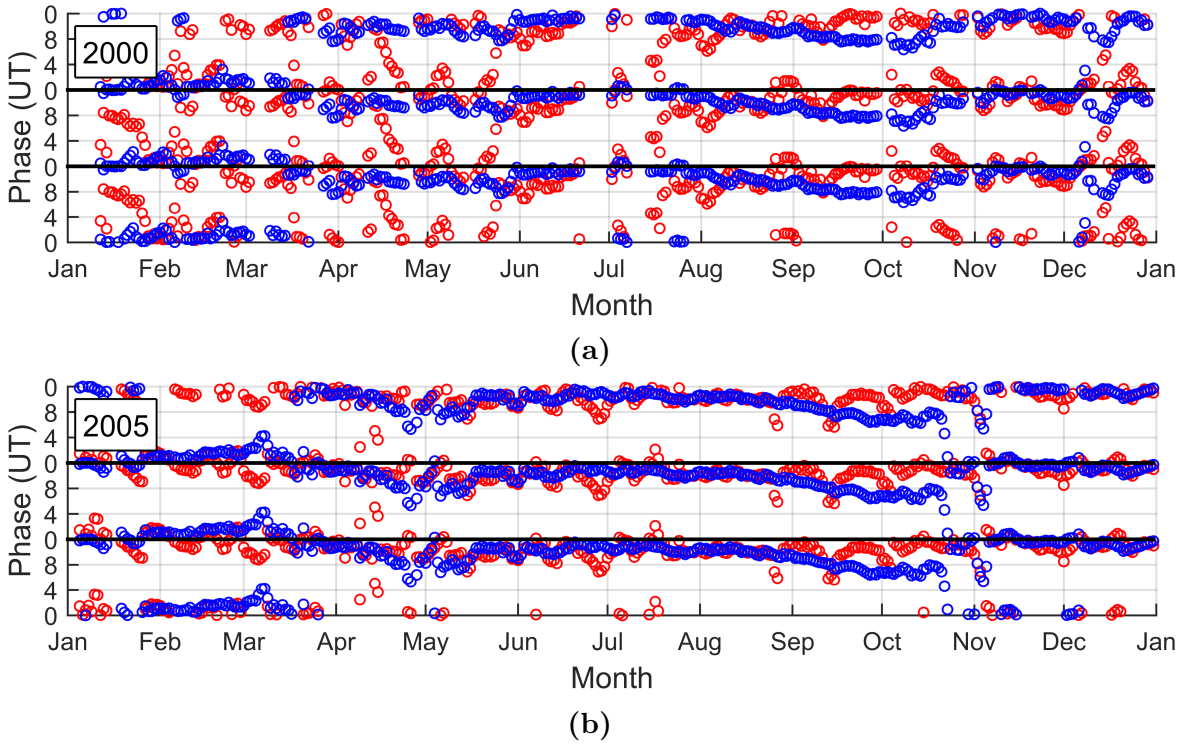

(a)

(b)

Figure 4.6: Phases from two-station method given in UT for the S1 (red circles) and S2 (blue circles) for the year 2000 **(a)** and 2005 in **(b)**. The phases are repeated over three cycles to show coherence.

characteristics are also noted for ϕ_{S2} (blue circles) for the years shown, varying around the same values as ϕ_{S1}, 0 – 2 UT during summer and winter solstice, and around 6 – 10 UT during spring and fall equinoxes.

The Φ_{diff} from the fitting routine for 2000 and 2005 is plotted in figure 4.7. The rest is included in appendix C. Also included is the phase difference ($\Phi_{diff} = \phi_{S1} - \phi_{S2}$) from the two-station method for validation. On first glance the data from 2000 seems very chaotic, and instead of being quite continues, as the individual phases, it has sharp jumps by roughly ± 12 h. This happens each time only one of the individual phases crosses 0 UT. E.g. if both ϕ_{S1} and ϕ_{S2} increases with 3 UT, ϕ_{S1} from 11 UT to 2 UT and ϕ_{S2} from 5 UT to 8 UT, the phase difference changes from $\Phi_{diff} = 6$ UT to $\Phi_{diff} = -6$ UT, even though the relative changes in the individual phases is the same. Since the Φ_{diff} values of the two methods mostly does these jumps at the same time, it can be extrapolated that the individual phases from the fitting functions would correspond well with those of the two-station method, if they could be fitted. Φ_{diff} seems constant around 0 UT and ± 12 UT during summer and winter, meaning that the S1 and S2 are in phase. Around the equinoxes, the phase seems to be out of phase more often. More variation is noted in 2000 than in 2005.

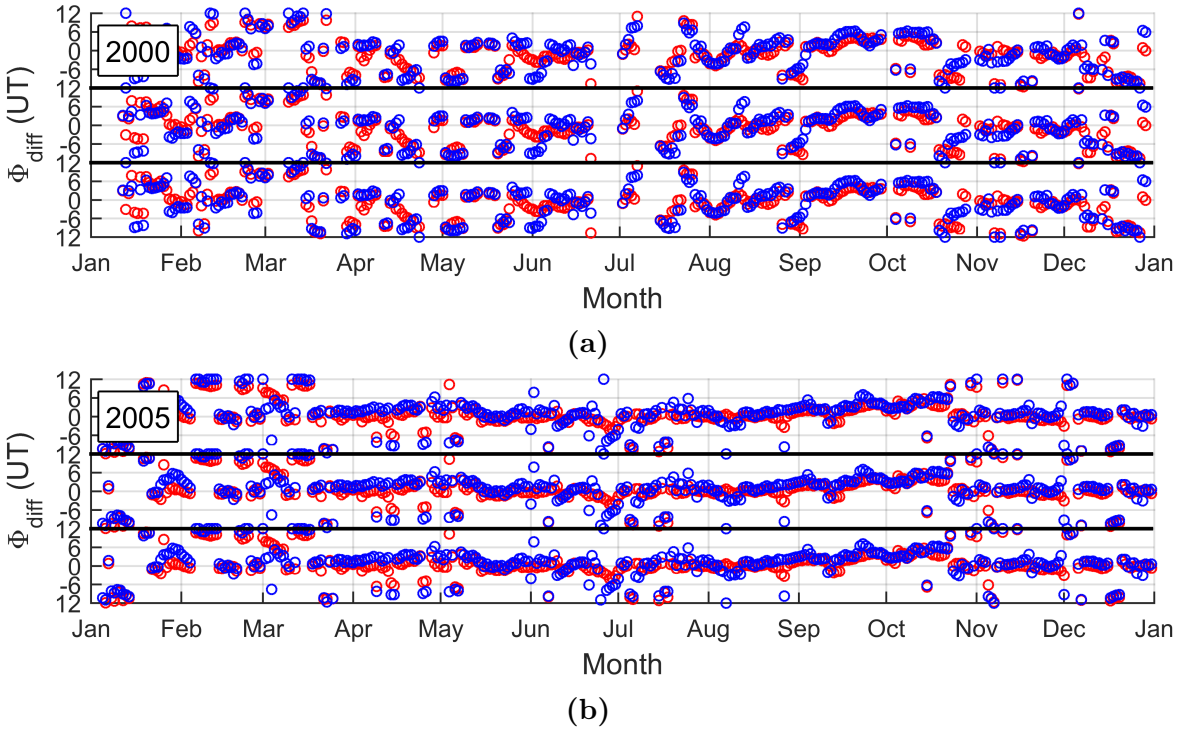

Figure 4.7: Phase difference ($\Phi_{diff} = \phi_{S1} - \phi_{S2}$) given in UT produced by the multiple station fitting routine (blue circles) and the two-station method (red circles) for the year for 2000 in **(a)** and 2005 in **(b)**. The phases is repeated over three cycles to show coherence.

4.4.3 Climatology of the S1 and S2

Seasonal effects seems to be causing large changes in the amplitudes. Hence eliminating the seasonal variability would make it easier to study if there are other driving forces. Using all years of amplitude data, an average year can be calculated. An appropriate smoothing of the average year will reduce the different inter-annual effects that differ from year to year and result in an estimate of general annual trends, called the *climatology*. This can later be used for calculating *anomalies* which here refers to divergences within a year from the climatology, yielding the inter-annual changes not directly related to the seasonal cycle.

The average year of the S1 and S2 is shown in figure 4.8 along with a plot showing the number of available years for each day of the average year. To calculate the climatology a 31-day running mean smoothing is used on the average years to smooth the data. The mean year is repeated three times, and the data for each day is replaced by the mean of the 15 days each side of it. This represents a boxcar average. This is shown by the red solid line in figure 4.9. The smoothing is repeated a second time, resulting in an effective triangular smoothing function extending 30 days each side of a given day. This smoothed data is shown as the black solid line in figure 4.9. While

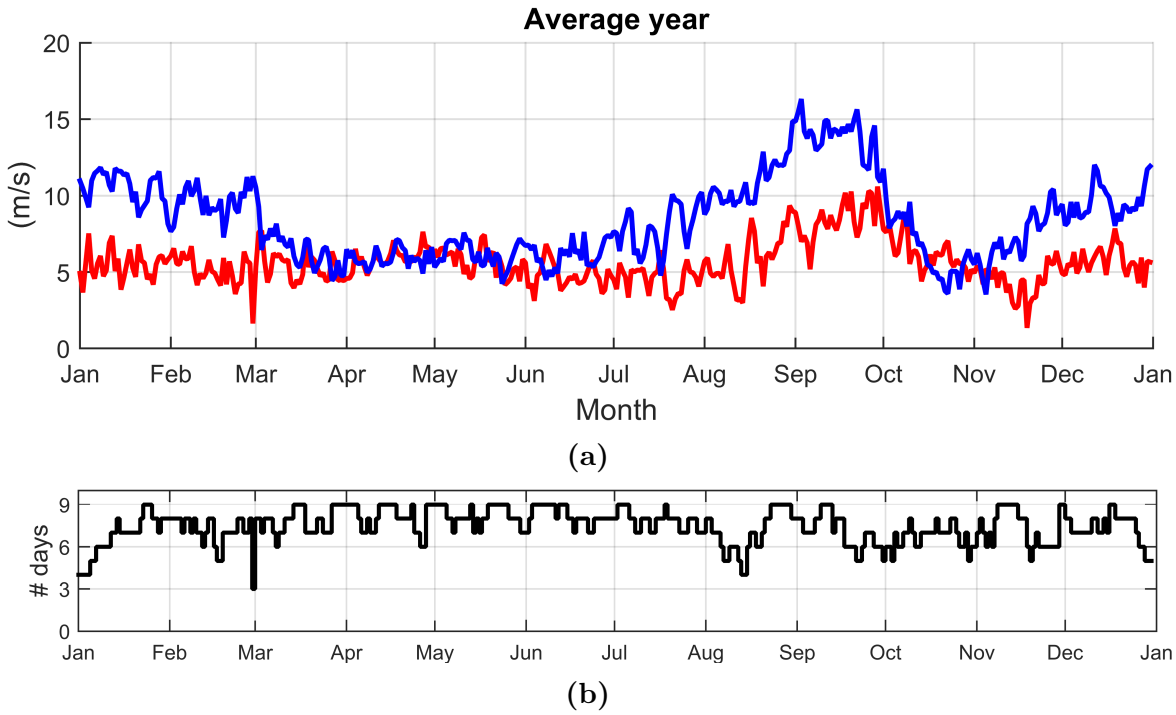

Figure 4.8: Average year from 2000 to 2008 for S1 (red line) and S2 (blue line) **(a)**. **(b)** shows number of data points from the 9 years contributing to each day in the average year.

the first and third repeated year will have end effects, the edges of the second year will blend in with the previous and following repeated year. The climatologies of the S1 and S2 (black lines in second segment in figure 4.9a and 4.9b respectively) shows that the S2 component has large enhancements maximizing around fall equinox starting around the start of June, ending in the start of November. Another enhancement is then noted in the winter months. These enhancements has maximum amplitudes of around 13 m/s and 10 m/s respectively. The S1 shows an enhancement around the fall (from August to start of November), but is more moderate than the S2 with amplitude of around 8 m/s. During the rest of the year the S1 shows quite flat profile at around 4 – 6 m/s. Right after spring equinox until June, the S1 and S2 are both small and approximately equal in strength.

4.4.4 Seasonal anomalies of the S1 and S2 amplitudes

Anomalies are useful when looking at how different phenomena affect the S1 and S2 components without the seasonal behaviour. That way, the seasonal cycle does not contaminate the comparison. E.g. when comparing the tidal response to some phenomena that happens at different times of the year, the seasonal difference may add a lot of variation to the comparison.

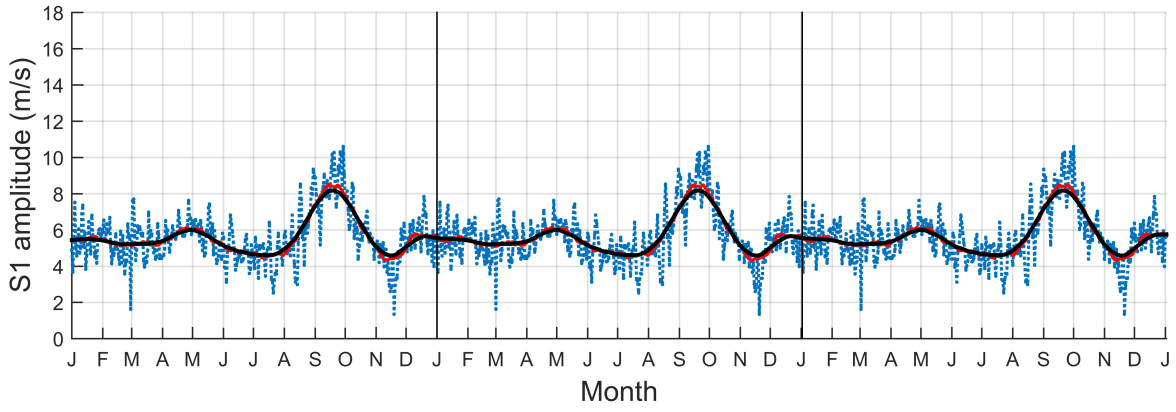

(a)

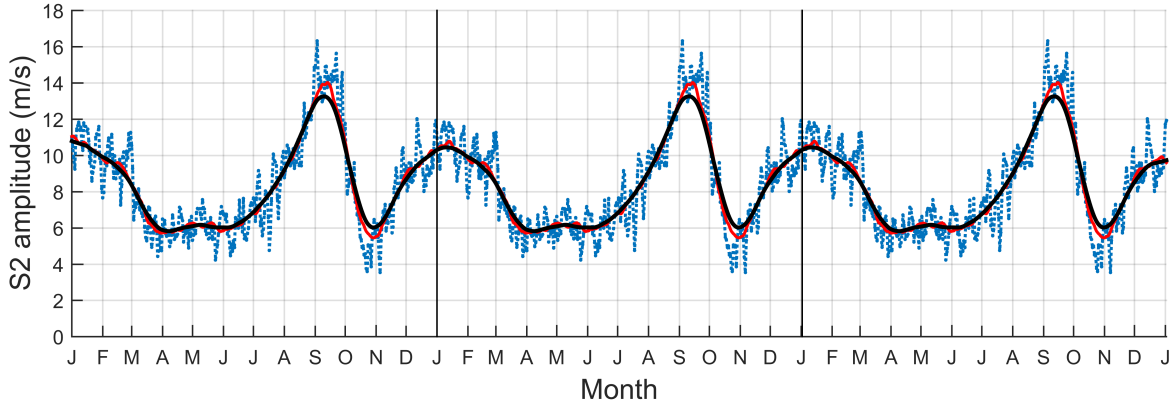

(b)

Figure 4.9: Shows the results of the 31-day running mean smoothing for the S1 and S2 amplitudes from fitting routine. The figure shows the average year (dotted blue line), first smoothing (red solid line) and the second smoothing (and black line). The horizontal axis indicate the month and the vertical black lines shows the start of each repeated year.

Figure 4.10 shows the resulting amplitude anomalies for the S1 and S2 for 2000 and 2008 by subtracting of the climatology from the amplitude data. The results for the rest of the years are given in appendix B. The results shows large (5 – 10 m/s) intra-seasonal fluctuations of 10 – 15 days especially in winter and fall corresponding with large semidiurnal tide amplitudes.

4.5 Connection to atmospheric events

An enhancement of the semidiurnal tide from single stations during SSWs have been observed previously, but the S1 and S2 component might behave differently. This will be investigate in the analysis in section 4.5.1. Then in section 4.5.2, the anomaly amplitudes are used to look at the possibility of the AE to be a generational mechanics for the S1 component of the semidiurnal tide by looking at correlations with the *AE* index.

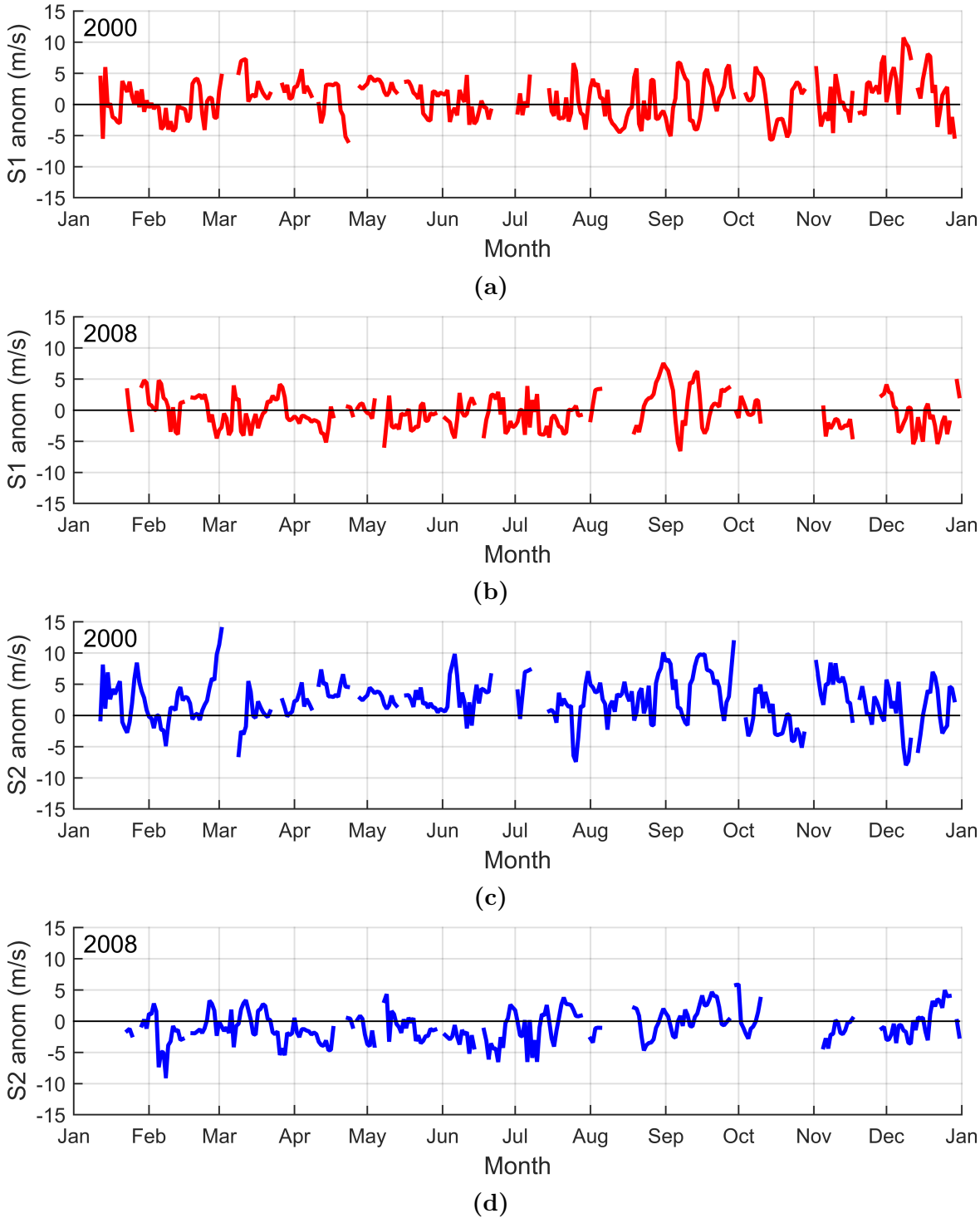

Figure 4.10: Plot of the semidiurnal S1 (**(a)** and **(b)**) and S2 (**(c)** and **(d)**) amplitude anomaly from the year indicated in the top left of each plot.

4.5.1 SSW

Using the criteria explained in section 2.3.1 results in 23 SSW events in the period between 2000 – 2008, of these 7 were also followed by an ES event. The SSW ES events are expected to have the largest effect, as also seen in e.g. Stray et al. (2015).

The SSW dates used are 11 December 2000, 29 January 2001, 22 December 2001, 29 December 2002, 19 December 2003, 9 January 2006 and 23 January 2008. These dates mark the onset of the reversal of the stratospheric polar cap zonal-mean zonal wind at ∼50 km. In the following plots, the onset date is set to day 0.

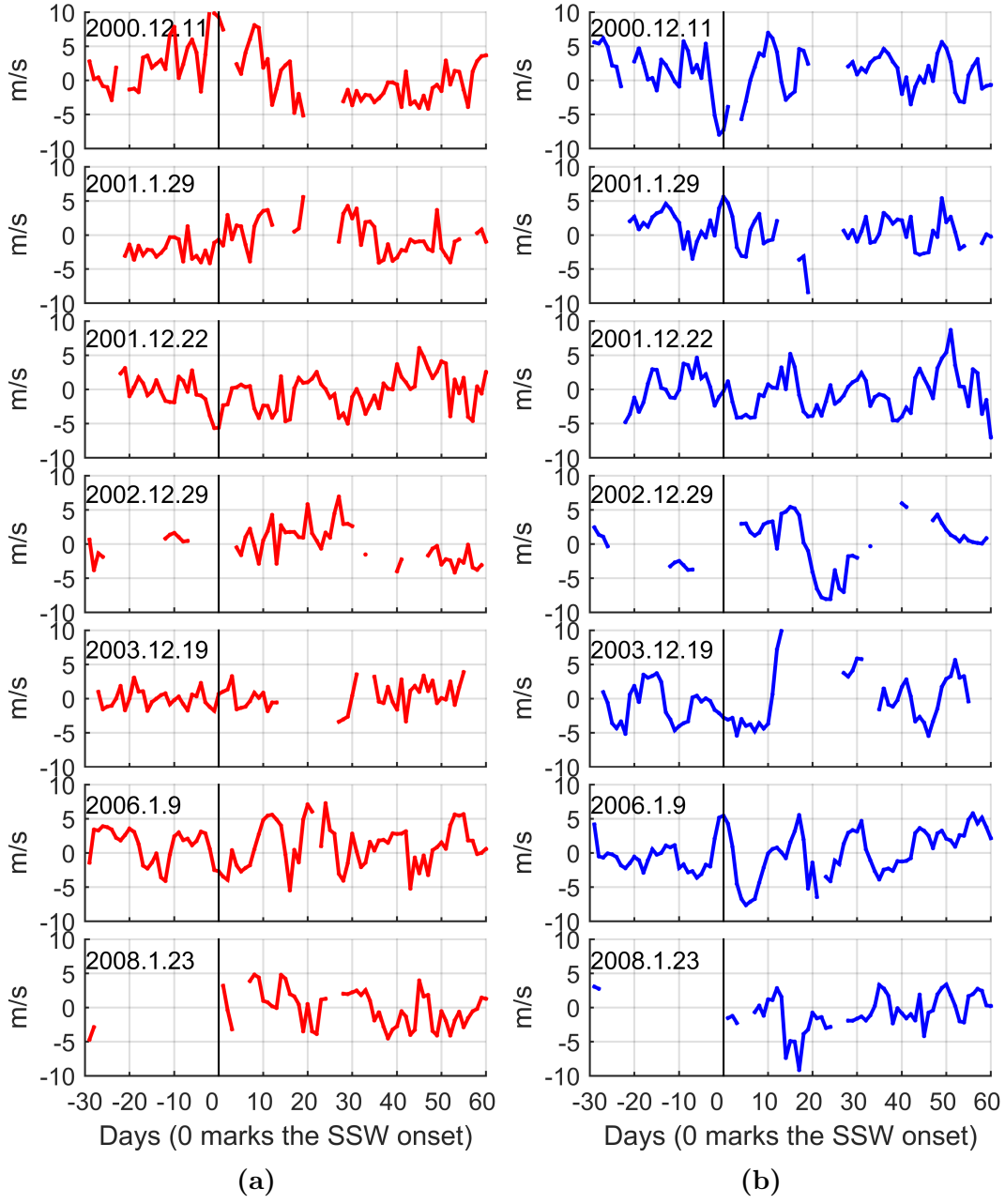

Figure 4.11: Anomaly amplitude of S1 **(a)** and S2 **(b)** from 30 days before, to 60 days after the SSW onset (day 0). The date of the SSW is marked at the top left of each subplot. The black vertical lines marks the onset.

The extracted anomaly amplitudes from 30 days before the onset to 60 days after is shown in figure 4.11 for each individual date. For the S2 the results show a high frequency of maximum at 10 – 15 days after the onset, and a minimum at 0 – 5 days

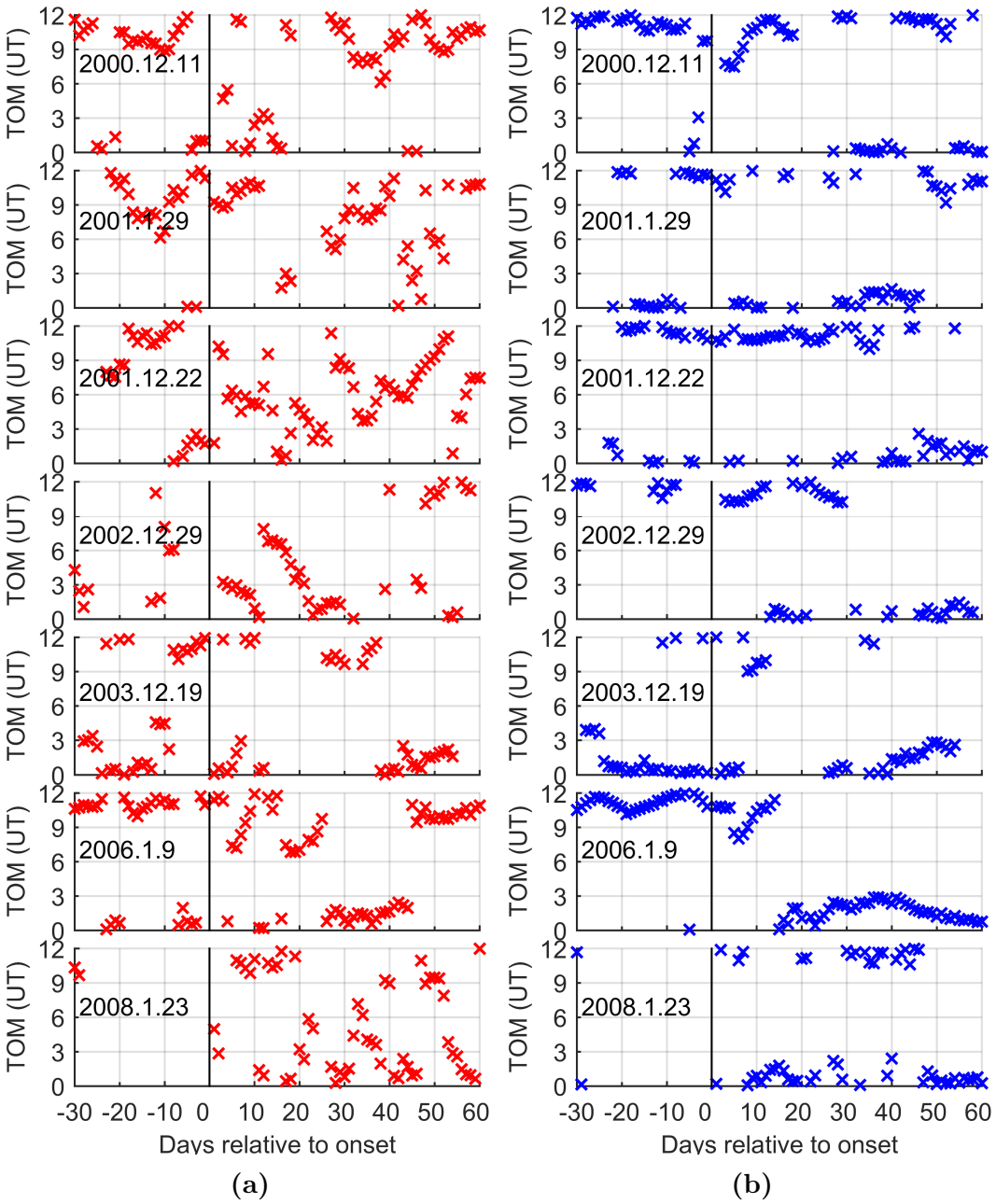

Figure 4.12: Time of maximum of S1 **(a)** and S2 **(b)** from 30 days before, to 60 days after the SSW onset (day 0). The date of the SSW is marked at the top left of each subplot. The black vertical lines marks the onset.

after the onset. The S1 anomaly around the events seems more random making it harder to deduce some significant trends.

Figure 4.12 shows the individual phase data for the same events. Since the fitting routine only produces Φ_{diff}, the two-station method phases are shown here. The phase values of the S2 looks quite stable before the onset at around 0UT for each event, and for some of the events there is a significant decrease of about 4 – 5 hours in TOM (from day 0 to around day 15. This is especially true for 2000.12.11 and 2006.1.9. Similar

tendencies are noted in 2002.12.29 and 2003.12.19. After the rapid decrease, the phase seems to stabilize again. The phase of the S1 is more unstable compared to the S2, which once again makes it harder to determine some common trend.

Some of the dates have quite low coverage during the event, making it harder to draw an objective understanding of how the amplitude changes around the onset. Therefore an arithmetic mean of the amplitudes of each day around the onset for dates containing data is used to yield a super-posed epoch, which will give a combined picture of how the amplitudes change. The super-posed epoch of the amplitude anomaly data and the raw S1 and S2 amplitude data is shown in figure 4.13. The S1 super-posed epoch is shown in figure 4.13a. It shows maximum amplitude around 19 days after the onset, the same can be noted for the anomaly data in figure 4.13b. The epoch of the S2 amplitudes and anomaly in figure 4.13c and 4.13d shows a maximum 12 days after the onset which is an increase of roughly 5 m/s compared to right after the onset. A large peak is also found at day -30 and around day 50 in the S2 epoch. Removing the seasonal variation does not change the characteristics of the epoch for either the S1 or S2 much.

Since this is an epoch consisting of only seven SSW events, the number of events covering each day around the onset is likely to affect produced values quite a bit. Figure 4.13e shows the number of SSW dates that cover each day around the onset. The better coverage, the better one would expect the results to reflect the real response of these wavenumbers to SSWs. Moreover, one would expect changes in the amplitude when the coverage changes that cannot be credited the SSW. The coverage shows that most days (around 60%) are covered by 5 – 6 SSW events. 3 – 4 events cover day -30 to -22, and 19 to 25. Only 3 events cover the S2 minima at day -23 and 21. 7 events covers both the maximum at day 12, and the maximum at day 50. The enhancements obtained in the S1 at day 13 and 19 show quite abrupt changes. At day 13, the S1 increases and the S2 decreases rapidly. This is likely due to the fitting routine setting the amplitudes equal for some of the events. The day 19 enhancement is likely caused by the degrease in the coverage from 6 to four events. The credibility of the two S1 minima are therefore not as high as the more persistent increase in the S2. The S1 does show a small persisting enhancement from day 7-10, and another from day 21-24.

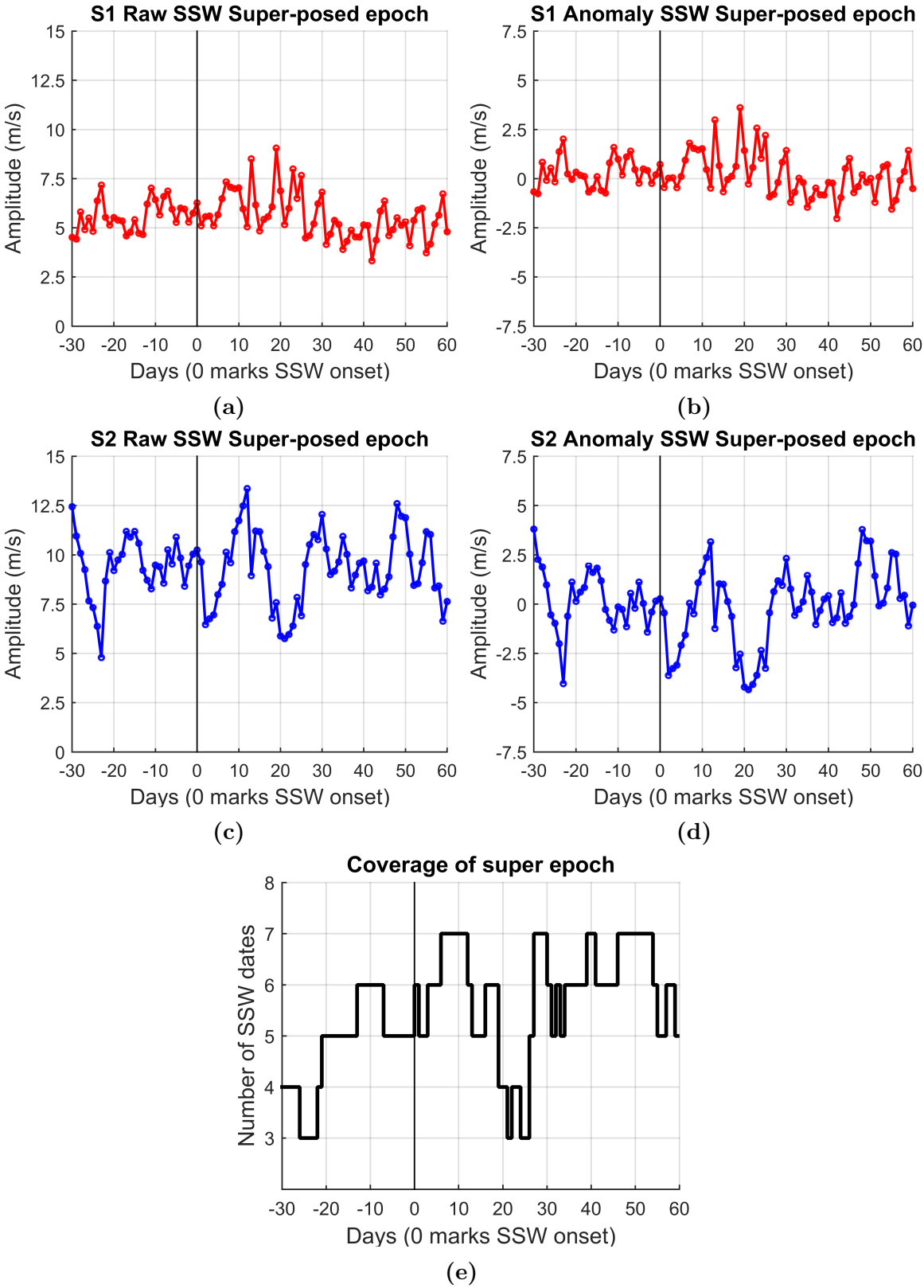

Figure 4.13: Amplitude of S1 **(a)**, S1 anomaly **(b)** S2 amplitude **(c)** and S2 anomaly **(d)** from 30 days before to 60 days after the SSW onset (day 0). **(e)** shows the number of SSW events covering each day.

4.5.2 Auroral electrojet

Figure 4.14 shows the values of the *AE* index for three of the years used in the following analysis, namely 2000, 2004 and 2008. During solar maximum (2000) the *AE* index is in general much larger compared to during solar minimum (2008).

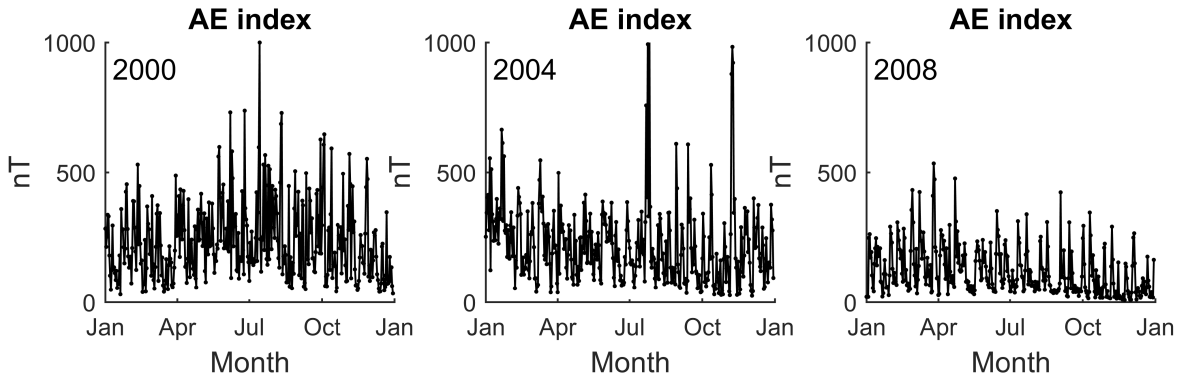

Figure 4.14: *AE* index in nT for the years indicated in the top left of each plot.

The correlations in the following and their 95% confidence intervals were calculated using the *crosscorr* function in Matlab that accounts for missing values. The data vectors were shifted manually in order to perform the lagged correlation. In the results below, a positive lag means that the tides are leading, and a negative lag means that the *AE* index is leading. Figure 4.15 shows the *AE* correlation with S1 (left) and S1 anomaly (right) for all nine years (2000-2008) of amplitude data from the fitting routine. Black solid line shows the correlation coefficient (r) and the blue area show the 95% confidence interval. What small correlations can be noted in figure 4.15 for the raw amplitudes is for the most part lost when removing the seasonal variability of the amplitude data.

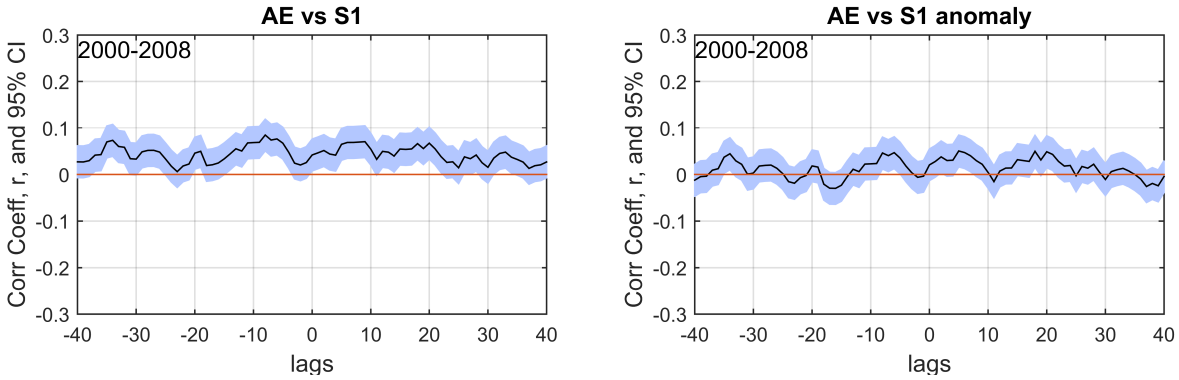

Figure 4.15: *AE* correlation with data from all years combined (2000-2008) for the S1 amplitude data (left) and S1 anomaly data (right). The plots indicate the correlation coefficient (black line) and the 95% confidence interval (blue area) of the coefficients.

Figure 4.16 shows the *AE* correlated with S1 data from 2000. The correlation yields highly varying values. The anomaly data increases r for the peaks around lag -28 and 27, but these peaks are just on the border of being statistically significant.

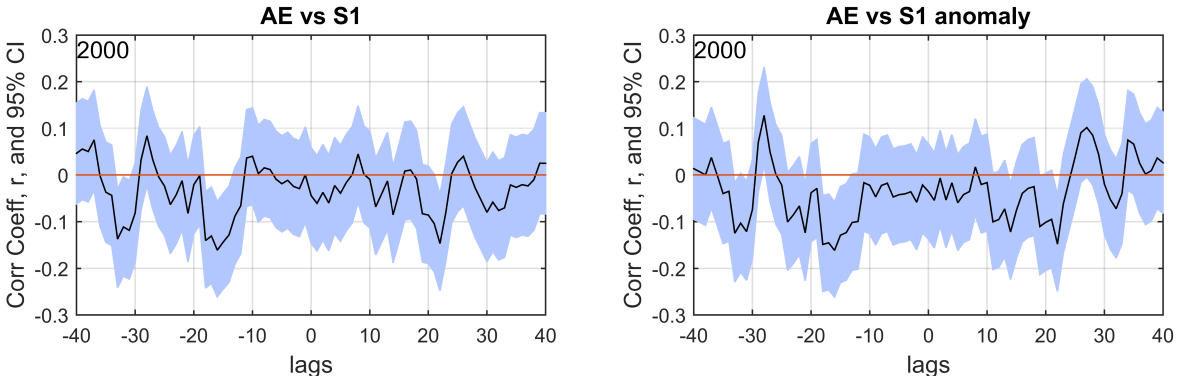

Figure 4.16: Same as figure 4.15 but for only 2000.

Figure 4.17 shows the correlation with the S1 amplitude and S1 anomaly amplitude from 2008. The correlation with the S1 amplitude shows a peak at lag +5 that is statistically significant, as well as a peak at +19 and +32. The r-values are between 0.1 and 0.15. For the anomaly data, the r-values of the peak at 19 is dampened and the r-values of the peaks at -23, +4 and +31 are increased to about 0.2, also they form sharper peaks. Hence, there is a 27-lag spacing between the peaks. The minima at -29, -2 and 26 with coefficients from $0.2 - 0.3$ is also noted, with the same repeating 27 day cycle.

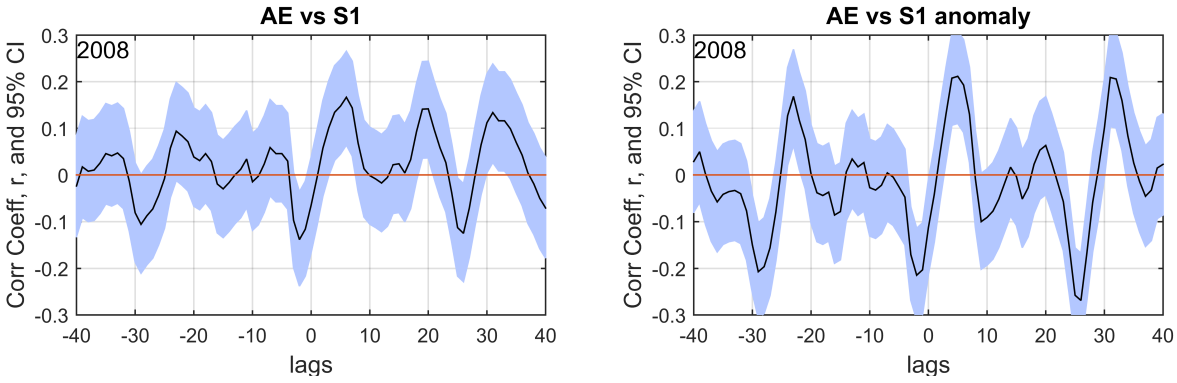

Figure 4.17: Same as for figure 4.15, but for only 2008.

The *AE* correlation with all individual years is given in appendix D. None of the other year produce as prominent features as 2008. However, 2007 shows some of the same tendency when splitting the year into the first and last 6 months. Figure 4.18a

shows the whole year, figure 4.18b and figure 4.18c show the first and last half of 2007 respectively. The correlation with all of 2007 shows few lags that are statistically significant for the anomaly data but shows some wide peaks roughly at lags -32, -10, -5 and 23. The first half of the year shows more prominent peaks at roughly -37 and -11, and the last half shows peaks at lags -30, -3 and 23. It might be noteworthy that the offset of the peaks in both halves of 2007 and 2008 are different with the closes peak to lag 0 being respectively -11, -3 and 5.

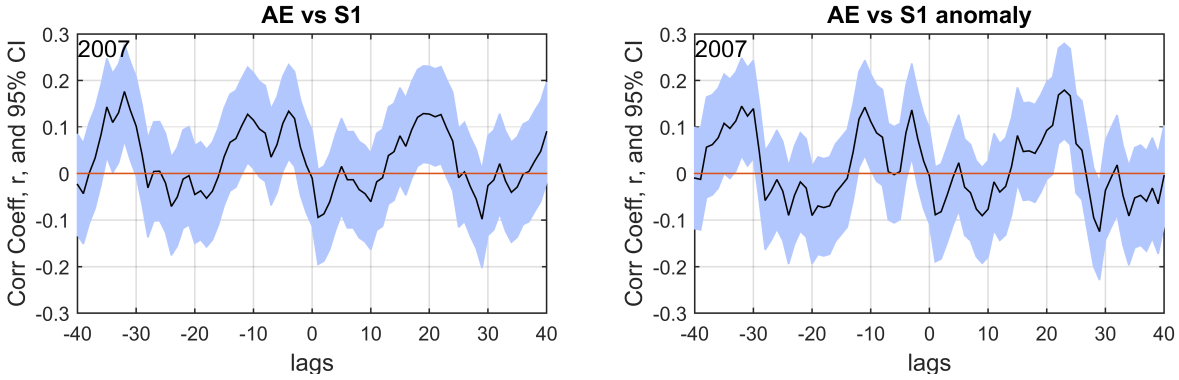

(a) Whole 2007

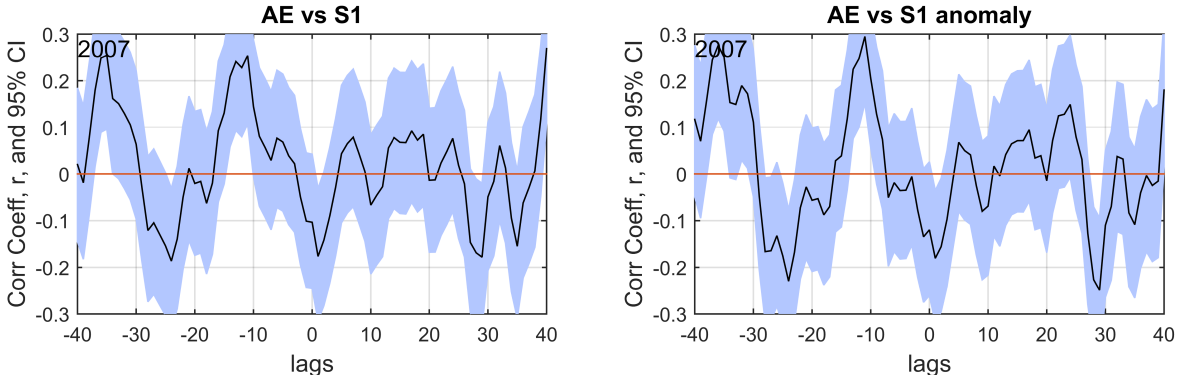

(b) First 6 months of 2007

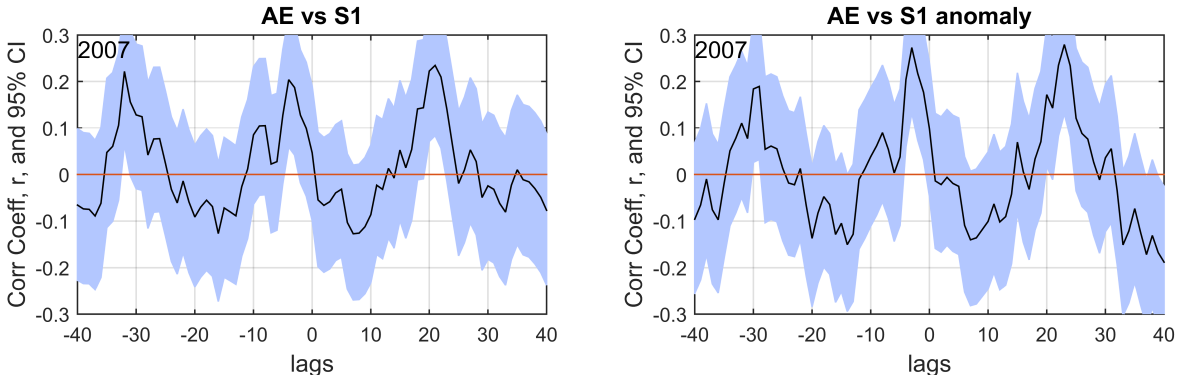

(c) Last 6 months of 2007

Figure 4.18: Same as for figure 4.15, but for the whole 2007 in **(a)**, first 6 months of 2007 in **(b)** and last 6 months of 2007 in **(c)**.

Splitting 2008 in two as done with 2007 yields the results shown in figure 4.19. The last half of 2008 yields stronger r-values compared to the correlations with the full year, and the strongest correlations are produced for the same lags.

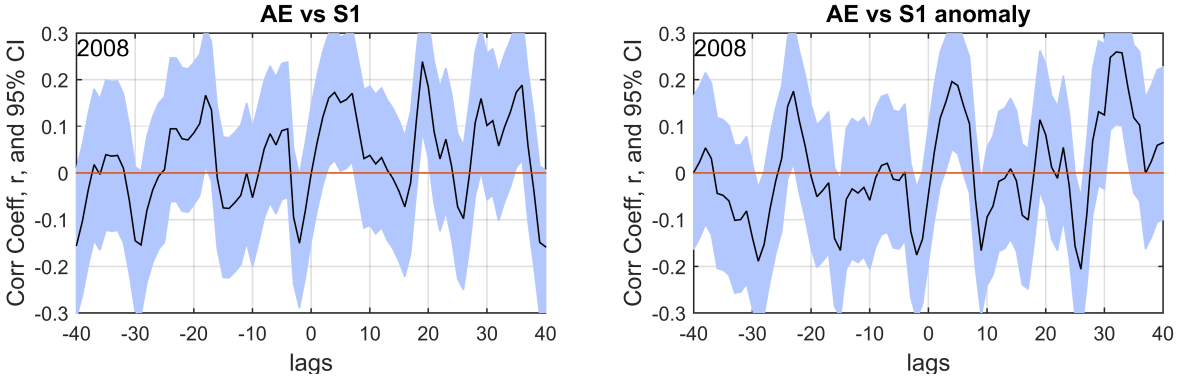

(a) First 6 months of 2008

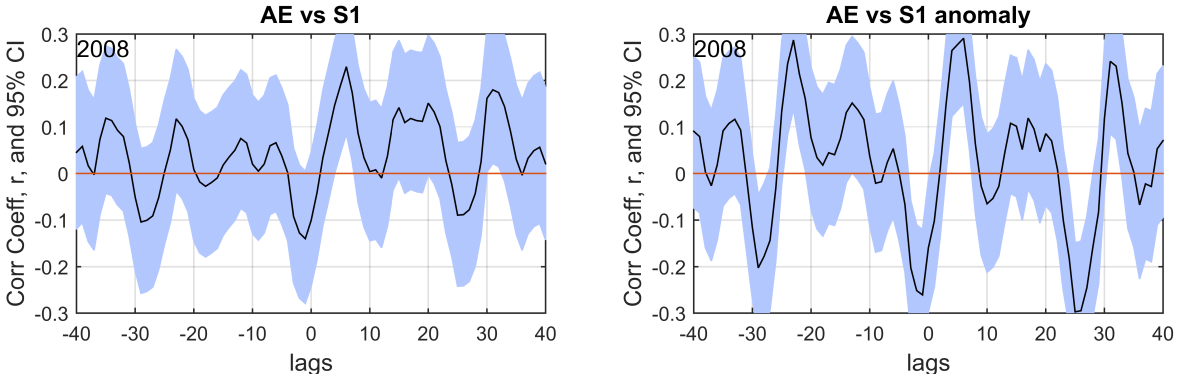

(b) Last 6 months of 2008

Figure 4.19: Same as for 4.15, only for the first 6 months **(a)** and the last 6 months **(b)** of 2008.

Chapter 5

Result validation

This chapter presents an assessment of the non-linear least-squares fit and the validation method (two station method) used to estimate the S1 and S2 component of the meridional semidiurnal tide, presented in chapter 4. In section 3.3.1 synthetic data was used to evaluate the two methods showing good agreement. Although the wings of the amplitude distribution of the fitting routine was wider than the two station method, it performed better for the A_{S1} method and equally for $A_{S2} \sim 95\%$ of the time. The fitting routine produced far better Φ_{diff} resolution, but had a 2π discrepancy due to the cosine term in the fitting function.

In this chapter a correlation between the obtained A_{S1}, A_{S2} and Φ_{diff} results is preformed showing a strong positive linear relationship between the two methods. As expected a 2π discrepancy in Φ_{diff} is found. Then the effects of the tendency in the fitting routine to output $A_{S1} \approx A_{S2}$ is investigated and shows that even though this is happening, it seems to only affect amplitude with differences within the uncertainty of the measurements.

5.1 Methods correlation

Correlation between the two methods gives correlation coefficient of 0.46 for the A_{S1} amplitude, 0.85 for the A_{S2} amplitude and 0.87 for Φ_{diff}. This shows a strong positive linear relationship between the two methods. Figure 5.1 shows the values of the two station method along the x-axis and the multiple station fitting routine along the y-axis for A_{S1} (left), A_{S2} (middle) and Φ_{diff} (right). The linear regression values for both $y = Ax$ and $y = Ax + b$ regression functions are given in table 5.1.

The S1 regression shows that the fitting routine has a tendency to produce larger amplitude values compared to the two station method. The S2 regression shows that the values compare better than for the S1 as suggested using the synthetic data. The regression of Φ_{diff} shows, albeit it having the highest correlation coefficient, that there are deviations from the two methods. This also shows that some of phase difference

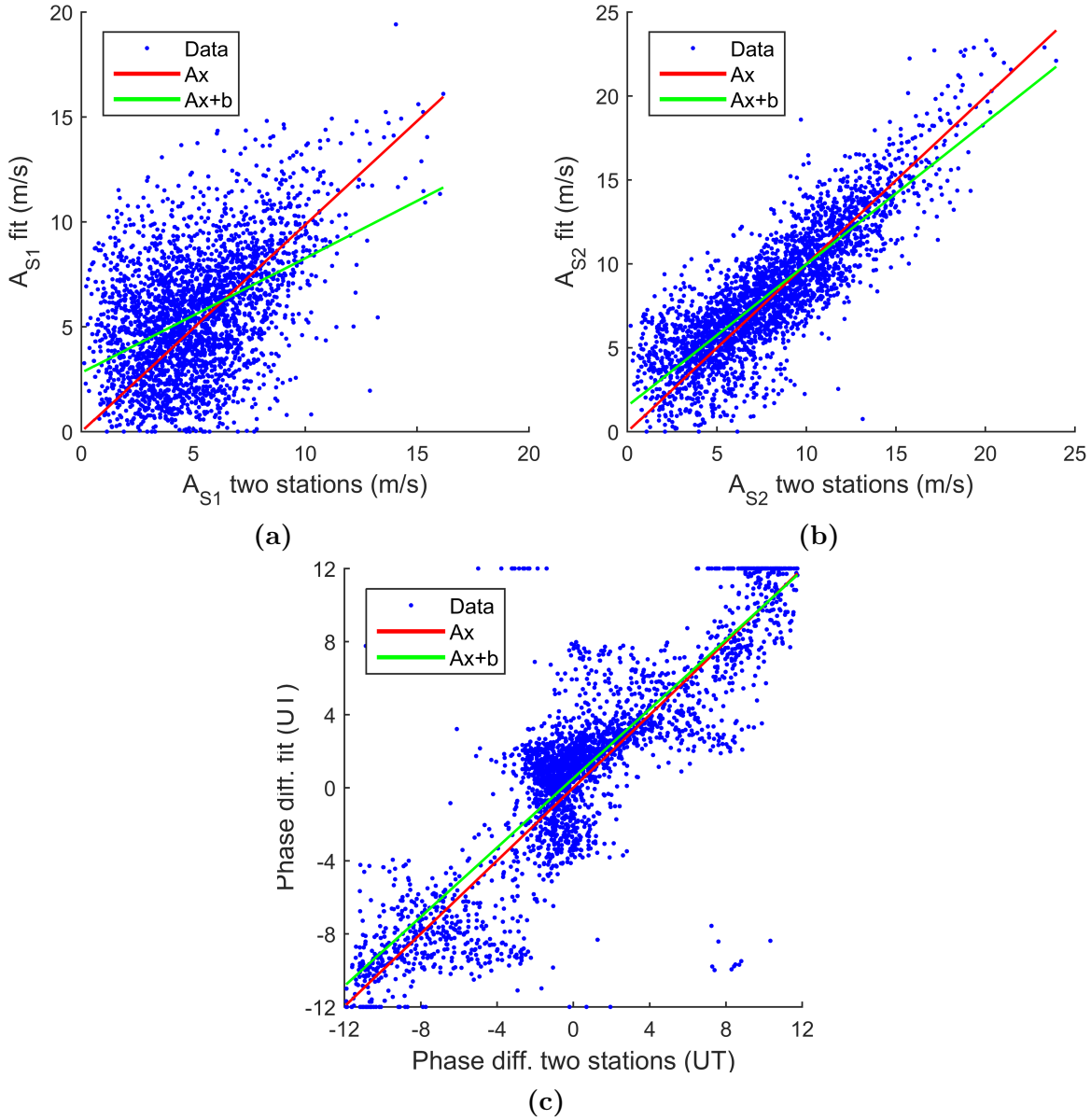

Figure 5.1: Correlation plot between the amplitude in m/s from the fitting routine in x-direction, and amplitude from the two-station method in y-direction for the semidiurnal S1 (left), S2 (middle) Φ_{diff} (right) as blue dots. The red and green line is the linear regression on the form $y = Ax$ and $y = Ax + b$ respectively.

Table 5.1: Values of the linear regression between the amplitude and phase data gathered by the two station method and multiple station fitting routine shown in figure 5.1.

Data	Regression function	
	Slope·x	Slope·x + Intersect
A_{S1}	$0.987x$	$0.546x + 2.812$
A_{S2}	$0.998x$	$0.844x + 1.528$
Φ_{diff}	$0.955x$	$0.948x + 0.518$

values from the fitting routine has the value ±12 UT. Since the phase cycle is 12 hours, this is the same as 0 UT. This will affect the regression values of Φ_{diff}.

5.2 Investigation of $A_{S1} \approx A_{S2}$

Figure 5.2 shows a histogram of $A_{S2} - A_{S1}$ for both methods. It is apparent that $A_{S2} \approx A_{S1}$ is a lot more frequent for the fitting routine compared to the two-station method. However, outside of the interval [-3.5, 6.5] m/s, the distributions are quite similar.

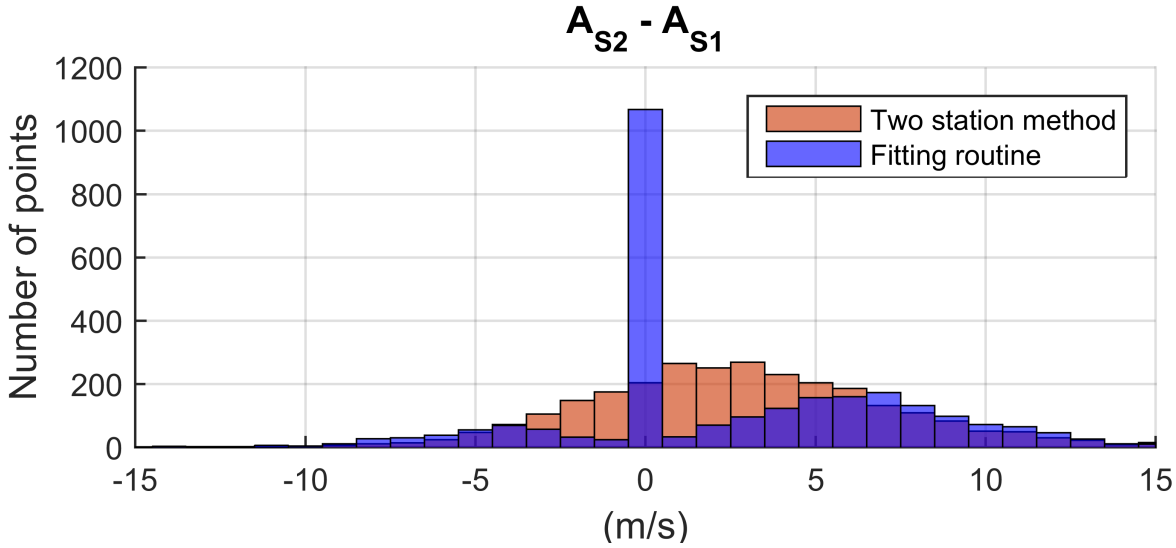

Figure 5.2: Histogram of $A_{S2} - A_{S2}$ from the two-station method (orange) and the fitting routine (blue) for 2000 – 2008 combined. Every bin is 1 m/s wide and is centred around each integer.

Excluding the zero points and subtracting the fitting values in the histogram off of the two-station values yield the residual histogram in figure 5.3. It looks like an approximate normal distribution around 1 m/s with σ around 2 – 3 m/s (containing $\sim 68\%$ of the data points).

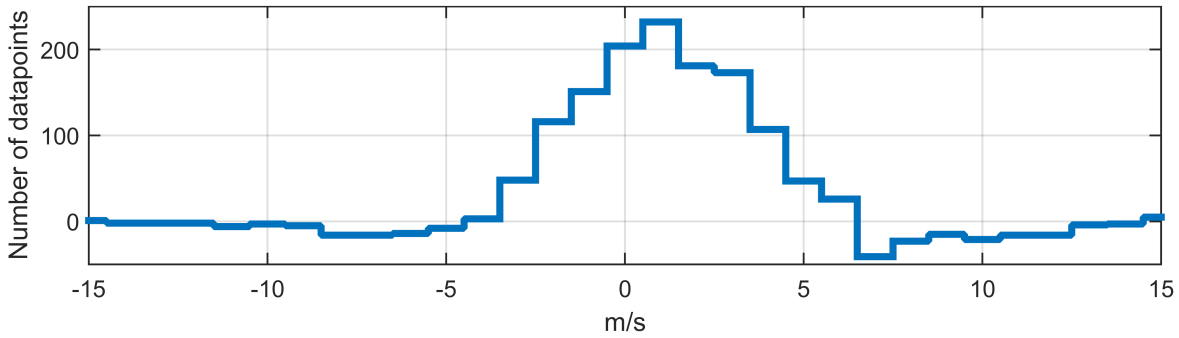

Figure 5.3: The residual when removing all zero points from histogram in figure 5.2 from fitting routine and subtracting the histogram values of the two-station data off of the fitting data.

The uncertainty in the data using the two-station method is as estimated in section 4.3 around $2 - 3\,\mathrm{m/s}$. Hence, if A_{S1} and A_{S2} are closer together in value than this, one cannot say that A_{S1} is significantly different from A_{S2}. It looks like that when the two distributions of A_{S1} and A_{S2} overlap, the fitting function results in $A_{S1} \approx A_{S2}$. This suggests that there is no discrepancy in the two methods, even though the histogram makes it look like it is. The difference is how the data is portrayed when the S1 and S2 amplitudes are too similar to statistically separate them. This can however yield abrupt spikes in the amplitudes when they become comparable in size.

Chapter 6

Discussion

This chapter discusses the results found in chapter 4 in light of similar studies and the theory presented in chapter 2, starting with the meridional amplitude and phase of the S1 and S2 components (section 6.1). This is followed by a discussion of the results of the super-posed epoch for the SSWs (section 6.2), and ending with a discussion on the results from the AE index correlations with the S1 amplitude (section 6.3).

6.1 S1 and S2 amplitudes

As stated earlier, only S1 and S2 of the semidiurnal tide is assumed significant. This has also been assumed in e.g. Baumgaertner et al. (2006) and Hibbins et al. (2010) in the SH, and Wu et al. (2011) in the NH. Hibbins et al. (2010) compared their results to results gathered by Murphy et al. (2006) where both S0, S1, S2 and S3 was included. From this, it was concluded that excluding the S0 and S3 components should not affect the results in a major way, since they were showed to be much weaker. Both these studies was done in the SH but since the tides are global waves they are expected to behave similar in the NH.

The climatology of the semidiurnal tide in the NH MLT has been well established (e.g. Schminder et al. (1989); Manson et al. (1989); Lysenko et al. (1994); Jacobi et al. (1999); Mitchell et al. (2002)) with maximum winds in fall, when the zonal circulation reverses in the stratosphere and mesosphere, and in winter. The climatology in section 4.4.3 shows S2 enhancements maximize around the fall equinox and winter months with amplitudes of about 13 and 11 m/s respectively, and the S1 is enhanced during fall equinox to about 8 m/s and stays quite flat during the rest of the year. Hence, the enhancement seen in the semidiurnal tides are mainly due to the S2 component. From April to June, the S1 and S2 amplitudes are approximately equal in magnitude (around 6 m/s), meaning that about 50% of the semidiurnal tide is S1 in this period. Using data from the TIDI instrument on the TIMED satellite Wu et al. (2011) found the same S2 enhancements in the NH with an enhancement in the winter months and another enhancement in late summer/early fall at 95 km. For the S1 at $\sim 60°$N a

maximum during fall was found for some years.

Since the tides are global waves, they are expected to be similar across the globe. Therefore, hemispherical deviations are likely due to some interaction in one hemisphere that is not present or as dominating in the other. Baumgaertner et al. (2006) studied both the zonal and meridional semidiurnal S1 and S2 component over Antarctica and found large amplitudes during November to February (SH summer months) which were often dominated by the S1 component. A mixture of both S1 and S2 was found to contribute from April to September with smaller amplitudes. Murphy et al. (2006) found that the S1 component was dominating from October to around March, but the S2 showed comparable amplitudes during January, and dominated from April to September. Similar results were also found in Hibbins et al. (2010). Hence, the winter months are found to be mostly dominated by the S2 component in both NH and SH. The amplitudes in the summer months are however found to deviate a lot in the different hemispheres. The S2 component is comparable to the S1 in the NH during early NH summer and dominates during late summer and fall, whereas the S1 in the SH often dominates during SH summer. Hence, during the respective hemispherical summer, there seems to be more non-migrating generation mechanics in the SH contributing to the S1 component compared to in the NH.

As mentioned, one of the generation mechanics of the non-migrating components of the semidiurnal tide are non-linear interaction with the migrating tide and a wavenumber 1 stationary PW (SPW1) (Forbes, 2009). Iimura et al. (2014) found large interannual variation of the S1 and SPW1 in both NH and SH, and found evidence of inter-hemispherical connections between the SPW1 and the non-migrating tides in the opposite hemisphere. The PW activity is higher in the NH than in the SH, due to the many land-sea boundaries one encounters along a line of latitude in the NH, as compared to the more symmetric SH. Thus, the SH winter PW activity is much lower. This could account for the lower S1 activity in the NH summer. This idea is consistent with the hypothesis put forward in Murphy et al. (2006).

There was a rare SH SSW event in September of 2002. Hence, inter-hemispherical generational mechanics of the S1 component through non-linear interactions with the S2 and SPW1 might show up as an enhancement in the S1 component during this SSW. No unusual enhancement of the S1 amplitudes is found in our results during this period. However, Wu et al. (2011) found a small increase in S1 component in the NH during this event. The enhancement in the S1 was found to be located poleward of

roughly 70°. Since our data is gather from stations from ∼50-65°N this could explain why no similar increase is found in our results.

These results suggests that the strong wintertime NH PWs, creating SSWs, are likely the source for the much stronger summer S1 winds in the Sh compared to the NH.

The S1 and S2 are close to in phase ($\Phi_{diff} = 0$) during summer and winter, and is more frequently out of phase close to equinoxes where the amplitudes of in particularly the S2 is changing rapidly. That the waves are in phase suggests similar and stable vertical wavelengths of the S1 and S2 during many months of the year. These results fits well with results from the Antarctica region where phases are recorded to be more variable when amplitudes are small. This can also be a result of the reduced phase accuracy when the amplitudes are small (Hibbins et al., 2010).

6.2 SSW discussion

Figure 6.1 shows wind data of the zonal (top) and meridional (bottom) component of the semidiurnal tide, using a meteor radar located in Trondheim (∼ 64°N), from December 2012 to March 2013. The total semidiurnal tidal amplitudes is observed to enhance shortly after a stratospheric warming event (onset around January 6 2013). Our analysis in section 4.5.1 of the 7 SSW events, identified by Stray et al. (2015), shows that this tidal enhancement occurs primarily in the S2 component.

For confirmation, R. Hibbins (personal communication, 2016) examined the same 7 events using the full hourly fitting to the radars (explained in detail in Hibbins et al. (2010)). These results are shown in figure 6.2a along with a reorganized plot of the results obtain in the present study in figure 6.2b. The S2 amplitude shows the same characteristics as our results, with an enhancement of about 5 m/s maximizing around 12 days after the onset. The main difference in the two results is the S2 peak at day -30 and the larger S1 amplitudes peaks from day 12 to 25 found in our results. These peaks are unlikely to reflect an actual S1 enhancement during SSWs since the peaks only persists for one single day (one data point), and that the deviations mentioned here coincides with days with few data points as seen in figure 4.13e. These points may be cause by the $A_{S1} \approx A_{S2}$ tendency of the fitting routine detailed in chapter 5, as the S2 epoch shows corresponding rapid changes for some of these points. In addition, the hourly fitting routine, which generally yields better data coverage, does not show these peaks. If ignoring the maxima at day 13 and 19, the S1 looks more comparable to the

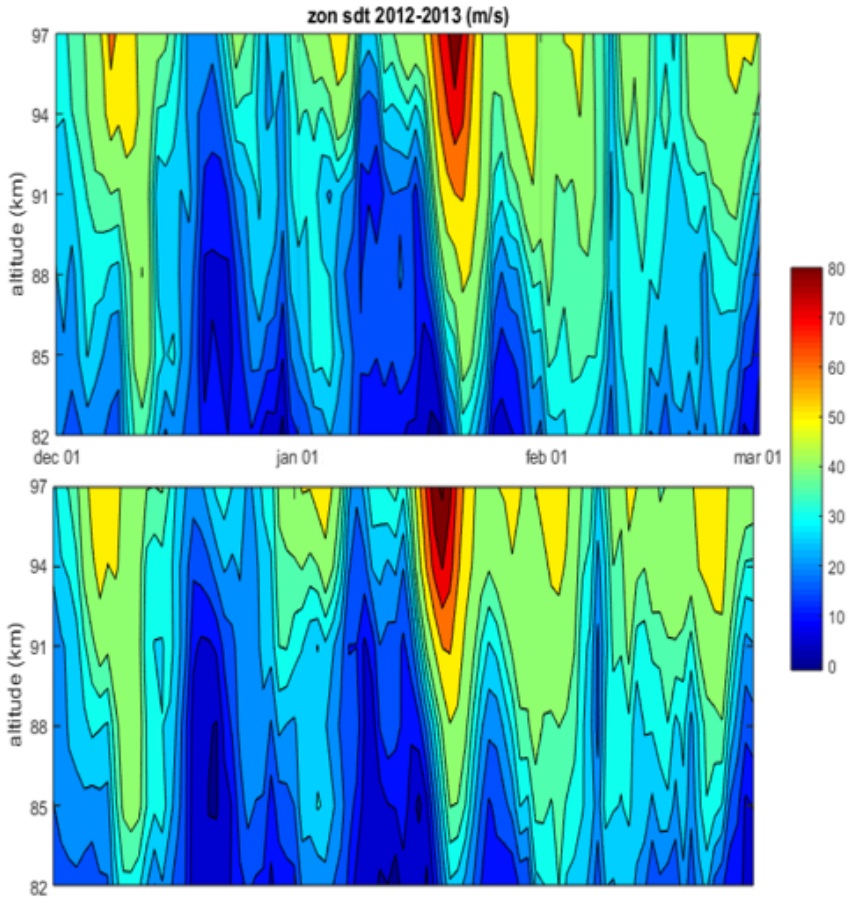

Figure 6.1: Semidiurnal tide data from meteor radar at Trondheim at 64°N in 2013 for the zonal (top) and meridional (bottom) component from December 2012 to March 2013 during a SSW event with the onset around January 6. From P. Espy and R. Hibbins (personal communication, 2016).

S1 obtained using the hourly data, showing a small enhancement around day 10 and 20 after the onset.

Pedatella and Liu (2013) used numerical simulations of SSW under different atmospheric tide and PW conditions, to investigate the variability of, among others, the S1 and S2 component of the semidiurnal tide in the MLT. They found that SSWs lead to an enhancement in the S2, and due to change in the vertical wavelength of the S2, saw phase variability at constant altitude. In addition, the S1 was found to only show significant enhancements when in the presence of additional PW activity. As seen from Stray et al. (2015), the PW were present and increasing for all SSW events reaching a maximum about 10 days after the event. These simulations also shows significant longitude variability that occurs in the ionosphere in response to SSWs.

Using the WACCM simulation of 23 SSWs Pedatella et al. (2012) found global changes

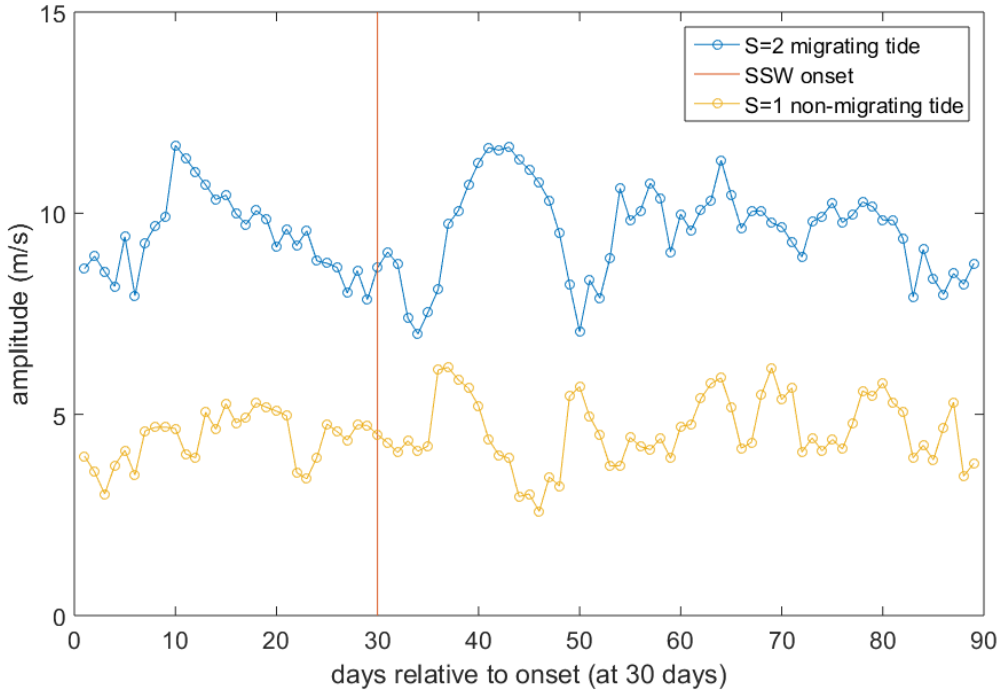

(a) From R. Hibbins (personal communication, 2016)

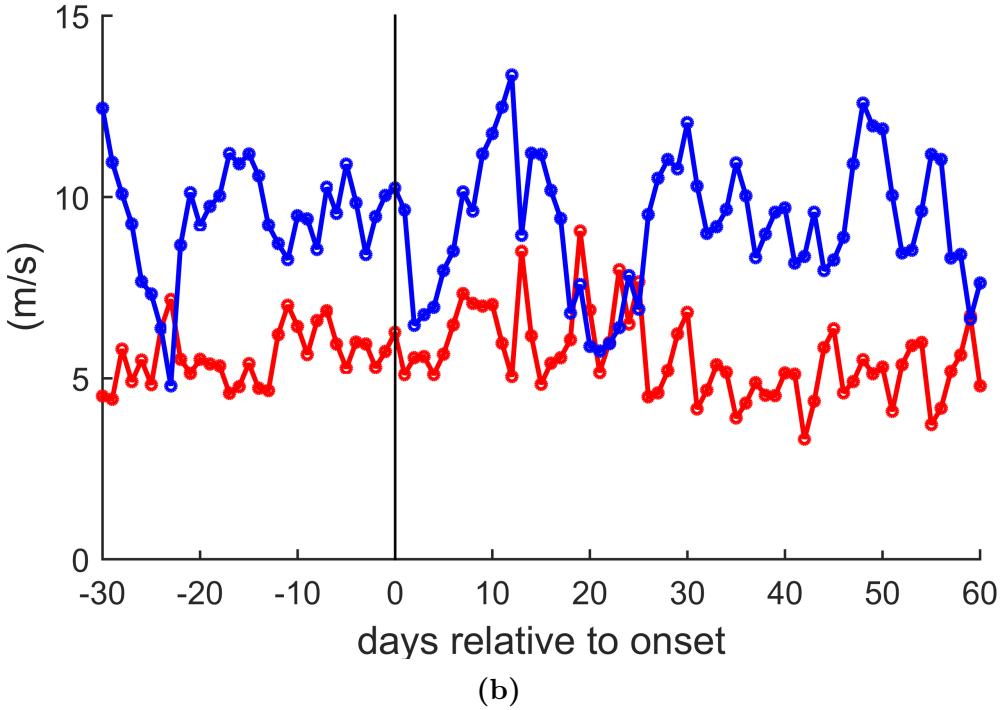

(b)

Figure 6.2: **(a)** shows super-posed epoch results obtained by R. Hibbins (personal contact, 2016) using a full hourly fitting routine on the data from the SuperDARN radars for the same 7 events as in this thesis. **(b)** shows reorganized data results from figure 4.13 for S2 amplitude (blue) and S1 amplitudes (red). Day 30 in **(a)** corresponds with day 0 in **(b)**.

occurring in both the semidiurnal S1 and S2, showing the greatest changes in the S2 with $\sim 5 - 6$ m/s, comparable to our findings. In the same study changes in the tidal phases were also found, but less than $\sim 1 - 2$ h, and was considered to only to be of minor importance. Our results shows relatively stable S2 phase values prior to the onset, a rapid decrease by $\sim 4 - 5$ h right after the onset for some of the SSWs, followed by a stabilization process of varying length. The particular SSW events showing S2 phase changes also show the largest changes in the S2 amplitudes. The S1 phase does not show the same phase stability prior to the onset and thus making it harder to conclude on the significance of these changes.

Our studies indicate that SSW causes changes, especially in the S2 components. However, the results are not consistent for every event. This was also noticed in Wu et al. (2011), and might be linked to how the polar vortex breaks down during a SSW as detailed in section 2.3.1. The two types are vortex displacement, and vortex splitting often associated with a zonal wavenumber 1 and 2 respectively (Charlton and Polvani, 2007). The specific SSW type was not identified for the SSW events used in this study; hence, both types of SSWs are mixed in the super-posed epoch. If the different types manifest themselves differently in S1 and S2, they will blend. One would expect this to dampen the combined effects seen in the epoch compared to an epoch consisting only of the S1 and S2 amplitude data for dates corresponding respective SSW type.

Even though a number of numerical and observational evidence demonstrate that SSWs connect to ionospheric disturbances, the mechanics are not yet fully understood (Pedatella and Liu, 2013). Any changes in the either the amplitude or the phase of the semidiurnal S2 component has the potential to cause significant changes in the ionospheric currents and electric fields Fesen et al. (2000). Hence, the indications that the changes during SSWs are mostly S2 driven, and the observation of S2 phase changes, means that most of the tidal enhancement would be capable of propagating into the ionosphere and initiating the process by which the SSW signature is carried to the equator as suggested by Chau et al. (2012).

6.3 AE discussion

Riggin et al. (1999) and Baumgaertner et al. (2006) suggests that zonally asymmetric heating due to particle precipitation can be an additional generation mechanism for the S1 component of the 12 h tide. Since the auroral oval is centred around the geomagnetic North Pole, and the tides are approximately centred around the geographical North

Pole, heating in the auroral oval could be a cause for approximately a S1 temperature structure.

The motivation for looking at the de-seasonalized S1 amplitude data in the correlation is due to the Russel-McPherron effect which can yield seasonal effects in the AE index. This would show up as a correlation between the seasonal effects in the tidal amplitudes which could dominate the correlation results (Russell et al., 1973). As seen in the results the correlation can change a lot when de-seasonalizing the amplitudes.

AE correlated with the S1 amplitude shows a clear 27-day periodicity in 2008 which was a solar minimum year. As stated in section 2.3.2 due to coronal holes and the mean 27-day rotational period of the Sun, a 27-day periodicity is expected in the AE index. This solar-terrestrial connection has been shown in e.g. (Lei et al., 2008) and (Thayer et al., 2008). This can also be seen in the raw AE data presented. If there is a lot of disturbances in the solar magnetic field, which is the case around solar maximum, the high-speed plasma ejections connected to coronal holes might not persist long enough to cause a 27-day periodicity. A 27 day periodicity in the AE correlation with the S1 amplitude would suggest a connection between the S1 and the auroral electro jet.

The results in section 4.5.2 show a weak ($\sim 0.2 - 0.3$) correlation between the AE index and the de-seasonalized S1 amplitude around the solar minimum in 2008, statistically significant above the 95% confidence level. A correlation coefficient of 0.25 would mean that about 6% (0.25^2) of the changes the in the S1 amplitudes can be explained with the changes in the AE index. There is a clear 27-day periodicity between maxima, approximately how the correlation of two signals with a 27-day periodicity (with a phase difference between the two signals) is expected to look. 2000, being a solar maximum year and showing only very small correlations, changes little when removing the seasonal variability, and showing no apparent 27-day periodicity. This fits with the explanation above. One might expect a gradual transition from solar maximum to solar minimum instead of the rapid change in the correlation from 2007 to 2008. However, the correlation with the first 6 months and the last 6 months of 2007 separately indicate a more gradual transition. All of this adds credibility to there being a solar link to the generation mechanics of the S1 component, and that it is particle rather than radiatively driven.

The SuperDARN radars measure the meteor echoes with respect to the background radiation. High auroral activity will increase the background radiation making it harder

to detect meteor echoes and can cause data shortage for days with high auroral activity. This might affect the results shown. In addition, as mentioned in section 2.3.2, during intense solar geomagnetic storms the auroral oval can expand southwards, away from the measuring stations. This can cause large geomagnetic storms, to not be recorded and included in the AE index.

If the auroral oval expands southwards it would cross 60°N in two places, increasing in longitudinal separation with the southward expansion of the auroral oval. At some point, it could potentially generate a wave more closely approximated an S2 wave. The correlation of the AE with the S2 data (given in appendix D) did not show any clear correlation for any year. Further investigation of this is outside the scope of this thesis.

The offset in lag is an indication of the phase difference of the two signals, i.e. how long it takes for a cause in AE to yield a response in the S1 amplitude. The AE is expected to be leading. The observed change in the peaks in the AE correlation, increasing by 8 lags between first half of 2007, last half of 2007 and 2008. This might indicate that there is a change in the time it takes the geomagnetic storms to cause effect in the S1 amplitude. Since the mechanics and circumstances for the S1 generation is not fully understood yet, reading too far into this is not wise, and will not be attempted.

Chapter 7

Conclusion

In this thesis the behaviour of the zonal wavenumber 1 (S1) and 2 (S2) components of the meridional semidiurnal tide has been investigated. These components cannot be determined from single station measurements, but needs spatially separated measurements. To extract the S1 and S2, 9 years (2000 – 2008) of meridional semidiurnal wind amplitudes, extracted from wind data gathered by meteor echoes in the mesosphere and lower thermosphere by a longitudinal chain of Super Dual Auroral Radar Network (SuperDARN) radars, has been used. Assuming that the semidiurnal tide consists of only S1 and S2, as done in previous studies, a non-linear least-squares fit has been performed to extract these two components. In order to validate the aforementioned fitting method, a method published by Baumgaertner et al. (2006) has been used for comparison and also as starting values in the fitting routine. The validation method showed strong positive correlations with the fitting results, and by the use of synthetic data the fitting was shown to produce better results for about 95% of the cases.

The focus in this thesis has been to determine the climatology of the two components, investigate the behaviour of these components during sudden stratospheric warmings (SSW), and look for evidence for asymmetric joule heating by the auroral electrojet as a generation mechanics for creating S1 waves.

The climatology showed that the S2 dominates from June to November maximising around fall equinox, followed by another enhancement in winter. The S1 showed an enhancement around the fall equinox. The rest of the year, the S1 and S2 amplitudes were comparable in magnitude. This behaviours were different from those recorded in the southern hemisphere, where the S1 often dominated, especially in the summer. This was thought to in large be explained by inter-hemispherical coupling between planetary waves and the semidiurnal S2 component.

The behaviour of the S1 and S2 components during SSWs have been studied using a super-posed epoch of 7 SSWs accompanied by an elevated stratopause event. The SSW was found to be mainly S2 driven with the amplitude maximizing roughly 12 days

after the onset of the SSW. For some of the events the phase of the S2 changed quickly right after the onset, before stabilizing again after the event. These results means that most of the tidal enhancement during an SSW would be capable of propagating into the ionosphere and initiating the process by which the SSW signature is carried to the equator, as suggested by Chau et al. (2012).

The auroral electrojet being a generation mechanic of the S1 component has investigate by correlating the S1 anomaly amplitudes and the *AE* index. This yielded weak correlations ($\sim 0.2 - 0.3$) above the 95% confidence level, showing a clear repeating 27 day cycle close to solar minimum. This repeating pattern is thought to be linked to persisting high-speed solar winds from coronal holes, adding credibility to there being a solar link to the generation mechanics of the S1 component, and that it is particle rather than radiatively driven.

Future work

This thesis shows that it is possible to obtain good results using the longitudinal chain of the SuperDARN radars to extract the S1 and S2 of the semidiurnal tide using a non-linear least-squares fit. There should be no problem extending these methods to account for different tidal components and include more wavenumbers. The equations presented by Baumgaertner et al. (2006) can also be expanded to include several longitudinally spread stations.

The planetary wave amplitudes in Stray (2015) and the tidal amplitudes presented in this study gives a good opportunity to study coupling between the tidal and PW energy in the mesosphere and lower thermosphere. E.g. both studies shows an enhancement during fall equinox that might be linked to the generation of the S1 during this period.

Bibliography

Andrews, D. G. (2010). *An introduction to atmopsheric physics*. Cambridge University Press.

Andrews, D. G., Holton, J. R., and Leovy, C. B. (1987). *Middle atmosphere dynamics*. Number 40. Academic press.

Baumgaertner, A. J., Jarvis, M. J., McDonald, A. J., and Fraser, G. J. (2006). Observations of the wavenumber 1 and 2 components of the semi-diurnal tide over Antartica. *Journal of Atmopsheric and Solar-Terrestrial Phyysics*, 68:1195–1214.

Boeker, E. and van Grondelle, R. (2001). Environmental Science. *Physical principles and applications, England: John Wiley & Sons Ltd*.

Chandran, A., Collins, R., Garcia, R., Marsh, D., Harvey, V., Yue, J., and Torre, L. (2013). A climatology of elevated stratopause events in the whole atmosphere community climate model. *Journal of Geophysical Research: Atmospheres*, 118(3):1234–1246.

Charlton, A. J. and Polvani, L. M. (2007). A new look at stratospheric sudden warmings. Part I: Climatology and modeling benchmarks. *Journal of Climate*, 20(3):449–469.

Chau, J. L., Goncharenko, L. P., Fejer, B. G., and Liu, H.-L. (2012). Equatorial and low latitude ionospheric effects during sudden stratospheric warming events. *Space Science Reviews*, 168(1-4):385–417.

Chisham, G., Lester, M., Milan, S. E., Freeman, M., Bristow, W., Grocott, A., McWilliams, K., Ruohoniemi, J., Yeoman, T. K., Dyson, P. L., et al. (2007). A decade of the Super Dual Auroral Radar Network (SuperDARN): Scientific achievements, new techniques and future directions. *Surveys in Geophysics*, 28(1):33–109.

Cox, D. R. and Hinkley, D. V. (1979). *Theoretical Statistics*. CRC Press.

Davis, T. N. and Sugiura, M. (1966). Auroral electrojet activity index AE and its universal time variations. *Journal of Geophysical Research*, 71(3):785–801.

Fesen, C., Noble, R., Richmond, A., Crowley, G., and Fejer, B. G. (2000). Simulation of the prereversalenhancement in the low latitude vertical drifts. *Geophysical Research Letters*, 27(13):1851–1854.

Forbes, J. (2009). Verical coupling by the semidiurnal tide in Earth's atmosphere. *Climate and Weather of the Sun-Earth System*, pages 337–348.

Forbes, J. M. (1995). Tidal and planetary waves. *The upper mesosphere and lower thermosphere: a review of experiment and theory*, pages 67–87.

Fritts, D. C. (1984). Gravity wave saturation in the middle atmosphere: A review of theory and observations. *Reviews of Geophysics*, 22(3):275–308.

Greenwald, R., Baker, K., Dudeney, J., Pinnock, M., Jones, T., Thomas, E., Villain, J.-P., Cerisier, J.-C., Senior, C., Hanuise, C., et al. (1995). Darn/Superdarn. *Space Science Reviews*, 71(1-4):761–796.

Greenwald, R., Baker, K., Hutchins, R., and Hanuise, C. (1985). An HF phased-array radar for studying small-scale structure in the high-latitude ionosphere. *Radio Science*, 20(1):63–79.

Hall, G., MacDougall, J., Moorcroft, D., St-Maurice, J.-P., Manson, A., and Meek, C. (1997). Super dual auroral radar network observations of meteor echoes. *Journal of Geophysical Research: Space Physics (1978–2012)*, 102(A7):14603–14614.

Hibbins, R., Espy, P., and Jarvis, M. (2006). Mean winds and tides in the mesosphere and lower thermosphere above Halley, Antarctica. *Journal of atmospheric and solar-terrestrial physics*, 68(3):436–444.

Hibbins, R. and Jarvis, M. (2008). A long-term comparison of wind and tide measurements in the upper mesosphere recorded with an imaging Doppler interferometer and SuperDARN radar at Halley, Antarctica. *Atmospheric Chemistry and Physics*, 8(5):1367–1376.

Hibbins, R., Marsh, O., McDonald, A., and Jarvis, M. (2010). Interannual variability of the S= 1 and S= 2 components of the semidiurnal tide in the Antarctic MLT. *Journal of Atmospheric and Solar-Terrestrial Physics*, 72(9):794–800.

Hines, C. O. (1960). Internal atmospheric gravity waves at ionospheric heights. *Canadian Journal of Physics*, 38(11):1441–1481.

Hocking, W., Fuller, B., and Vandepeer, B. (2001). Real-time determination of meteor-related parameters utilizing modern digital technology. *Journal of Atmospheric and Solar-Terrestrial Physics*, 63(2):155–169.

Iimura, H., Fritts, D., Lieberman, R., Wu, Q., and Skinner, W. (2014). Interannual variability of the nonmigrating semidiurnal tide at high latitudes and stationary

planetary wave in the opposite hemispheres. *Journal of Atmospheric and Solar-Terrestrial Physics*, 110–111:37 – 49.

Jacobi, C., Portnyagin, Y. I., Solovjova, T., Hoffmann, P., Singer, W., Fahrutdinova, A., Ishmuratov, R., Beard, A., Mitchell, N., Muller, H., et al. (1999). Climatology of the semidiurnal tide at 52–56 N from ground-based radar wind measurements 1985–1995. *Journal of Atmospheric and Solar-Terrestrial Physics*, 61(13):975–991.

Kleinknecht, N. H., Espy, P. J., and Hibbins, R. E. (2014). The climatology of zonal wave numbers 1 and 2 planetary wave structure in the MLT using a chain of Northern Hemisphere SuperDARN radars. *Journal of Geophysical Research: Atmospheres*, 119(3):1292–1307.

Kutner, M. L. (2003). *Astronomy: A physical perspective*. Cambridge University Press.

Lei, J., Thayer, J. P., Forbes, J. M., Sutton, E. K., and Nerem, R. S. (2008). Rotating solar coronal holes and periodic modulation of the upper atmosphere. *Geophysical Research Letters*, 35(10).

Limpasuvan, V., Thompson, D. W., and Hartmann, D. L. (2004). The life cycle of the Northern Hemisphere sudden stratospheric warmings. *Journal of Climate*, 17(13):2584–2596.

Lindzen, R. S. (1981). Turbulence and stress owing to gravity wave and tidal breakdown. *Journal of Geophysical Research: Oceans*, 86(C10):9707–9714.

Lysenko, I., Portnyagin, Y. I., Fakhrutdinova, A., Ishmuratov, R., Manson, A., and Meek, C. (1994). Wind regime at 80–110 km at mid-latitudes of the northern hemisphere. *Journal of atmospheric and terrestrial physics*, 56(1):31–42.

Manney, G. L., Krüger, K., Pawson, S., Minschwaner, K., Schwartz, M. J., Daffer, W. H., Livesey, N. J., Mlynczak, M. G., Remsberg, E. E., Russell, J. M., et al. (2008). The evolution of the stratopause during the 2006 major warming: Satellite data and assimilated meteorological analyses. *Journal of Geophysical Research: Atmospheres*, 113(D11).

Manney, G. L., Schwartz, M. J., Krüger, K., Santee, M. L., Pawson, S., Lee, J. N., Daffer, W. H., Fuller, R. A., and Livesey, N. J. (2009). Aura Microwave Limb Sounder observations of dynamics and transport during the record-breaking 2009 Arctic stratospheric major warming. *Geophysical Research Letters*, 36(12).

Manson, A., Meek, C., Teitelbaum, H., Vial, F., Schminder, R., Kürschner, D., Smith, M. J., Fraser, G., and Clark, R. (1989). Climatologies of semi-diurnal and diurnal

tides in the middle atmosphere (70–110 km) at middle latitudes (40–55). *Journal of atmospheric and terrestrial Physics*, 51(7):579–593.

Matsuno, T. (1971). A dynamical model of the stratospheric sudden warming. *Journal of the Atmospheric Sciences*, 28(8):1479–1494.

Mitchell, N., Pancheva, D., Middleton, H., and Hagan, M. (2002). Mean winds and tides in the Arctic mesosphere and lower thermosphere. *Journal of Geophysical Research: Space Physics*, 107(A1).

Murphy, D., Forbes, J., Walterscheid, R., Hagan, M., Avery, S., Aso, T., Fraser, G., Fritts, D., Jarvis, M., McDonald, A., et al. (2006). A climatology of tides in the Antarctic mesosphere and lower thermosphere. *Journal of Geophysical Research: Atmospheres (1984–2012)*, 111(D23).

Murphy, D., Tsutsumi, M., Riggin, D., Jones, G., Vincent, R., Hagan, M., and Avery, S. (2003). Observations of a nonmigrating component of the semidiurnal tide over Antarctica. *Journal of Geophysical Research: Atmospheres*, 108(D8).

Newton, H. and Nunn, M. (1951). The sun's rotation derived from sunspots 1934–1944 and additional results. *Monthly Notices of the Royal Astronomical Society*, 111(4):413–421.

Oberheide, J., Hagan, M., A.D., R., and J.M, F. (2015). *Dynamical Meteorology: Atmospheric Tides*.

Paldor, N. (2008). Non-divergent 2D vorticity dynamics and the shallow water equations on the rotating earth. In *IUTAM Symposium on Hamiltonian Dynamics, Vortex Structures, Turbulence*, pages 177–187. Springer.

Pedatella, N. and Liu, H.-L. (2013). The influence of atmospheric tide and planetary wave variability during sudden stratosphere warmings on the low latitude ionosphere. *Journal of Geophysical Research: Space Physics*, 118(8):5333–5347.

Pedatella, N., Liu, H.-L., Richmond, A., Maute, A., and Fang, T.-W. (2012). Simulations of solar and lunar tidal variability in the mesosphere and lower thermosphere during sudden stratosphere warmings and their influence on the low-latitude ionosphere. *Journal of Geophysical Research: Space Physics*, 117(A8).

Riggin, D., Fritts, D., Jarvis, M., and Jones, G. (1999). Spatial structure of the 12-hour wave in the Antarctic as observed by radar. *Earth, planets and space*, 51(7-8):621–628.

Rostoker, G. (1972). Geomagnetic indices. *Reviews of Geophysics*, 10(4):935–950.

Russell, C., , and McPherron, R. (1973). Semiannual variation of geomagnetic activity. *Journal of geophysical research*, 78(1):92–108.

Schminder, R., Kuèrschner, D., Manson, A., and Meek, C. (1989). Semidiurnal tidal winds at Collm (52N, 15E) and Saskatoon (52N, 107W) over the decade 1978–1988. *Journal of atmospheric and terrestrial physics*, 51(7):623–626.

Stray, N., Orsolini, Y., Espy, P., Limpasuvan, V., and Hibbins, R. (2015). Observations of PW activity in the MLT during SSW events using a chain of SuperDARN radars and SD-WACCM. *Atmospheric Chemistry and Physics Discussions*, 15(1):393–413.

Stray, N. H. (2015). Planetary waves in the MLT: Vertical coupling and effects.

Taylor, G. (1929). Waves and tides in the atmosphere. *Proceedings of the Royal Society of London. Series A, Containing Papers of a Mathematical and Physical Character*, 126(800):169–183.

Thayer, J. P., Lei, J., Forbes, J. M., Sutton, E. K., and Nerem, R. S. (2008). Thermospheric density oscillations due to periodic solar wind high-speed streams. *Journal of Geophysical Research: Space Physics*, 113(A6).

Tsurutani, B. T., Gonzalez, W. D., Gonzalez, A. L., Guarnieri, F. L., Gopalswamy, N., Grande, M., Kamide, Y., Kasahara, Y., Lu, G., Mann, I., et al. (2006). Corotating solar wind streams and recurrent geomagnetic activity: A review. *Journal of Geophysical Research: Space Physics*, 111(A7).

Tweedy, O. V., Limpasuvan, V., Orsolini, Y. J., Smith, A. K., Garcia, R. R., Kinnison, D., Randall, C. E., Kvissel, O.-K., Stordal, F., Harvey, V. L., et al. (2013). Nighttime secondary ozone layer during major stratospheric sudden warmings in specified-dynamics WACCM. *Journal of Geophysical Research: Atmospheres*, 118(15):8346–8358.

Wu, Q., Ortland, D., Solomon, S., Skinner, W., and Niciejewski, R. (2011). Global distribution, seasonal, and inter-annual variations of mesospheric semidiurnal tide observed by TIMED TIDI. *Journal of Atmospheric and Solar-Terrestrial Physics*, 73(17):2482–2502.

Appendix A

Daily amplitude plots of S1 and S2

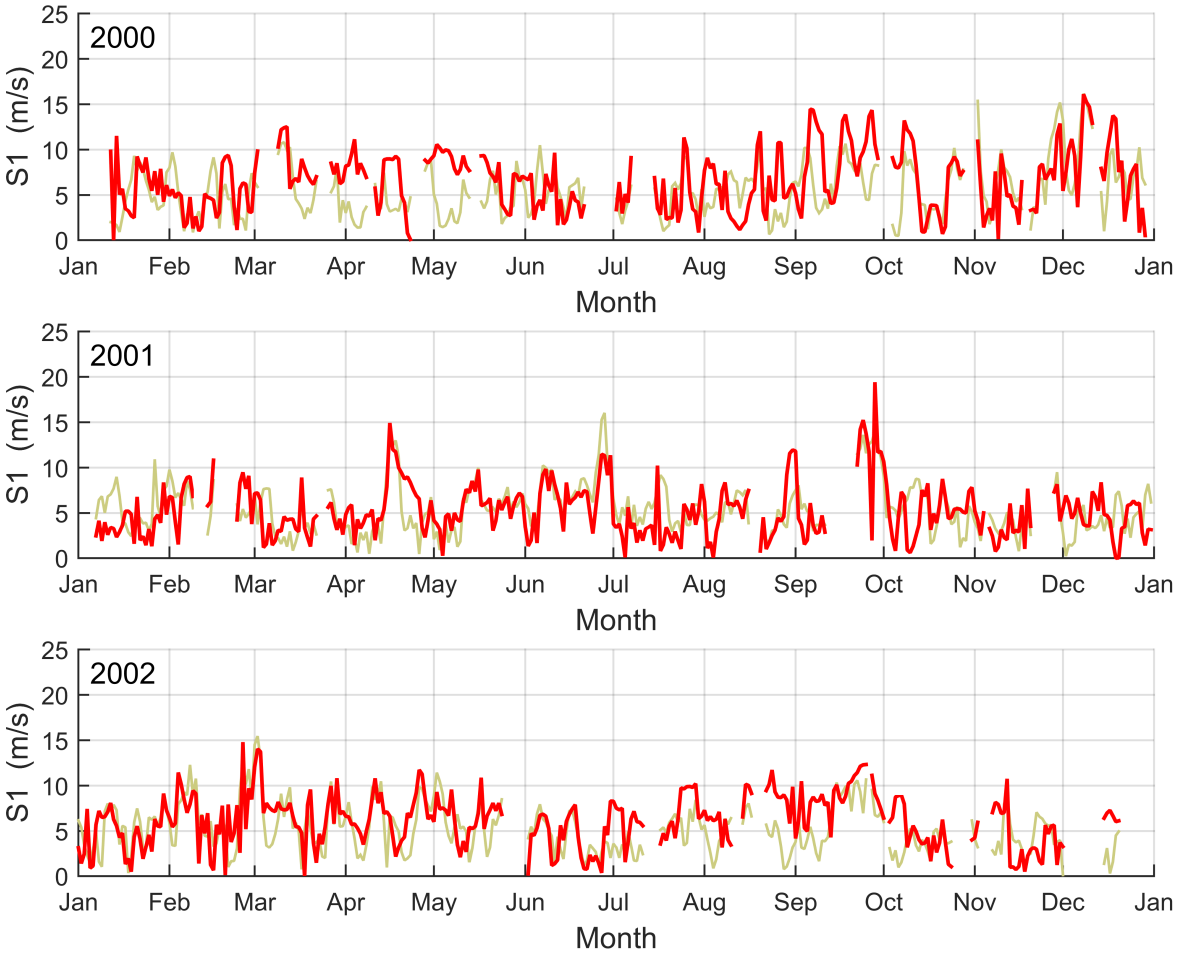

Figure A.1: Plot of the semidiurnal S1 amplitude from 2000-2008. The red line shows the amplitude from the fit and the gold line is from the two station method.

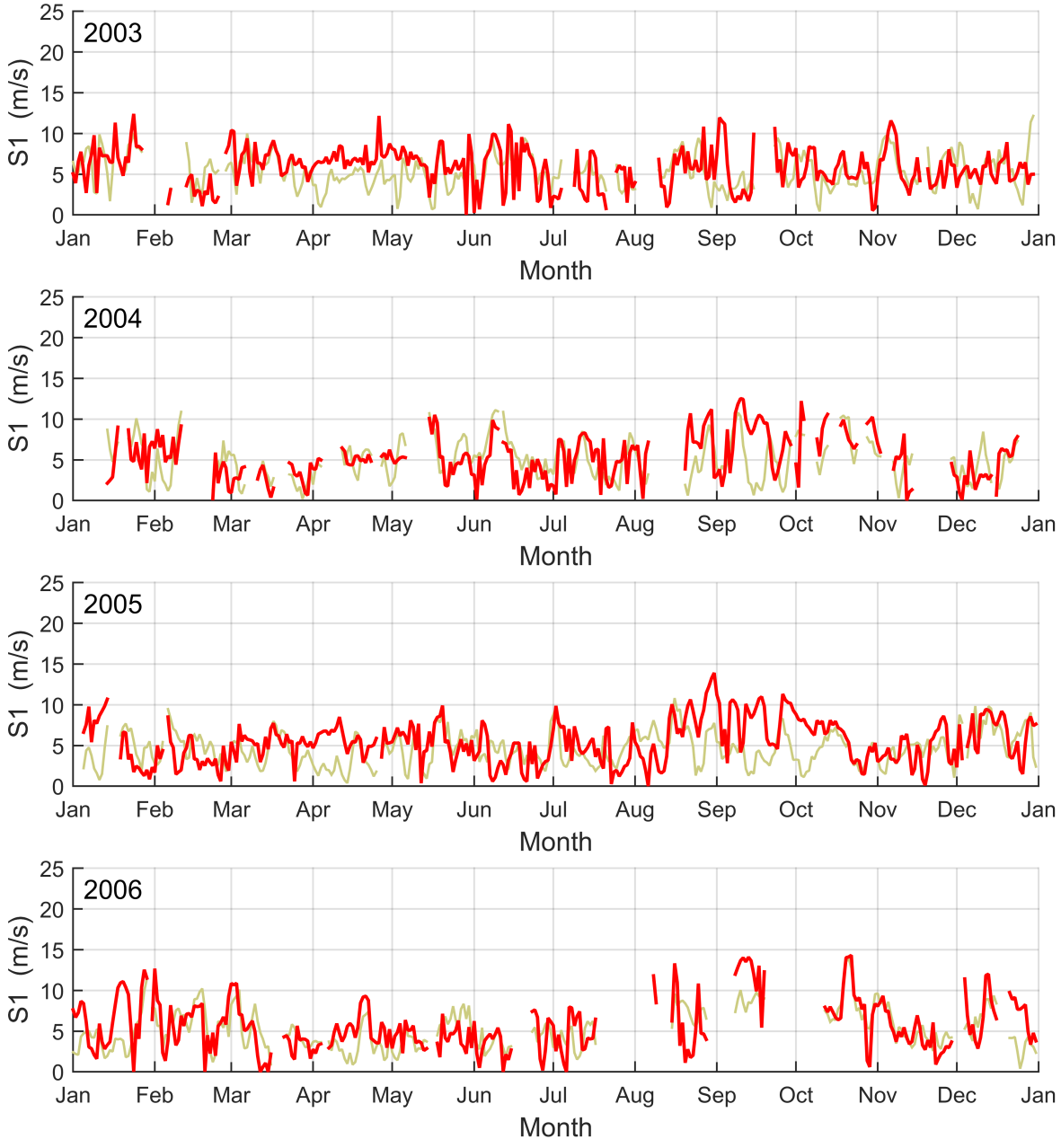

Figure A.1 (cont.)

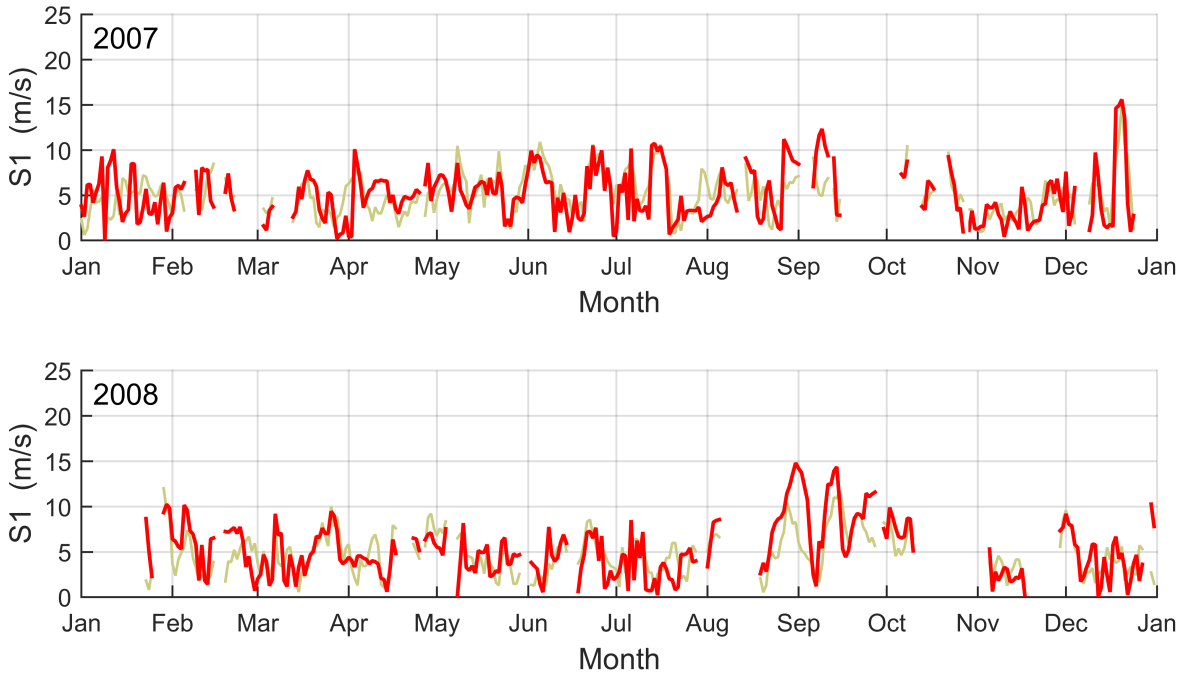

Figure A.1 (cont.)

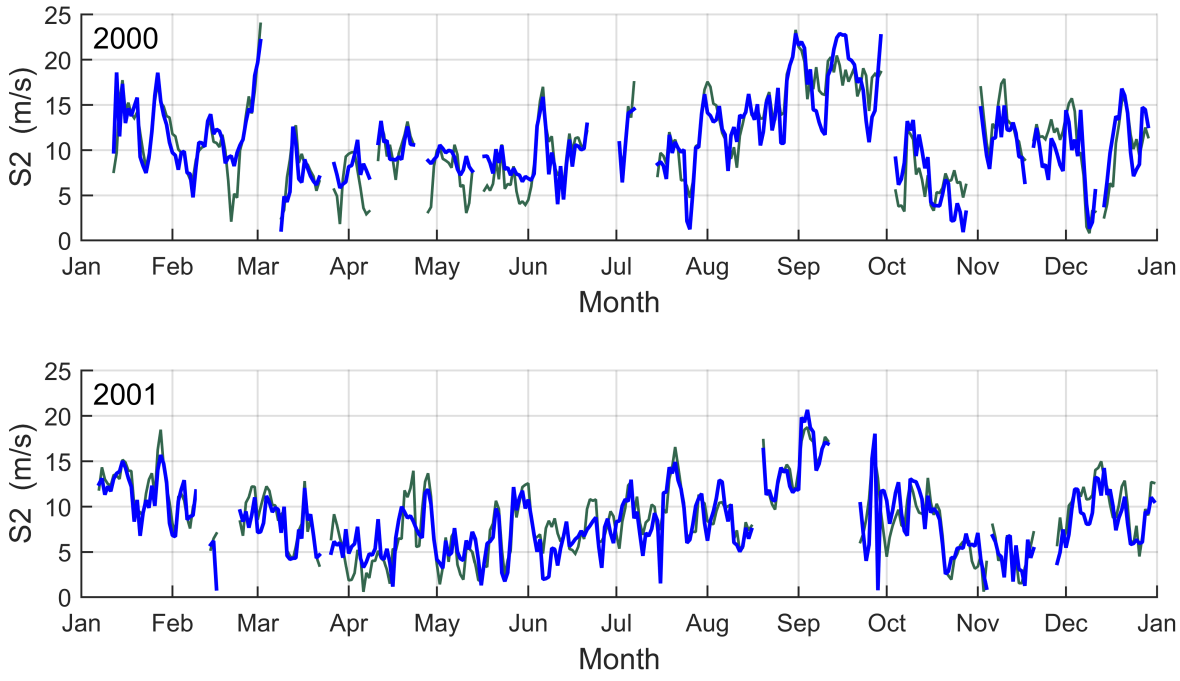

Figure A.2: As figure A.1 only for S2. Fit (blue), two station (green)

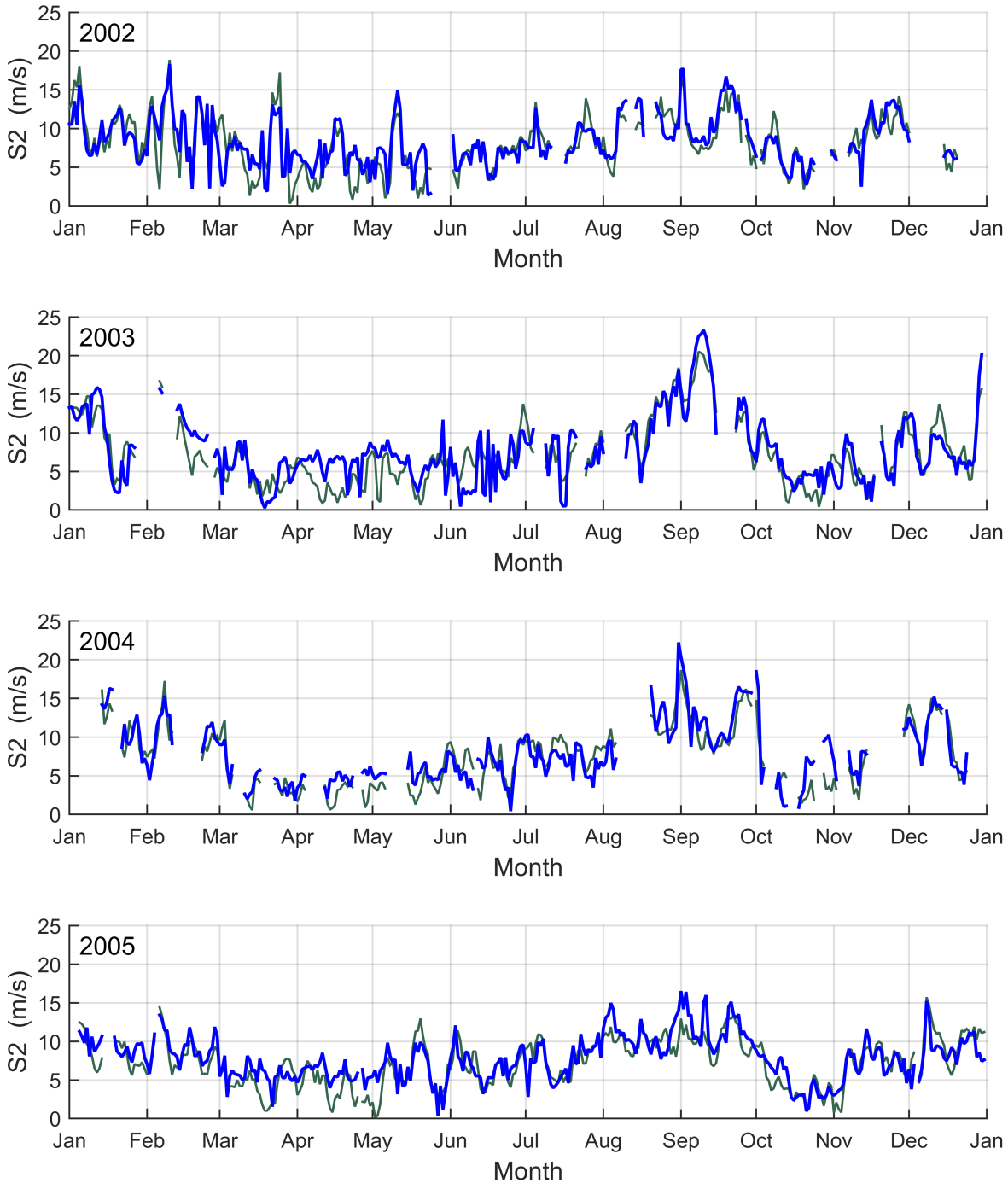

Figure A.2 (cont.)

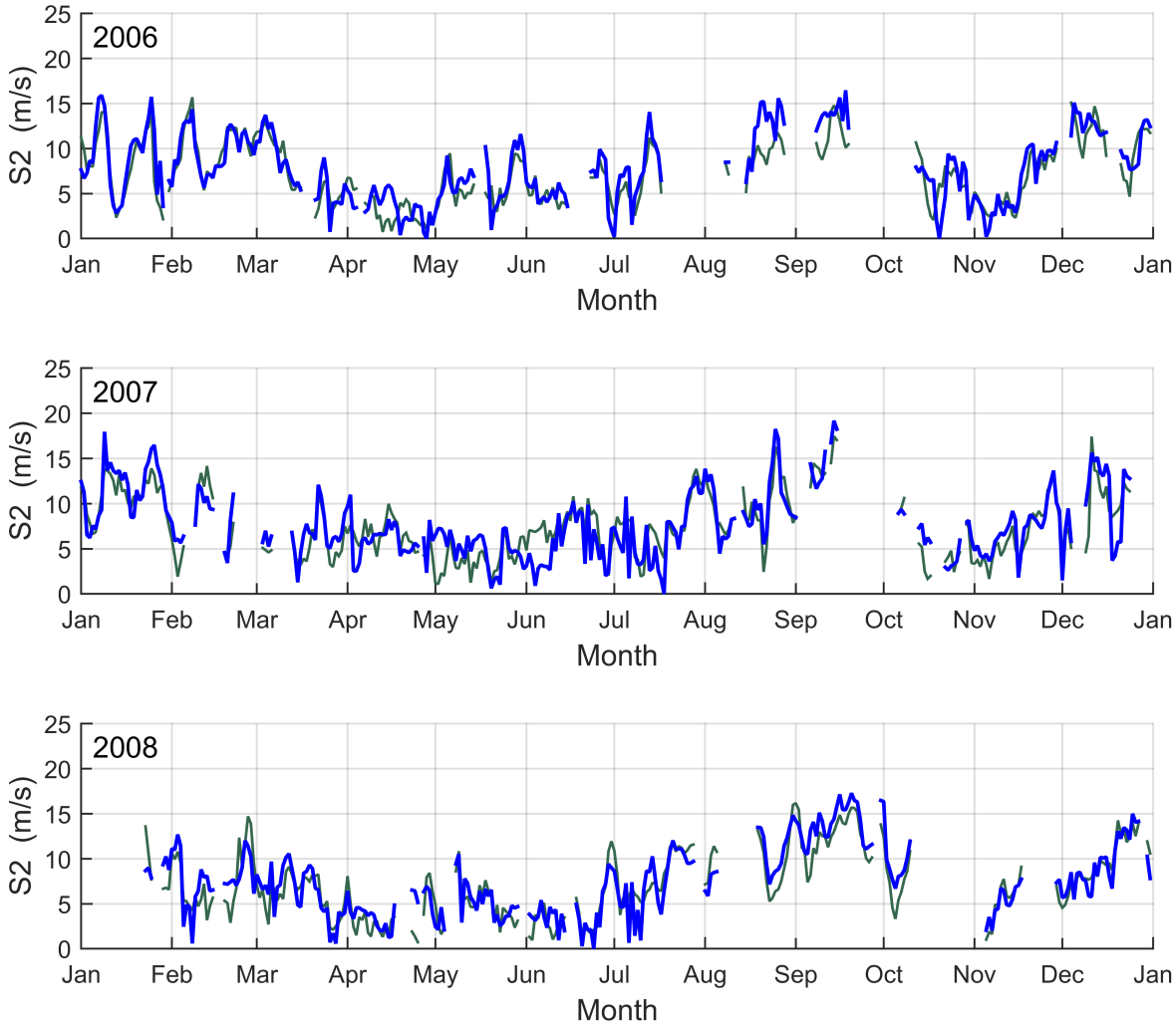

Figure A.2 (cont.)

Appendix B

Daily anomaly amplitude plots of S1 and S2

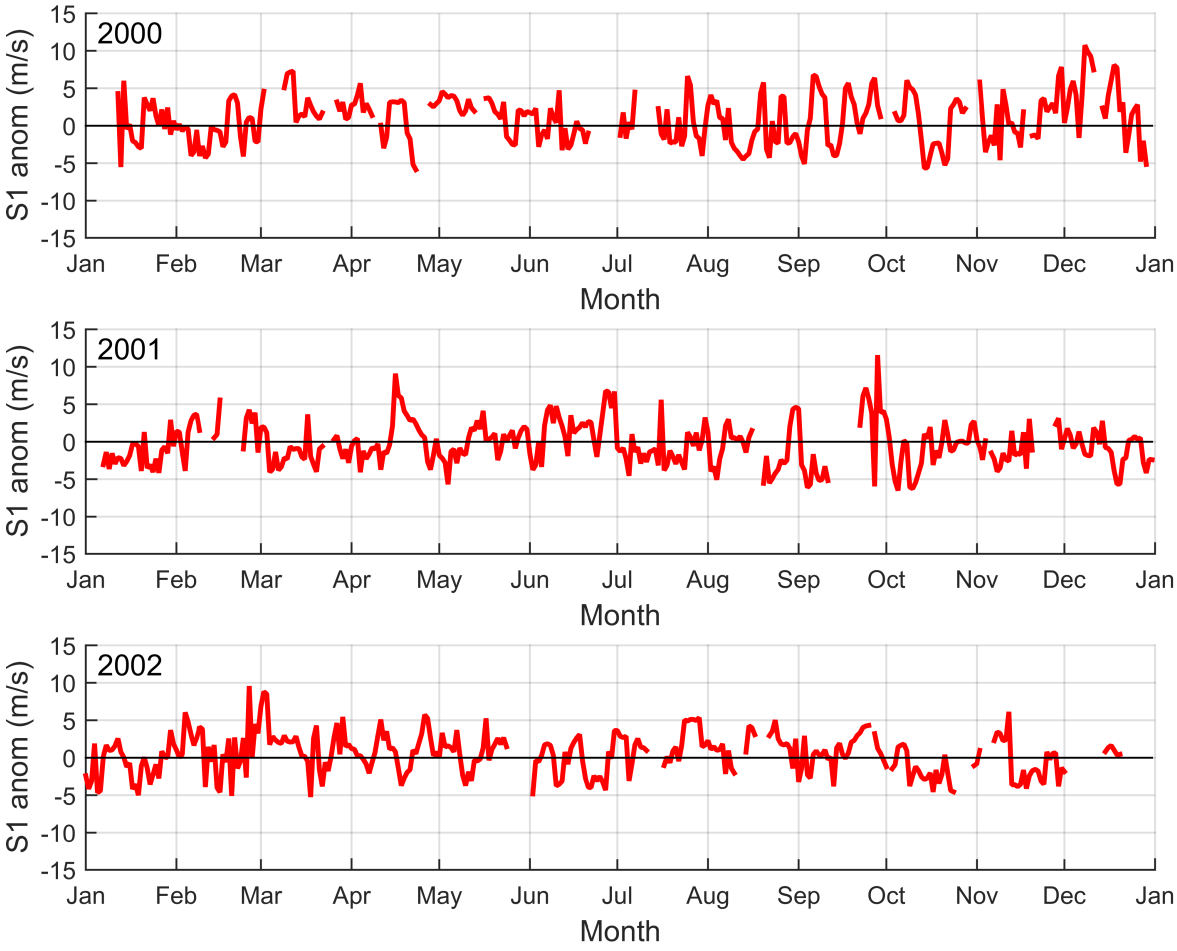

Figure B.1: Anomaly amplitude of S1 from 2000-2008

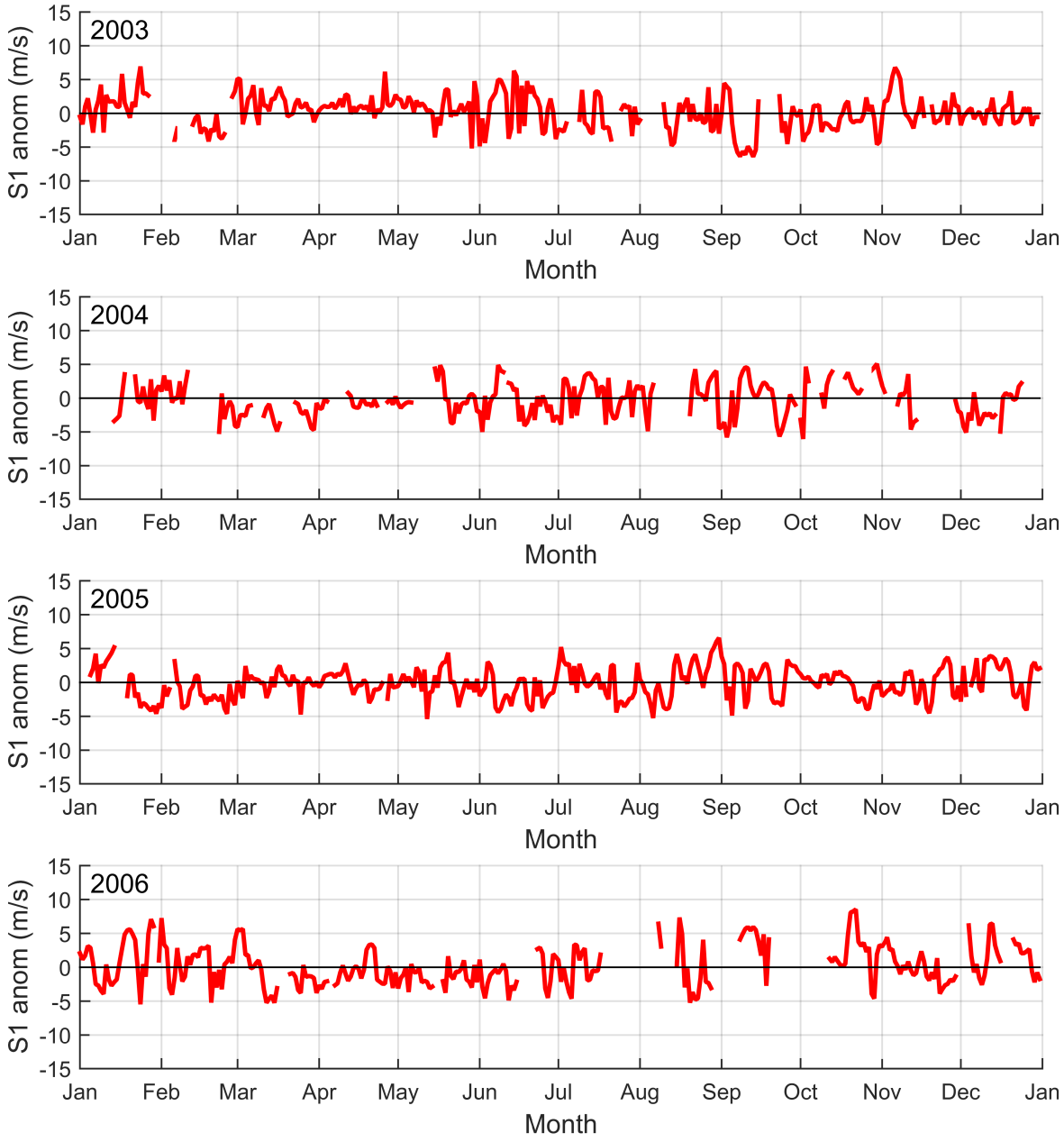

Figure B.1 (cont.)

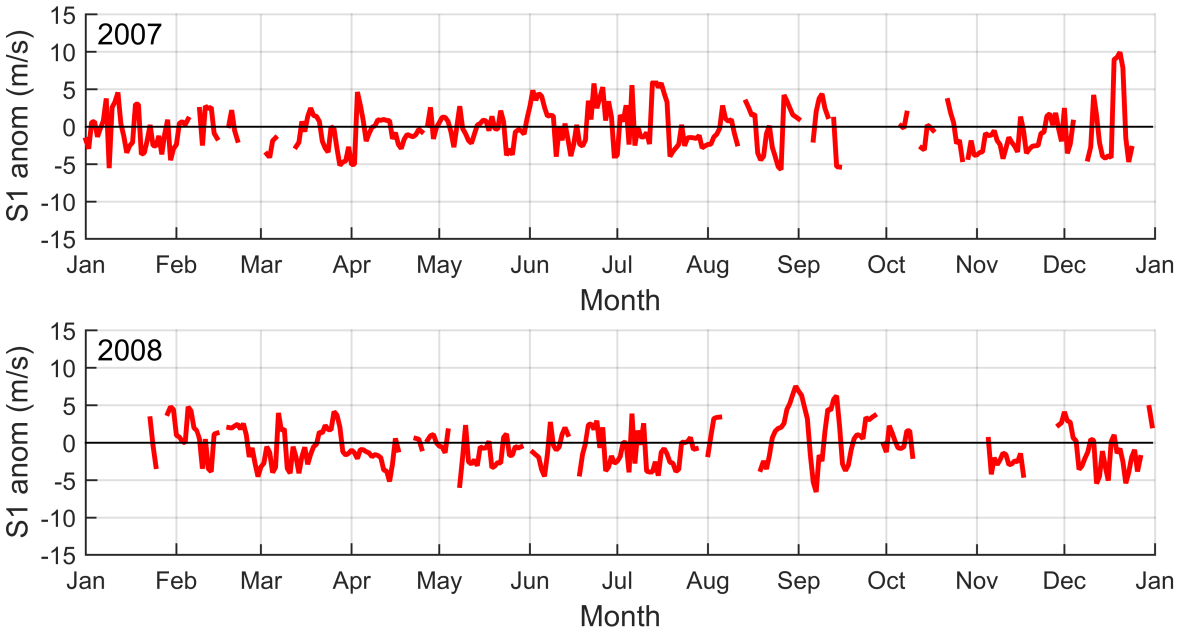

Figure B.1 (cont.)

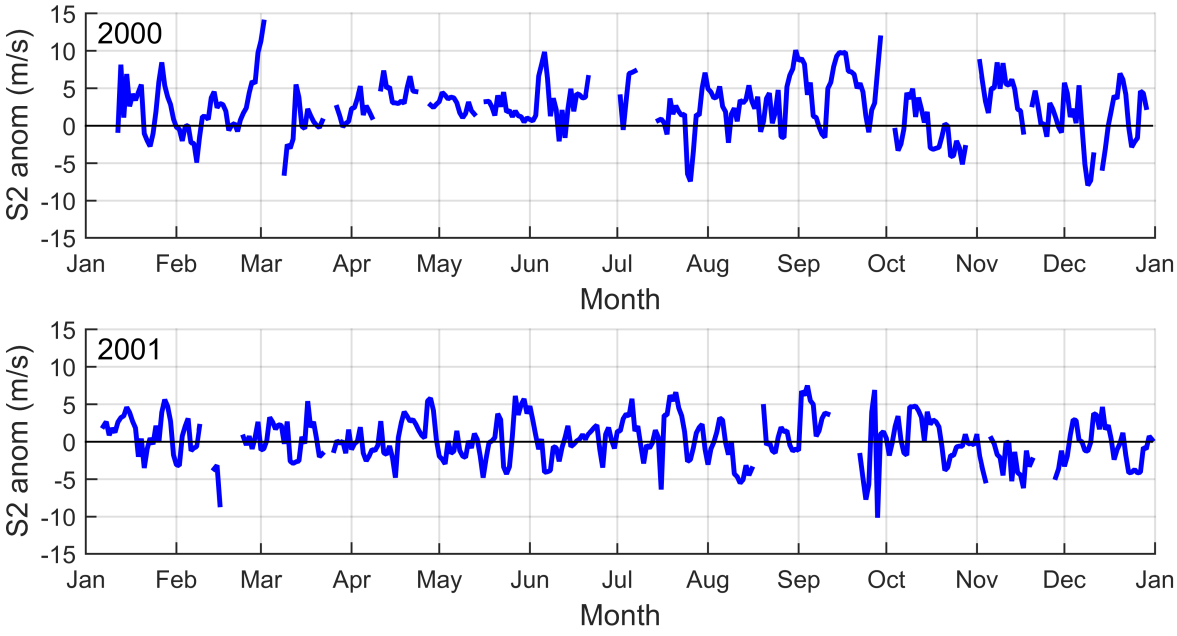

Figure B.2: Same as for figure B.1 only for S2.

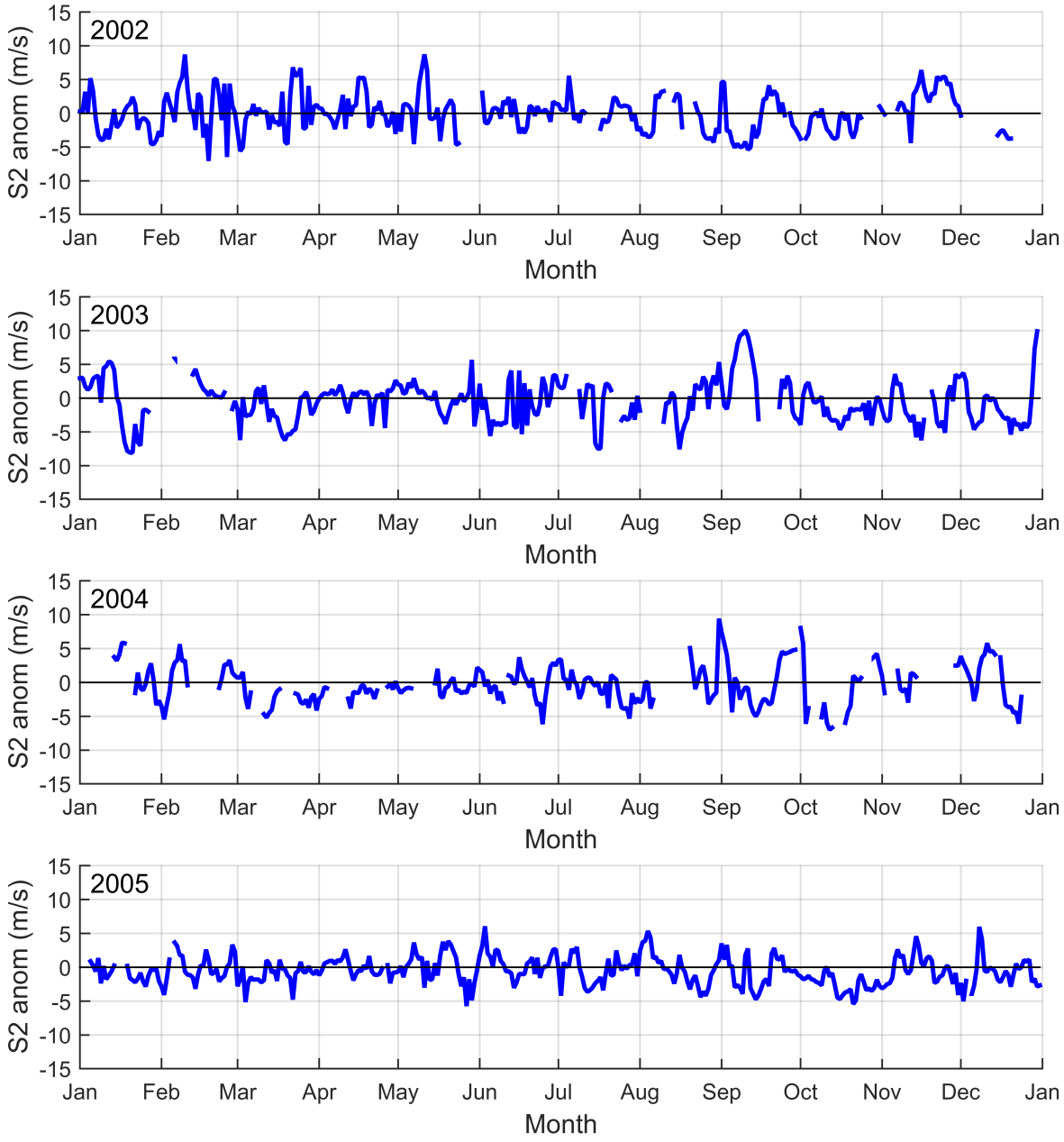

Figure B.2 (cont.)

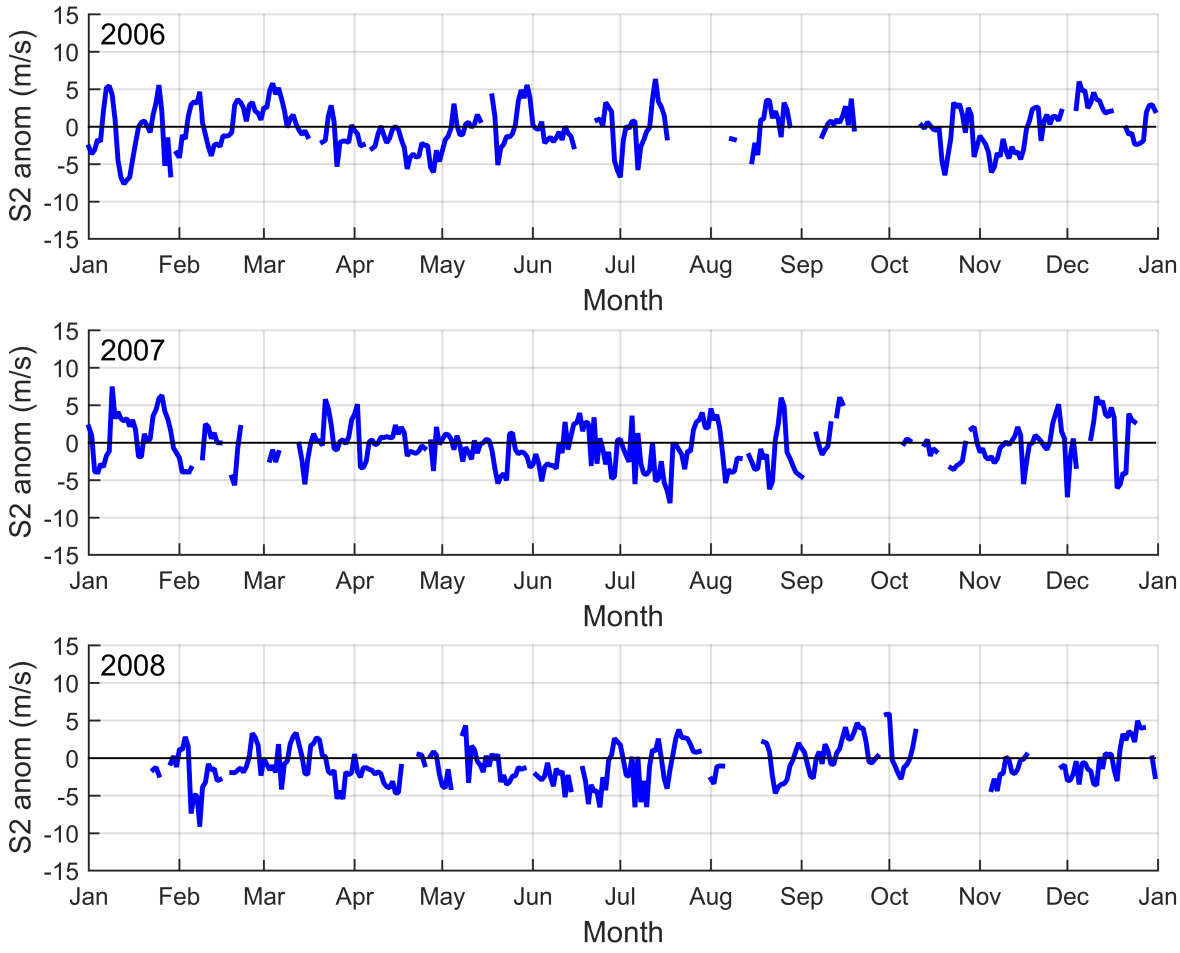

Figure B.2 (cont.)

Appendix C

Daily phase plots of S1 and S2

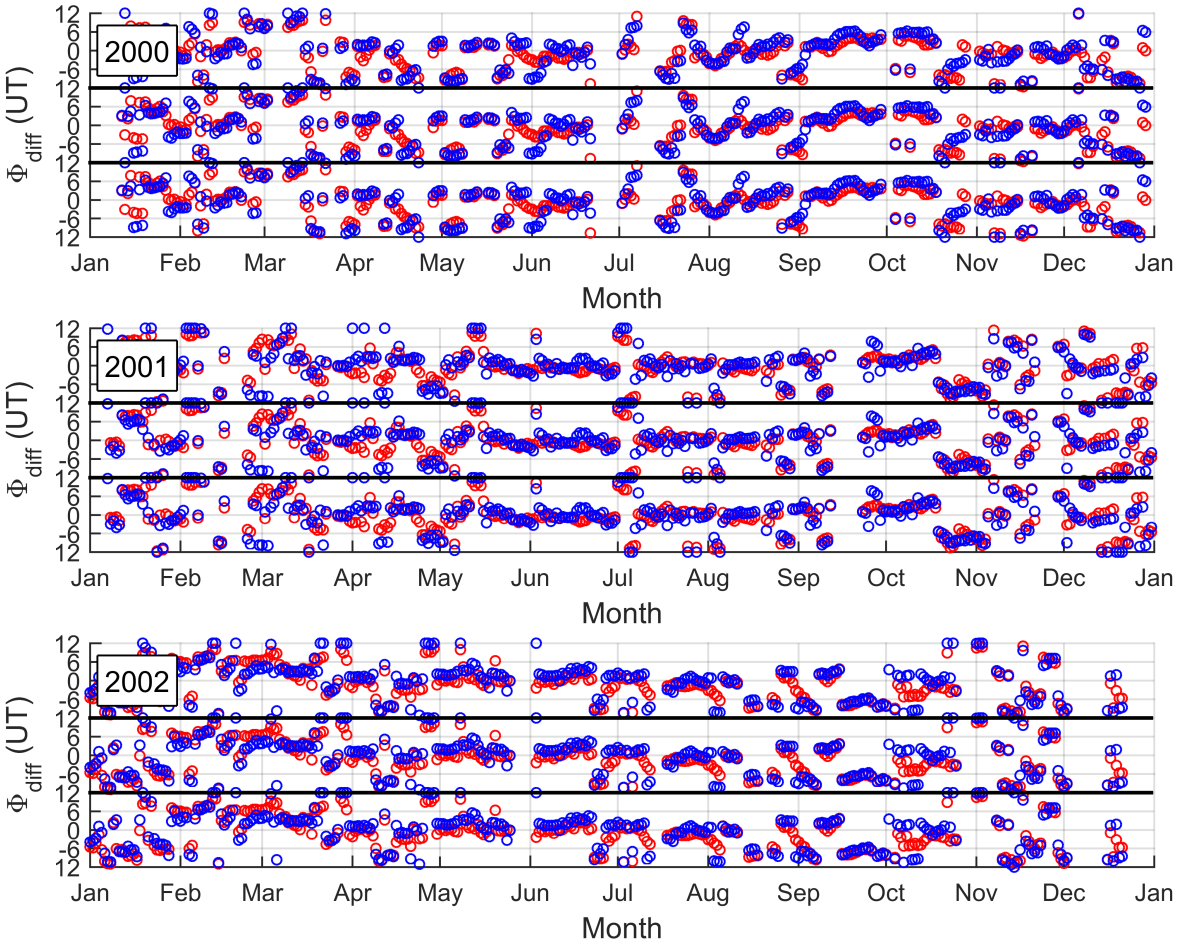

Figure C.1: Plot of the phase difference from 2000-2008 in UT. Blue circles are from the fitting routine, and red are from the two station method. The phases are repeated three cycles to show coherence.

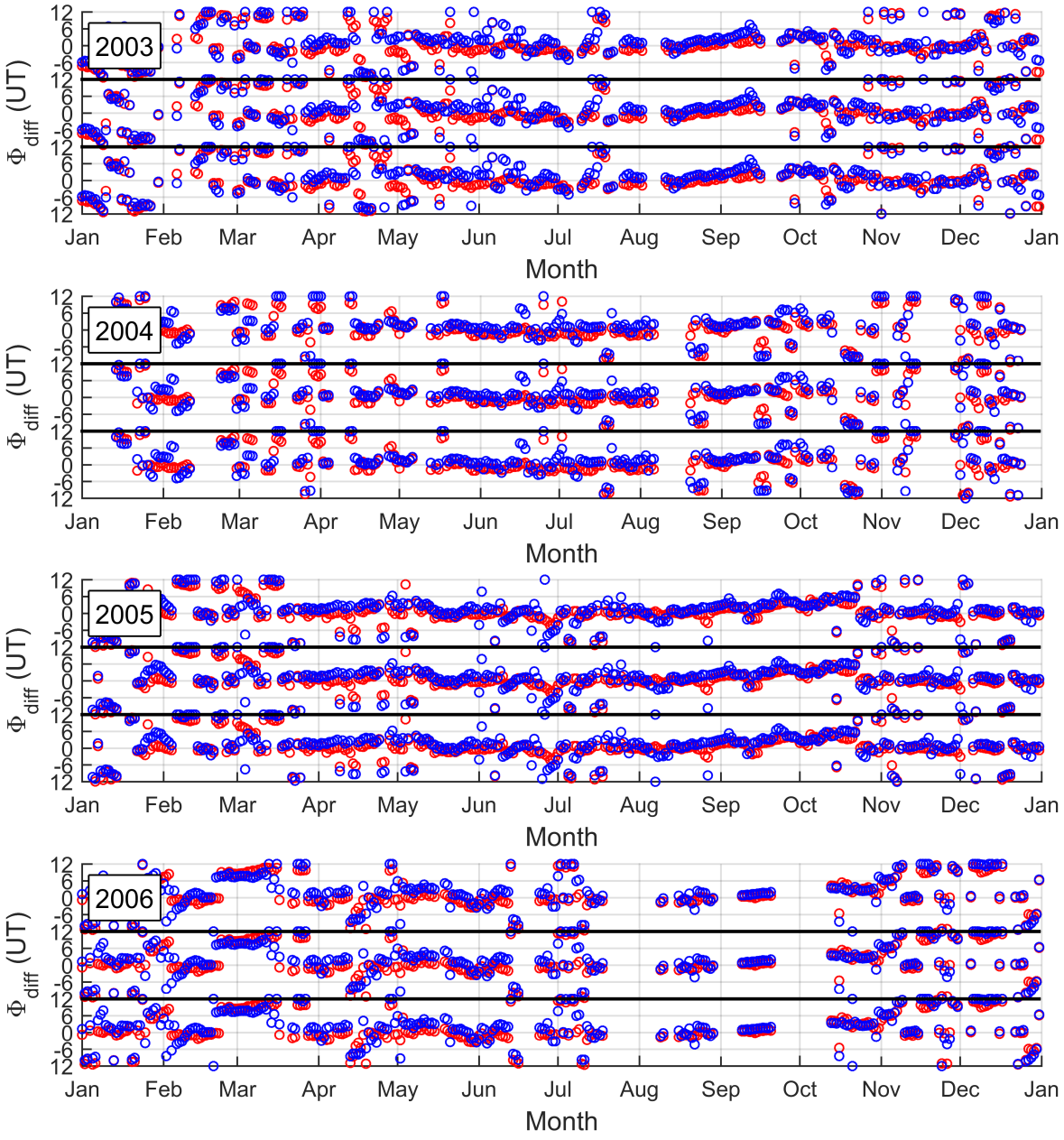

Figure C.1 (cont.)

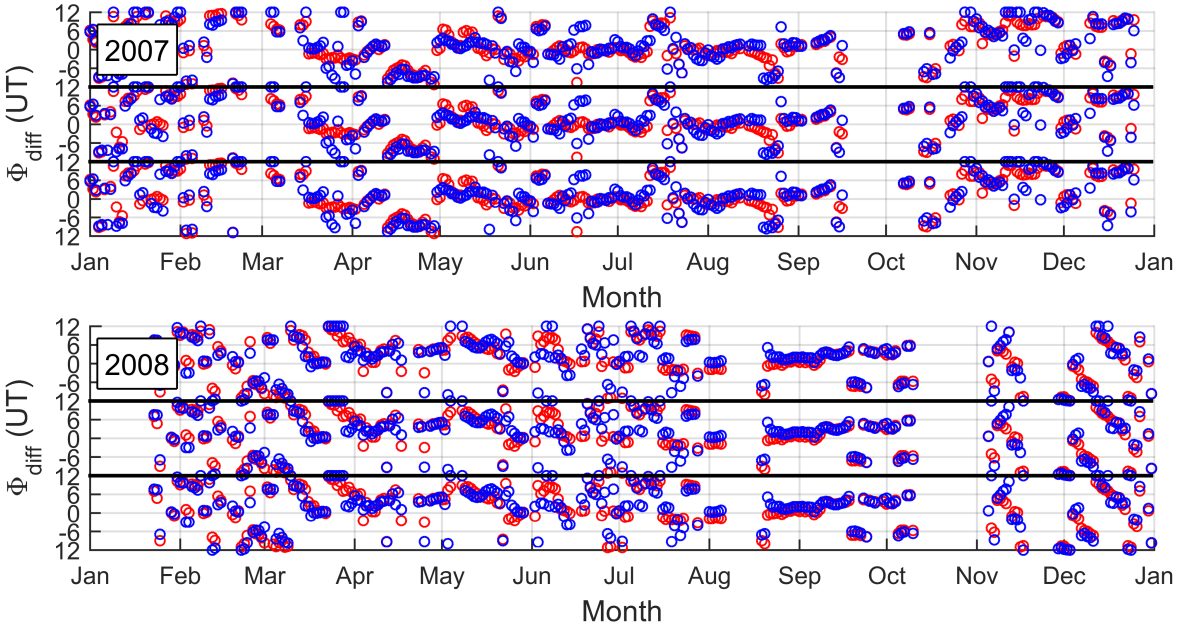

Figure C.1 (cont.)

Appendix D
AE correlation plots

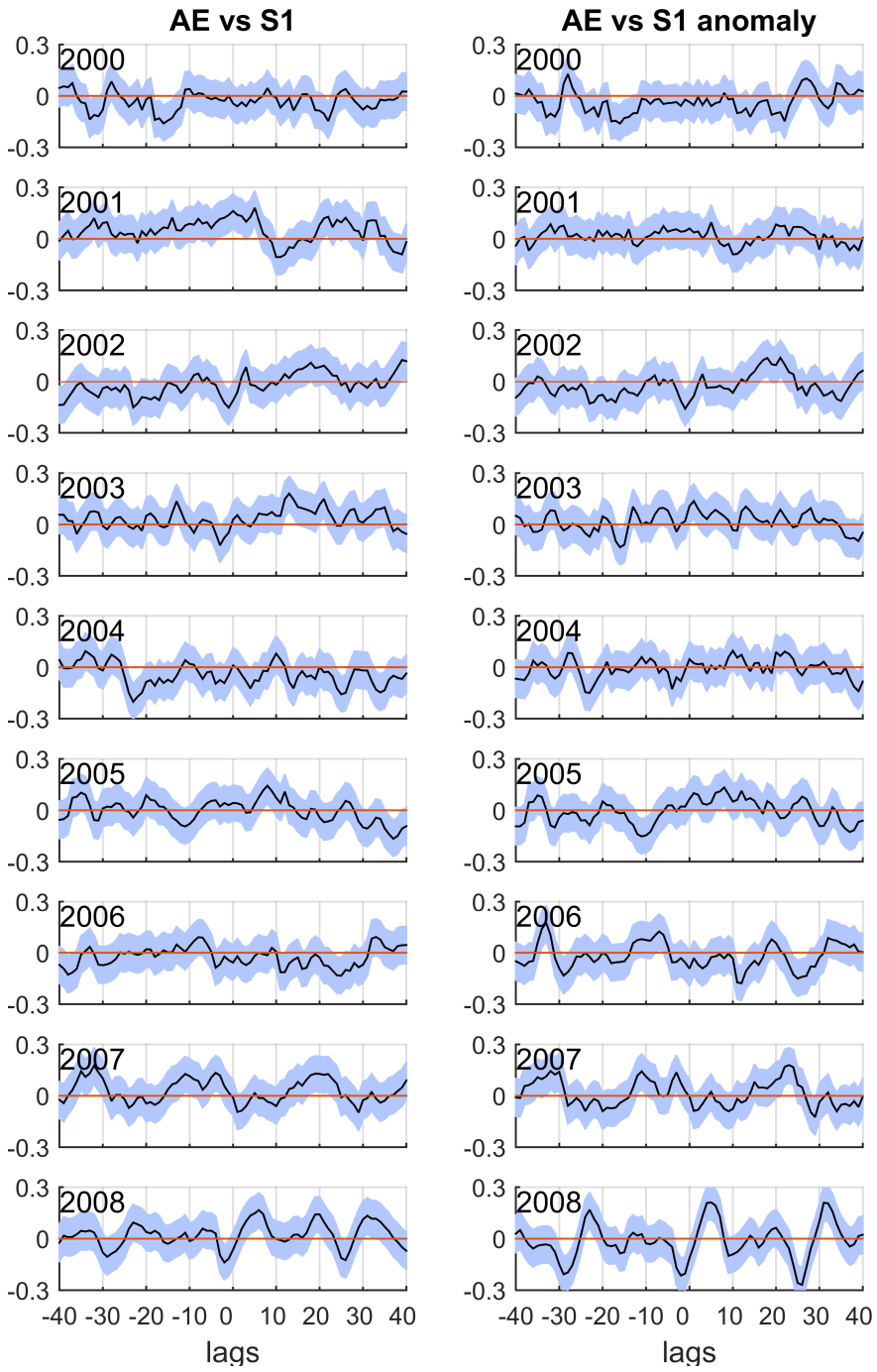

Figure D.1: *AE* index correlation with the S1 amplitude indicated in title for years indicated in top left.

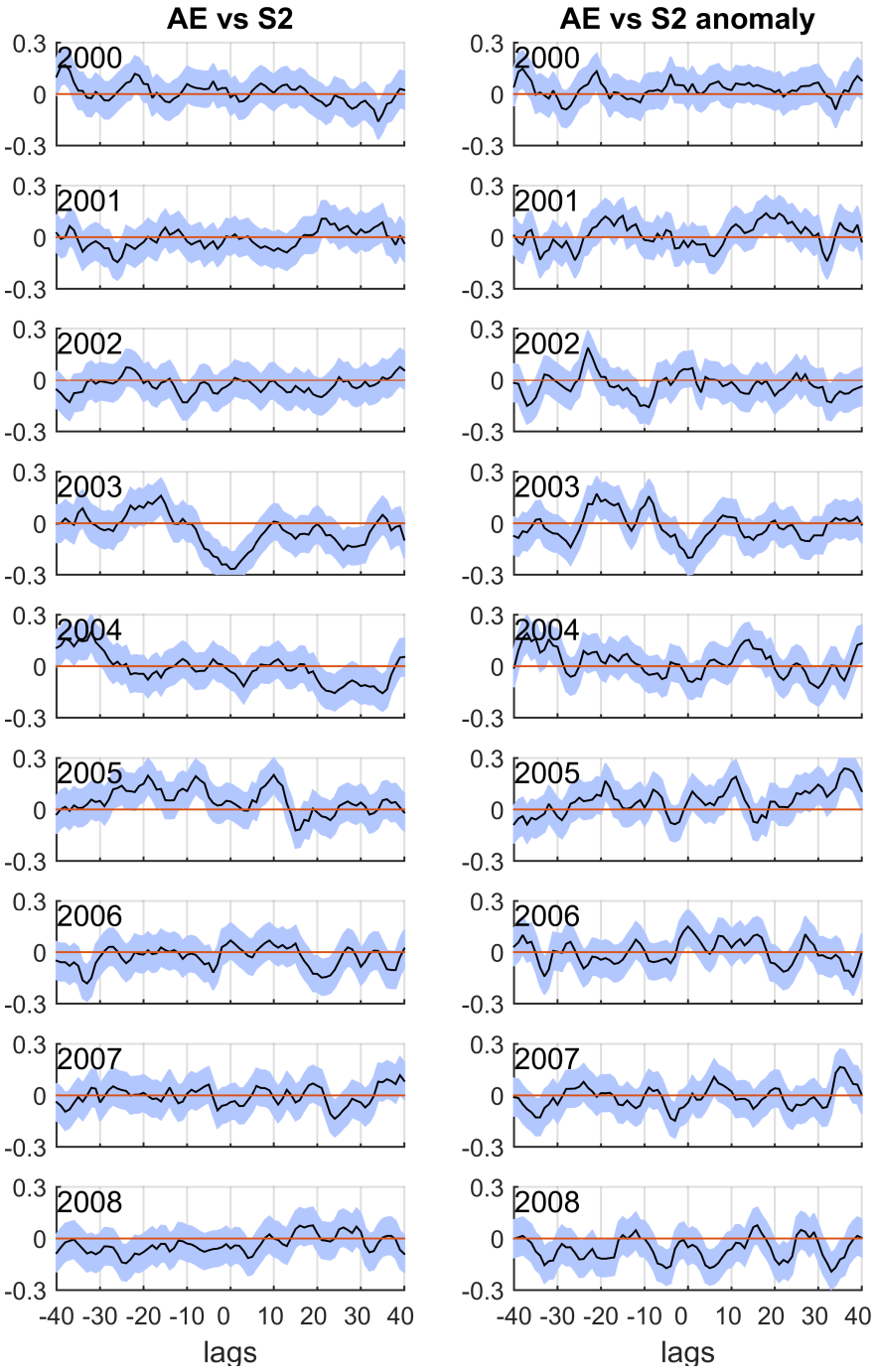

Figure D.2: Same as for figure D.1 only for S2.